#### **Marshall University**

## Marshall Digital Scholar

Theses, Dissertations and Capstones

2024

## Numerical design, fabrication, and characterization of porous tissue scaffolds for bone regeneration

Brandon Coburn Coburn30@marshall.edu

Follow this and additional works at: https://mds.marshall.edu/etd



Part of the Biomechanical Engineering Commons, and the Molecular, Cellular, and Tissue Engineering Commons

#### **Recommended Citation**

Coburn, Brandon, "Numerical design, fabrication, and characterization of porous tissue scaffolds for bone regeneration" (2024). Theses, Dissertations and Capstones. 1910. https://mds.marshall.edu/etd/1910

This Thesis is brought to you for free and open access by Marshall Digital Scholar. It has been accepted for inclusion in Theses, Dissertations and Capstones by an authorized administrator of Marshall Digital Scholar. For more information, please contact beachgr@marshall.edu.

## NUMERICAL DESIGN, FABRICATION, AND CHARACTERIZATION OF POROUS TISSUE SCAFFOLDS FOR BONE REGENERATION

A thesis submitted to
Marshall University
in partial fulfillment of
the requirements for the degree of
Master of Science
in
Mechanical Engineering
by
Brandon Coburn
Approved by
Dr. Roozbeh "Ross" Salary, Committee Chairperson
Dr. James B. Day
Dr. Nalini Santanam

Marshall University August 2024

#### **Approval of Thesis**

We, the faculty supervising the work of Brandon Coburn, affirm that the thesis, *Numerical Design, Fabrication, and Characterization of Porous Tissue Scaffolds for Bone Regeneration*, meets the high academic standards for original scholarship and creative work established by the Weisberg Department of Mechanical and Industrial Engineering and the College of Engineering and Computer Sciences. The work also conforms to the requirements and formatting guidelines of Marshall University. With our signatures, we approve the manuscript for publication.

Ross Salary		06/25/2024
Dr. Roozbeh "Ross" Salary Department of Mechanical & Industrial Engineering, College of Engineering & Computer Sciences, Marshall University	Committee Chairperson	Date
Jelley		30 June 2024
Dr. James B. Day Department of Orthopaedics, School of Medicine, Marshall University	Committee Member	Date
of Jankowin		6/28/2024
Dr. Nalini Santanam Department of Biomedical Sciences, School of Medicine, Marshall University	Committee Member	Date

© 2024 Brandon Coburn ALL RIGHTS RESERVED

#### Acknowledgments

I want to acknowledge the committee chairperson, Dr. Roozbeh "Ross" Salary, and committee members Dr. James B. Day and Dr. Nalini Santanam. Their critiques and challenges have significantly improved the quality of my thesis. Furthermore, a heartfelt thank you to Dr. Roozbeh "Ross" Salary for his guidance and diligence, shaping me into the researcher I am today. More importantly, his mentoring has made me a better person who can face challenges with confidence and clarity for my future endeavors.

I want to thank my family and friends for their unwavering support and encouragement, who have been a constant source of strength throughout this academic journey. I would not be where I am today without their love and support. A special thanks to my mother, uncle, and girlfriend for their role in my achievements cannot be overstated.

### **Table of Contents**

List of Tablesx
List of Figures xi
Abstractxiii
Chapter 1: Introduction
Significance, Goals, and Objectives
Literature Review of the Mechanical Influence Characteristic of Bioactive Material of
Composite Bone Tissue Scaffolds
Literature Review of Material Transport of Triply Periodic Minimal Surface (TPMS) Bone
Scaffolds6
Literature Review of Mechanical Properties of Bone-Like, Porous Tissue Scaffolds with
Medical-Grade Material for Bone Regeneration
Literature Review of Machine Learning Network In-Process to Assess Complex Porosity of
Bone Tissue Scaffolds
Chapter 2: Investigation of the Influence of Nylon-6 vs. Nylon-66 on the Mechanical
Performance of Composite Bone Tissue Scaffolds
Goal and Objectives
Material
3D-Microfabrication Process
Experimental Designs
Results and Discussion

Summary
Chapter 3: Characterization of the Mechanical Properties of Bone-Like, Porous Tissue Scaffolds
with Complex Microstructures Composed of a Medical-Grade Material for Bone Regeneration 38
Goal and Objectives
Material and Methods
Experimental Designs
Scaffold Design
Modeling Software
Torsion Bar
Tensile Bar
Compression TPMS Scaffolds
Materials
3D-Microfabrication Process
Fused Deposition Modeling Process
Cura Settings
Results and Discussion
Torsion Analysis
Tensile Analysis
Scaffold Compression Analysis and Optimal TPMS Scaffold Design 50
Summary

Chapter 4: Investigation of Material Transport through Triply Periodic Minima	al Surface (TPMS)
Bone Scaffolds Using Computational Fluid Dynamics (CFD)	57
Goal and Objectives	57
Material and Methods	58
Scaffold Design	58
Meshing	61
Governing Equations in CFD Analysis	63
Fluid Properties and Boundary Conditions	64
Numerical Solutions	65
Verification and Validation	65
Validation	65
Verification	66
Results and Discussion	66
Internal Flow Simulation Pressure Contours Analysis	66
Internal Flow Simulation Wall Shear Stress Analysis	69
Internal Flow Simulation Velocity Streamline Analysis	71
External Flow Simulation Pressure Contour Analysis	73
External Flow Simulation Wall Shear Stress Analysis	75
External Flow Simulation Velocity Streamline Analysis	77
External Cubic Flow Simulation Pressure Contour Analysis	79

External Cubic Flow Simulation Wall Shear Stress Analysis	81
External Cubic Flow Simulation Velocity Streamline Analysis	83
Significance and Biological Implications of the Results	85
Identification of Optimal Designs	85
Summary	86
Internal Flow	87
External Flow	87
External Cubic Flow	88
Chapter 5: A Convolutional Neural Network Model for In-Process Assessment of the	e Complex
Porosity of Additively Manufactured Bone Tissue Scaffolds	90
Goal and Objectives	90
Material and Methods	90
Materials	91
Experimental Designs	91
TPMS Scaffolds	91
Modeling Software	92
Image Capturing	94
3D-Fabrication Process	95
Fused Deposition Modeling Process	95
Cura Parameters	96

CNN Process	98
Class Categorization	98
Training Code for Prediction	99
Testing Code for Validation	100
Hyper Parameters	100
Results and Discussion	101
CNN Hyperparameter Optimization	101
Accuracy of CNN	103
Loss of CNN	105
Validation Accuracy of CNN	107
Validation Loss of CNN	108
F-Score Effects on Hyper Parameters	110
Summary	112
Chapter 6: Conclusion	113
References	116
Appendix A: IRB Approval Letter	123

### **List of Tables**

Table 1	The design, material, and extrusion process parameters	28
Table 2	Parametric equations of TPMS design 1 - 10	41
Table 3	Rhion 7 parameters for all 10 TPMS scaffolds	42
Table 4	Parameters for torsion bar and tensile bar	43
Table 5	Cura Setting with The Fabrication Parameters of The TPMS Scaffold for All 10	0
	Designs, Torsion Bar, And Tensile Bar	47
Table 6	Parametric Equations of TPMS Design 1 - 10	59
Table 7	TPMS design parameters within Rhino 7	60
Table 8	Number of Elements in Each CFD Design Model	62
Table 9	CFD Meshing Parameters for Design $1-10$ For Internal and External Flow	
	Analysis	63
Table 10	Parametric equations of TPMS design 1 - 5	93
Table 11	Rhion 7 parameters for all 5 TPMS scaffolds	94
Table 12	Cura setting with the fabrication parameters of the TPMS scaffold for all 5	
	designs and fatigue bar, torsion bar, and tensile bar	97
Table 13	Hyperparameters optimization setting ranges for Batch size, Convolutional layer	ers,
	Dense layers, Layer size, and Epoch iteration	101
Table 14	Hyperparameters optimization values for Batch size, Convolutional layers, Der	nse
	layers, Layer size, and Epoch iteration	112

## **List of Figures**

Figure 1	A schematic diagram of material transport and deposition in fused deposition
	modeling (FDM) additive manufacturing process
Figure 2	Triply Periodic Minimal Surface of All Four TPMS designs (Schwarz-Primitive,
	Neovius, Schwarz-Diamond, and Schwarz-Gyroid)27
Figure 3	Monochromatic images of the 3D-fabricated TPMS bone scaffolds30
Figure 4	A comparison of the compression modulus (stiffness) as well as the bulk density
	of the FDM-fabricated TPMS bone scaffolds Composed of PAPC-I32
Figure 5	A comparison of the compression modulus (stiffness) as well as the bulk density
	of the FDM-fabricated TPMS bone scaffolds Composed of PAPC-II33
Figure 6	A comparison of the compression modulus (stiffness) as well as the bulk density
	of the FDM-fabricated TPMS bone scaffolds Composed of PAPC-V34
Figure 7	An overall comparison of the compression modulus (stiffness) as well as the bulk
	density of all fabricated bone scaffolds
Figure 8	TPMS designs of all 10 scaffolds
Figure 9	A Schematic Diagram of Material Transport and Deposition in Fused Deposition
	Modeling (FDM) Additive Manufacturing Process
Figure 10	Torsion SimuBone Elastic Curve Regions
Figure 11	Tensile Finding of SimuBone and The Effects of Angle Changes50
Figure 12	Visual comparison of the compression properties of the fabricated TPMS bone
	tissue scaffolds51
Figure 13	Evaluation of Compression modulus, Pore Percentage, and Deposition mass of all
	10 TPMS scaffolds54

Figure 14	TPMS designs (in order of Design 1-10) developed in this study for fabrication of	
	bone scaffolds having complex, porous internal microstructures	58
Figure 15	The boundary conditions of the CFD models	64
Figure 16	Internal pressure contours for all 10 TPMS design	68
Figure 17	Internal wall shear stress (WSS) contours for all 10 TPMS designs	70
Figure 18	Internal velocity streamlines for all 10 TPMS designs	72
Figure 19	External pressure contours for all 10 TPMS designs	74
Figure 20	External Wall Shear Stress (WSS) contours for all 10 TPMS designs	76
Figure 21	External velocity streamlines for all 10 TPMS designs	78
Figure 22	External Cubic pressure contours for all 10 TPMS designs	80
Figure 23	External Cubic wall shear stress (WSS) contours for all 10 TPMS designs	82
Figure 24	External Cubic velocity streamlines for all 10 TPMS designs	84
Figure 25	Bar graphs comparing maximum pressure and wall shear stress with respect t	0
	design 1-10	86
Figure 26	TPMS designs of all 5 scaffold designs	92
Figure 27	A schematic diagram of material transport and deposition in fused deposition	
	modeling (FDM) additive manufacturing process	96
Figure 28	Workflow of CNN code model, image acquisition, model setup, and validation	n .99
Figure 29	Change in accuracy with respect to hyper parameters	104
Figure 30	Change in loss with respect to hyper parameters	106
Figure 31	Change in validation accuracy with respect to hyper parameters	108
Figure 32	Change in validation loss with respect to hyperparameters	109
Figure 33	Change in F-Score with respect to hyper parameters	111

#### Abstract

With the recent advancements within biomedical engineering of bone tissue scaffolds, there is still a need to develop mechanically robust and biocompatible with low immunogenicity for bone regeneration. Additionally, the evaluation of the fluid dynamics of the porous Triply Periodic Minimal Surfaces (TPMS) bone scaffold also shows the need for investigation due to the complex fluid interaction of hemodynamics that occurs with the scaffold internal and external domains. To aid in the development of treating bone fractures, defects, and diseases. Furthermore, with the induction of a wide variety of TPMS architecture that yields different topologies, the Convolutional Neural Network (CNN) model will aid in predicting the TPMS scaffold characteristic to help develop critical design parameters.

Thus, this research has observed biocompatible and mechanically strong materials with bone regeneration applications by evaluating polyamide, polyolefin, and cellulose fibers (PAPC) and SimuBone biomaterial. The TPMS scaffolds are fabricated by fused deposition modeling (FDM) additive manufacturing. Furthermore, the evaluation of fluid dynamics of internal and external effects using the computational fluid dynamics (CFD) method is used to observe the fluid interaction of the TPMS scaffold. Therefore, ANSYS (Fluent with Fluent Meshing) software captures the pressure, wall shear stress, and velocity streamline characteristics. As for the bone scaffold topology prediction, machine learning CNN is used and developed within Python to observe these properties. Accuracy, loss, validation accuracy, validation loss, and F-Score will be recorded to aid in developing the hyperparameters with the CNN platform.

Therefore, the findings show that PAPC compression modulus performance observed that Neovius and Schwarz-Diamond designs have higher levels of compression strength than that of Schwarz-Primitive and Schwarz-Gyroid designs. As for SimuBone biomaterial, it was observed

to be a suitable bone tissue engineering material due to its robust mechanical performance.

Additionally, it is observed that the vertical orientations of P.W. Hybrid showed optimal performance with the compression analysis out of 10 different TPMS designs. It also has suitable mechanical mimicry of human trabecular bone yield strength.

The evaluation of the CFD analysis of the internal and external performance of 10 TPMS scaffold designs showed that Schwarz Primitive yielded superior fluid properties. The wall shear stress was the lowest for analysis, with the external cubic evaluation showing Schwarz Primitive has a wall shear stress value of 3.4 mPa. In addition, its fluid pressure performance was suitable for improving cell viability and survival.

Furthermore, the CNN evaluations displayed the optima hyperparameter for batch size, convolutional layers, dense layers, layer size, and Epoch training as 16, 6, 3, 32, and 25, respectively. A trend can be discerned within accuracy, loss, validation accuracy, validation loss, and F-Score performance, all yielding improved and consistent performance with the 5-replication analysis.

Thus, this research has observed the fluid dynamics, mechanical performance, and topology evaluation of the TPMS bone scaffold. This study will aid in designing and experimenting with bone tissue engineering scaffold development.

#### **Chapter 1: Introduction**

#### Significance, Goals, and Objectives

When considering the future development of bone tissue engineering for treating and regenerating bone fractures, defects, and diseases, there is a significant need to understand porous bone scaffold design development and fabrication for patient-specific treatment.

Evaluating a scaffold's hemodynamics and mechanical strength is crucial to improving the functionality of highly porous bone scaffolds fabricated using biomedical polymer composite material.

Therefore, this study focuses on patient-specific treatment for bone pathology by using porous triply periodic minimal surface (TPMS) scaffolds. The goal is to analyze and observe the computational fluid dynamics of 10 unique TPMS bone scaffold architectures. Furthermore, the mechanical challenges of compression, tensile, and torsion of the scaffold's robust strength are addressed. In addition, 2 biomedical composite materials are used for engineering bone scaffold applications, focusing on repairing fractured or segmented bone defects.

Thus, the objective of evaluating the mechanical characteristics is to fabricate porous and mechanically robust TPMS scaffolds by investigating the mechanical effects of polyamide, polyolefin, and cellulose fibers (PAPC) and SimuBone biomaterial using additive manufacturing fused deposition modeling (FDM) process. Furthermore, the biomaterial yields biocompatible and biodegradable properties. In addition, the mechanical compression performance is also compared to that of the effects of deposition mass and pore percentage.

Furthermore, the computational fluid dynamic (CFD) observation is evaluated for the internal and external geometry of the TPMS scaffolds for the effects of pressure, wall shear stress (WSS), and velocity streamlines. This will provide insight into biological fluid interaction

within the scaffold pores and microstructure characteristics, thus allowing for more improved design applications, as for the topology of the TPMS scaffold holding important in-patient specific designs. Hence, convolutional neural network (CNN) modeling is used. The CNN model will predict the TPMS scaffold's different topologies that were collected from a monochromatic, high-resolution charge-coupled device (CCD) camera to aid in optimizing bone scaffold selection with the find detailing the performance of the framework of the CNN model by the interpolation of the F-Score presentation.

# Literature Review of the Mechanical Influence Characteristic of Bioactive Material of Composite Bone Tissue Scaffolds

Various composite materials have been synthesized to fabricate bone tissue scaffolds. Oladapo *et al.* [1] investigated a lattice design using 3D printing technology for bone implants. The material used was a bio-composite polyether ether ketone (PEEK). In addition, calcium hydroxyapatite (cHAp) was used to improve bone-implant interfaces and osseointegration of PEEK composite. Furthermore, the FDM method and a surface treatment strategy were used to produce a microporous scaffold. PEEK osteointegration is slow and can be enhanced by coating the surface with a bioactive cHAp to optimize mechanical and biological properties for bone implants. It was observed that the mechanical performance of cHAp-coated PEEK was improved due to the increase in the degree of crystallinity and accumulation of residual polymer.

Han et al. [2] investigated fused deposition modeling (FDM) for printing pure PEEK and carbon fiber-reinforced PEEK (CFR-PEEK) composites, focusing on mechanical properties. Furthermore, the test subjects' surfaces were modified via the post-processing technique of polishing and sandblasting. Composites showed satisfactory biocompatibility levels for both materials with and without surface alterations.

Manzoor et al. [3] investigated the effect of 3D printing with PEEK/HA composites on material formulation, mechanical properties, and bioactive potential. Nano-hydroxyapatite (nHA) was added to PEEK to aid in its bioactivity. Ferroni et al. [4] investigate 3D printed polyetheretherketone (PEEK) scaffolds coated in methacrylate hyaluronic acid (MeHA)-hydroxyapatite (HAp) hydrogel. The methodology will consist of developing and characterizing the structural scaffold, using MeHA-HAp post-process of infiltration and UV photocrosslinking, and investigating the biological characteristics of human mesenchymal stem cells (MSCs). Furthermore, the interconnected porous PEEK matrices were developed using fused deposition modeling (FDM).

Zheng et al. [5] investigated the fused filament fabrication (FFF) 3D printing process on PEEK/HA, which is used for highly controllable mechanical characteristics and osteogenesis in bone tissue engineering. Furthermore, the pore size of HA content and the printing direction were analyzed on the mechanical characteristics of the PEEK/HA structure scaffold.

Kang et al. [6] investigated the mechanical properties of a 3D-printed fabricated PEEK/HA composite filament. Combining a bioactive ceramic within a PEEK structure was expected to enhance pure PEEK's bio inertia and hydrophobicity.

Singh et al. [7] investigate tensile, compression, and flexural mechanical performance for a novel chitosan-reinforced poly-lactic-acid (PLA) scaffolds using a filament fabrication (FFF) 3D printing process.

Ali *et al.* [8] fabricated on-woven fibrous and porous bone tissue scaffolds, composed of polyurethane and Nylon-6 (mixed with natural gelatin) based on electrospinning. They observed that the fabricated composite scaffolds not only had a high level of tensile strength, stiffness, and

elongation, but also were bioactive (capable of forming bone apatite like layers). In addition, the scaffolds were hydrophilic and showed osteoblast cell proliferation.

Similarly, Abdal-hay *et al.* [9] used air jet spinning (AJS) to fabricate non-woven bone tissue scaffolds. It was observed that "polymer concentration" was a significant factor affecting the morphological properties of AJS-fabricated nylon-based tissue scaffolds. In a research work by Wear *et al.* [10] ultrasonic attenuation (having a frequency in the range of 1.5 and 3.5 MHz) was utilized for the fabrication of bone-like phantoms, based on parallel-nylon-wire arrays (having a diameter of 150 - 300 μm).

Das *et al.* [11] utilized selective laser sintering (SLS) to fabricate biocompatible bone scaffolds (composed of Nylon-6) having a periodic and biomimetic internal architecture. Similarly, Chen *et al.* [12] investigated the design and mechanical compatibility of Nylon-based bionic cancellous bone structures. Selective laser sintering was used to produce honeycomb structures with a porosity range of 59% and 96%. The result of a compression test showed that the fabricated structures had a stiffness comparable to that of human vertebrae.

Pant *et al.* [13] used electrospinning to fabricate porous chitin butyrate-coated/Nylon-6 composite scaffolds for bone regeneration. It was observed that the electrospun scaffolds were cytocompatible and had bone formation ability.

Abbasian *et al.* [14] investigated the functional properties of a biomimetic nanocomposite material composed of Nylon 6 as well as Baghdadite together with cuttlefish bone (utilized as a sacrificial material) for the fabrication of hierarchical and porous microstructure scaffolds for bone regeneration. It was observed that the presence of Baghdadite in the Nylon 6 matrix significantly enhanced not only the bioactivity and degradation rate but also the mechanical properties of the fabricated porous scaffolds.

Looking at the capabilities of Nylon-66, Mehrabanian *et al.* [15] fabricated composite scaffolds made of nano-hydroxyapatite (n-HA)/Nylon-66, using a salt-leaching/solvent casting process. They observed that a uniform distribution of n-HA within the nylon network led to the formation of scaffolds with adequate mechanical strength. Their findings also showed that n-HA/Nylon-66 scaffolds with a porosity of 75% had a compressive strength and elasticity modulus comparable to those of natural cancellous bone.

As the above-mentioned literature review implies, a broad range of composite materials are developed to fabricate bone tissue scaffolds. However, few works have focused on the characterization of the functional properties of the PAPC composite materials. PAPC is a medical-grade polymer composite (as discussed in Chapter 2). This gap is addressed in this work by investigating the mechanical properties of PAPC composite materials, including PAPC-I (Nylon-6-based), PAPC-II (Nylon-6-based), and PAPC-V (Nylon-66-based).

Note that the main disadvantage associated with PEEK is that it (unlike PAPC) is *not* a bioactive polymer for bone regeneration. Additives are, therefore, required to make PEEK bioactive (which significantly decreases the mechanical properties of PEEK), while PAPC is a bone-like, bioactive material and thus can be directly used for bone tissue engineering. In addition, PEEK (unlike PAPC, which allows for the formation of an excellent implant-to-bone interface) may result in low-grade infection as well as total body rejection. Furthermore, PEEK (unlike PAPC) is radiolucent and, therefore, incapable of showing bone bridging during the fracture healing process.

The material and methods used in this study are discussed in Chapter 2: Material and Methods; this includes FDM-based fabrication of triply periodic minimal surface (TPMS) bone scaffolds composed of PAPC-I, PAPC-II, and PAPC-V in addition to characterization of the

compressive properties of the fabricated bone scaffolds. The results of this work are presented in Chapter 2: Results and Discussion. Finally, the conclusions, as well as future work, are presented in Chapter 2: Conclusions.

## Literature Review of Material Transport of Triply Periodic Minimal Surface (TPMS) Bone Scaffolds

Wang et al. evaluated the mechanical properties, permeability, conductive cell adhesion, and proliferation of a TPMS Primitive structure (composed of Ti6A14V and fabricated using selective laser sintering (SLM) process). The CFD analysis of a single unit model and a cytotoxicity test showed that the permeability of the designed Primitive structure (with varying pore size and porosity) was acceptable for bone tissue replacement. In addition, the fabricated scaffolds were non-cytotoxic and had a high level of printing accuracy, mechanical properties (comparable to that of real bone), and transport capacity [16].

Ma et al. investigated scaffolds with different porosities, verifying performance, and revealing the effect of their permeability for cell growth, with the use of selective laser melting (SLM) for the manufacturing method, compressive testing for mechanical characterization, CFD for permeability analysis, and cell cultivation for biocompatibility for a model Gyroid architecture. Results yielded that elastic modulus and permeability displayed ranges of human bone likeness, with a morphological evaluation yielding that fabrication accuracy significantly affects designed porosity and an in-vitro analysis showing permeability has an impactful role in cell proliferation. Overall, the study aided in developing scaffold parameters for mechanical properties, permeability, and cell growth for better bone development [17].

Ali et al. investigated eight different bone scaffold models (constant porosity of 80%) for fluid flow within the scaffolds using CFD analysis. The models were designed computationally

using k3dsurf to produce the TPMS and lattice-based structures and ANSYS Fluent software for the CFD analysis. The finding displayed that scaffold design significantly affects permeability within narrow channel variation, producing the highest permeability. Furthermore, the scaffold model affects wall shear stress and its distribution in the scaffold. In addition, wall shear stress along the wall of the scaffold showed that a relationship between the design of the model and distribution statistics of wall shear stress is nonexistent [18].

Kim et al. investigated flow behaviors in different TPMS scaffolds, measuring the pressure drop on two other structures at three different porosities with the architecture of Gyroid and Body-Centered Cubic (BCC) models. The classic Ergun equation is used to understand the flow through random sphere packing. Thus, the results from the Gyroid scaffolds agreed well with the Ergun equation for laminar and turbulent regimes. The BCC scaffolds differed within the transitional and turbulent regimes. The velocity field of the BCC recirculation flow at high flow rates and large-scale flow inhomogeneity pressure drops in the scaffolds no longer followed the Ergun equation at higher Reynolds numbers [19].

Li et al. investigated TPMS scaffolds manufactured By Selective Laser Melting (SLM), evaluating surface curvature on mechanical response and mass-transport property and/or permeability of the scaffolds. Methods used for assessing mechanical and permeable properties of the scaffold are scanning electron microscopy (SEM) and finite element analysis (FEA), used to analyze the influence mechanism of curvature on structural fracture and deformation behavior. Thus, the results showed that uniform porosity leads to a more concentrated curvature distribution of the same unit, yielding improved trade-off of mechanical and mass-transport properties for scaffolds. Furthermore, with a porosity of 55%, a compressive elastic modulus and permeability of the Diamond tensile (Dte) structure are increased when compared to the

Diamond unit. In addition, fusion structures can improve permeability performance at the cost of mechanical properties. Overall, this study showed that surface curvature significantly influences the mechanical and permeable properties of the scaffolds that aid in the development of bone tissue engineering [20].

Pires et al. investigated average WSS for Schwartz diamond and Schwartz gyroid scaffolds using different topologies and meshing elements for CFD analysis and applying algorithm simulation to aid in designing bone tissue engineering scaffolds with a specific average WSS. The results yielded that tetrahedral elements have WSS levels 35% higher than that of the non-smooth surface topology of hexahedral elements. Furthermore, the algorithm displays to have obtained a WSS level of around five mPa (physiological range) within an established 100 iteration limit [21].

Pires et al. produced a comprehensive review of recent studies using CFD analysis within bone tissue engineering. Evaluation of mechanical and fluidic characteristics of a selected scaffold combined with scaffold architecture can lead to optimization in one portion and a hindrance in another. Thus, designs that have been shown to improve permeability normally decrease average wall shear stress. In addition, there are few specific applications of scaffolds other than the use for in-vitro bioreactor environments. Furthermore, there is a shortage of studies that combine CFD with optimization methods to improve scaffold design [22].

Kumar et al. investigated two TPMS structures (I-graph wrapped package (IWP) and Diamond with porosities of 50%, 60%, 70%, and 80%) that have been mathematically modeled using TPMS equations with the use of systematic fluid flow simulations for evaluation of permeability, wall shear stress (WSS), pressure distribution, velocity distribution, and pressure drop for the importance of suitability of scaffolds and bone substitution. The finding details that

the IWP structure shows improved fluid accessibility compared to the diamond structure regarding permeability and WSS; this is also adequate for mesenchymal stem cells (MSC) osteogenic differentiation. Furthermore, a higher velocity at the center of the structure detailed the accelerating capability of the structure, which is beneficial for nutrient transport and promotes cell migration to deeper sections of structures [23].

Deng et al. investigated selective laser melting (SLM) fabrication, producing four porous titanium alloy scaffolds with porosities of 65% and pore sizes of 650 µm. With the use of animal implants, bone tissue growth can be evaluated with the use of in-vivo, along with Micro-CT and hard tissue section analyses being performed. The finding yielded that diamond lattice unit bone growth is superior to the four topological scaffolds. The CFD analysis of the diamond lattice unit was shown to have the most negligible internal velocity difference; in addition, the fluid flow path yielded the longest, aiding bone growth. Overall, this study provided a new theoretical basis for the design of bone scaffolds for future studies [24].

Ali et al. investigated four different scaffold configurations of Schwarz architecture (00, 300, 450, and 600). Using darcy permeability and fluid flow-induced wall shear stress evaluated with computational fluid mechanics. The finding detailed that permeability decreased by 25%, 5%, and 15% with respect to 300, 450, and 600 in relation to the model of 00. The WSS decreased by 14% for 300 models and increased by 20% and 10% for 450 and 600. Overall, this study aids in the functionality of Schwarz architecture for bone tissue engineering [25].

Singh et al. investigated the manufacturing of selective laser melting (SLM) TPMS scaffolds of Neovius architecture, using CFD analysis for estimating fluid flow with a non-Newtonian blood fluid model. In addition, a static compression test evaluated the strength of open cell Neovius structure and an in-vitro cell culture (Alamar blue was used). The finding

yields that permeability for an open cell porous scaffold with a Neovius architecture is of the same magnitude order as human bone, as for the elastic modulus and compressive strength yield peak values of 3.71 GPa and 205 MPa, respectively. Overall, the findings detail that the values are comparable to human bone [26].

Guerreiro et al. investigated a novel method of scaffold selection that is based on the application of tortuosity inside TPMS structures, with the use of CFD simulation to validate this methodology. The findings detail that tortuosity and CFD outputs imply that tortuosity can be used for early indication of scaffold viability; this favors scaffolds with complex curvature-dependent streamlines [27].

Li et al. investigated novel strut-based scaffolds and design development using 3D printing for experimental use, allowing for modification to topological, mechanical, and mass transport properties. Scaffold structures were parameterized in terms of mechanical and mass transport properties for simulated analysis. The findings yielded simulation and experimental results that display that the scaffolds present controllable deformation modes and mass transport characteristics. The elastic modulus and permeability of the scaffold meet the range of cancellous bone qualities. Overall, the designs allow scaffolds to decouple and individually tailor multiphysics properties at a given porosity [28].

As the Literature Review section implies, many studies have examined porosity variations and a small collection of TPMS structures using fluid dynamics to develop bone tissue scaffolds. There is a need for the identification and characterization of a broader range of bone-like scaffolds with optimal properties for bone tissue engineering.

It was observed that Primitive had a relatively simple structure, allowing for easier design and characterization of flow properties, as well as good compressibility and permeability in the

structure [16, 20]. Gyroid structure had self-supported features along with excellent mechanical properties [17]. In addition, Gyroid shows an excellent complex internal structure, aiding in fluid properties [19], along with adequate permeability and fluid tortuosity. Furthermore, the highest permeability can be seen at a porosity of 80%, aiding cellular growth [20, 21].

It was also reported that investigating geometrical parameters on WSS and permeability would be inevitable for scaffold design toward bone regeneration [18]. Body-centered cubic (BCC) scaffolds are also used for their open-cell structure capabilities [19]. Schwartz diamond design shows good cellular growth due to high permeability, along with fluid tortuosity that aids in cell-scaffold interaction [21]. Studies have shown that, overall, TPMS scaffolds are more permeable than lattice scaffolds. An example of this design is Schoen I-WP [22]. Studies have shown that Schoen I-WP has better WSS and permeability [23]. Choosing scaffolds with high porosity and pore size is essential to improve bone growth and ensure scaffold strength [24]. Schwarz designs have desirable bone scaffold characteristics due to their high surface area-to-volume ratio [25].

TPMS architecture has been shown to have good porous structures for interconnected pores, along with improved mechanical and physiological properties. In addition, some studies show that they can be optimal bone implants for regenerative medicine [26, 27]. Thus, TPMS designs have received more attraction for their excellent performance compared to lattice scaffolds [28].

However, the knowledge gap presented here requires a more comprehensive selection of the TPMS structure for bone scaffold fabrication. Many scaffolds presented in the literature for bone tissue engineering were simply chosen based on their prior mechanical performance. At the same time, an in-depth analysis and understanding of the complex dynamics of fluid flowporosity interactions would be critical for optimal bone tissue regeneration. This study addresses this gap by analyzing the fluid dynamics of a broad range of critical TPMS structures.

This will aid in selecting an optimal design for 3D fabrication utilizing additive manufacturing methods. Thus, this study aims to fill this knowledge gap by observing a comprehensive collection of ten TPMS structures as a collective whole to study the fluid properties with a uniform porosity to capture the true essence of its fluid behavior.

The TPMS structures can be seen in Figure 1, which is further delineated in Chapter 4: Scaffold Design. Also, this study covers the analysis of internal flow, focusing on the fluid properties of pressure contour, wall shear stress (WSS), and velocity streamline, which can be seen in Chapter 4: Results and Discussion to understand how the TPMS structures' internal flow behavior will respawn. In addition, another knowledge gap is satisfied with the analysis of external flow evaluated to observe how environmental fluid behavior will affect the TPMS scaffold toward the identification of optimal designs, as detailed in Chapter 4: External Flow Simulation.

# Literature Review of Mechanical Properties of Bone-Like, Porous Tissue Scaffolds with Medical-Grade Material for Bone Regeneration

Zhifei et al. investigated TPMS scaffolds, which embody trabecular bone-mimicking hyperboloidal topography and a unique structure that aids in developing cellular stem cells.

Therefore, Zhifei discusses the effect of pore size, porosity, and pore shape parameters and their influences on mechanical properties, permeability, and curvature [29].

Seyed et al. investigated the mechanical properties of compression, tension, bending, and torsion analysis for significant load-bearing implants. Thus, the aim is to evaluate 2 TPMS designs (gyroid and diamond) for the mechanical properties of bone (porosity, stiffness, and

strength). The findings yielded that both TPMS designs' stiffness and strength are comparable to cortical bone; in addition, both TPMS designs showed bone mimicry for the physical and mechanical properties of cortical bone, making them viable for bone replacement [30].

Xiaoyu et al. investigated additively fabricated polyether ether ketone/silicon nitride (PEEK/SiN) scaffolds with a TPMS architecture. The TPMS structure has been shown to have advantages due to its large surface area in addition to its uniform stress distribution. Furthermore, the TPMS scaffold exhibited a mechanical property with favorable damping characteristics and mimicked the physical attributes of trabecular bone. The PEEK/SiN material yielded osteogenic differentiation capabilities, thus resulting in the selected material being a favorable option with bone tissue engineering [31].

Dmitriy et al. fabricated TPMS gyroid geometry using 2 different Electron Beam Melting (EBM) methods to manufacture the scaffolds. The surface morphology, geometry, and mechanical properties were evaluated using electron microscopy, X-rays, compression, and tension analysis. The different manufacturing methods yielded in the TPMS structures with varying wall thicknesses; in addition, the quasi-elastic method yielded 1.5 GPa elastic modulus, similar to human bone. Using Finite Element (FE) analysis, the simulation showed that the elastic wall regions are the primary affected deformation section. Furthermore, the gyroids developed by the 2 methods were viable for mimicking the mechanical properties of bone [32].

Ashish et al. investigated the mechanical performance of TPMS Schwarz P. scaffold design under uniaxial compression. Additionally, the comparison of 2 different polymers (PLA and ABS) with varying compression speeds was evaluated. The PLA polymer showed less compressibility than the ABS material, with both tending to failure. The peak stress of PLA was shown to have a higher value than that of ABS. Furthermore, ABS displayed less variation in

compression performance samples and the deformation rate. Thus, an analysis of the 2-material polymer shows the effect of mechanical behavior when compared at different strain rates [33].

Maryam et al. investigated the environmental dependency of mechanical responses of additive manufacturing porous scaffold with PMMA material. A TPMS scaffold design of Primitive and Schoen-IWP is used for this study. The TPMS scaffolds were tested under a compressive load in ambient and fluidic environments; additionally, the investigation showed that the compressive performance of the TPMS scaffolds has a significant loss in performance within the fluidic conditions compared to that of the ambient settings. Furthermore, the mechanical analysis showed that the compressive properties and flexural stiffness are within the ranges of trabecular bone in both scaffolds. In addition, the study showed that the mechanical behavior of additive manufacturing scaffolds is controlled by topology and morphology [34].

de Aquino et al. investigated the mechanical effects of orientations during the fabrication of a TPMS scaffold in producing an FDM process. The analysis of compressive load on the directional effects of 0° and 90° of the fabrication directions shows significant changes in the compressive modulus. Thus, the TPMS primitive, gyroid, and diamond scaffold design was used in this study. Hence, the primitive yields the optimal performance in the compression analysis; in conclusion, the findings have detailed that the loading direction significantly affects the scaffolds' compressive strength and elastic modulus [35].

Pearlin et al. investigated the mechanical properties of the TPMS scaffold design of gyroid with different sets of pore sizes. Thus, the additive manufacturing method of selective laser melting (SLM) was used in fabricating a gyroid scaffold of varying pore sizes from 250, 300, 350, and 400 µm. The analysis shows that increased pore size led to decreased compression strength. For the pore size, 250 µm yielded a compressive strength of 205 MPa. Additionally, a

biocompatibility analysis was performed on the bone scaffold. Using human mesenchymal stem cells (hMSCs) showed that gyroid with greater pore size yielded the highest biocompatibility [36].

Ekaterina et al. investigated the effects of mechanical performance 3D-cell culture and in vitro analysis on lattice and TPMS designs of Diamond, Gyroid, and Primitive scaffolds. The scaffold material is hydroxyapatite for all 3 scaffolds; additionally, shared among all microarchitectures, the minimal constriction is 0.8 mm diameter. Furthermore, the compression strength of the gyroid and diamond scaffold in comparison to the primitive and lattice designs showed that the gyroid and diamond have significantly higher compression strength. The in vitro culture of human bone marrow stromal cells showed no difference within the scaffolds. In addition, the TPMS scaffolds of diamond and gyroid showed higher bone ingrowth and bone-to-implant contact in vivo. Thus, the diamond and gyroid show the most effective bone tissue scaffold in bone tissue regeneration [37].

Castro et al. investigated the mechanical properties of a TPMS gyroid design by adding 2 different porosity percentages (50% and 70%). The additive manufacturing method used is 3D MultiJet printing, which displayed significant accuracy. Furthermore, elasticity has been shown to be an essential parameter for promoting cellular growth and proliferation. In addition, a homogenization method was used to determine the stiffness of the scaffold as a function of porosity [38].

Dvina et al. investigated the generation of a TPMS scaffold (Diamond, Gyroid, and Schwarz P) fabricated with polycaprolactone (PCL). In addition, a finite element (FE) numerical analysis was conducted to evaluate Young's modulus and an experimental evaluation of cell migration using an in vitro study. The analysis of the in vitro study shows that Diamond, Gyroid,

and Schwarz P cell migration assays, adipose-derived mesenchymal stromal cells (AdMSC), managed to migrate farther on the PCL material. Additionally, the migration rate was accelerated along the surface of the coated scaffolds with the addition of calcium-phosphate-based appetite. Therefore, an integration process using an additive manufacturing method is essential. The improved workflow showed development in biological and mechanical functionality and improved regeneration of enhanced cell migration [39].

Zizhen et al. investigated the effect of porosity on the mechanical properties of a periodic cellular structure. Using TPMS scaffold designs (Skeletal-IWP, Skeletal-Diamond, Skeletal-Gyroid, Sheet-Gyroid, Sheet-Primitive, Sheet-IWP, and Sheet-Diamond) that were developed with a series of modeling software to conduct a compressive analysis of mechanical properties on each cellular structure. The finding yielded that high porosity groups showed that the yield strength of the low porosity variants displayed those 3 times higher, and the modulus is 2.5 times larger. The experiment showed that the fabricated scaffold is related to porosity and Young's modulus. However, it is seen that high and low porosity structures failed through distinctive mechanisms, with high porosity breaking down via buckling and the latter via micro-fracturing [40].

Lei et al. investigated the compression–compression fatigue behavior and the underlying fatigue mechanisms using a TPMS gyroid design. The findings detailed that the gyroid TPMS design showed that both cycling ratcheting and fatigue damage aid in the failure. In addition, the gyroid design has superior fatigue resistance due to its smooth surface area. A post-processing sandblasting treatment has also been shown to enhance fatigue resistance by alleviating adhered powder particles, etc. [41].

Roberta et al. investigated the combination of AM and computational methods to develop a porous scaffold with complex microstructure and quality mechanical performance similar to cancellous bone. Thus, the TPMS scaffolds used are Schwarz P. and Schwarz G. designs developed using computational methods. It has shown that geometry has complex and highly pore interconnective designs. Schwarz P. and G. have been shown to play a role in mechanical cell proliferation; several design parameters can alter the scaffolds' structure effect and performance. For example, wall thickness affects the elastic modulus and compressive strength, which has implications for biological performance [42].

Sanjairaj et al. investigated porous bone implant designs based on TPMS Schwarz P. design; 12 different versions were developed. It was fabricated from a ceramic material (Alumina) using Lithography-based Ceramics Manufacturing (LCM) technology. The 12 variations of Schwarz P. have different pore sizes that range from 500 to 1000 µm. The finding detailed that the material and porous of the Schwarz P. led to a poor performance of compressive modulus that is comparable to native bone. This led to adopting bone implant design to mitigate the stress-shielding effect [43].

The literature review discusses the relative findings regarding the mechanical and biological performance of TPMS bone scaffolds. However, the gap in the literature is the lack of variation in the TPMS scaffold design for consistent use and valuation of Schwarz P., Schwarz G., and Schwarz D., which have been significantly evaluated.

Additionally, very few have investigated the TPMS scaffold design, such as Neovius, Icosahedron, P.W. Hybrid, and many more. This is not due to the lack of performance of the scaffold's mechanical strength or biological response but more of the nuance of the topology of the structure. Furthermore, most studies only evaluate a few sample design variations; this can

lead to mechanical performance variation and inconsistencies between studies, thus creating a knowledge gap. Therefore, this study evaluates 10 different TPMS designs, which will be assessed for their mechanical properties, as shown in Chapter 3: Scaffold Compression Analysis and Optimal TPMS Scaffold Design of the results.

Similarly, our study recognizes the crucial need for diversity in TPMS materials. While PEEK, PCL, PLA, and Hydroxyapatite have demonstrated quality performance, they still lack the variety of newer and improved biological materials. To address this, our study introduces new material for evaluation. SimuBone, a biocompatible material with an additive mixture of PLA, offers enhanced mechanical strength. The material and its potential implications are elaborated in Chapter 3: Materials of the methods.

## Literature Review of Machine Learning Network In-Process to Assess Complex Porosity of Bone Tissue Scaffolds

When investigating the application of the convolutional neural network model for inprocess assessment of the complex porosity of additively manufactured bone tissue scaffolds,
Insight can be seen within the investigation that *Joshua et al.* evaluated an image-based
intelligence platform, the CNN, to aid in the prediction of the properties of bone scaffolds.
Furthermore, the scaffold was fabricated using fused deposition modeling (FDM). The finding
details the impact of scaffold design, material, and process parameters, along with displaying the
optimal fabrication method for mechanically strong, dimensionally accurate, and porous
composite bone scaffolds. Therefore, the CNN model showed the learning capability of complex
composite material deposition dynamics and scaffold porosity prediction. Thus, this study
provided an innovative, robust, porous bone scaffold for tissue bone engineering [44].

Additionally, *Yongtao et al.* investigated bionic bone scaffolds designed by CNN framework with anisotropic mechanical characteristics that mimic native bone. The anisotropic properties were solved using CT images of bone tissues. Furthermore, the CNN platform was trained and validated using a prediction method of the heterogeneous finite element (FE) model. The CNN model uses the desired given elasticity matrix. The model then would develop the design using a conventional method. Thus, the finding showed that the CNN model closely designs a scaffold that mimics native bone tissue. Therefore, this framework shows significant implications that can be achieved with CNN models for clinical applications [45].

Bo et al. present a method for high-dimensional multi-property optimization of 3D-printed structure materials using a machine learning (ML) cycle. In addition, with consisting of the finite element method (FEM) and 3D neural networks. Thus, the results showed their designs produced a microscale heterogeneous structure of a biocompatible elastic modulus with higher strength. Therefore, the ML designed a model to fix the macroscale of irregularly shaped animal bones. Thus, their ML design displayed a higher load-bearing capacity than the uniform design. Hence, the method provides a fast and intelligent architectural material design tailored to mechanical, physical, and chemical characteristics [46].

Silvia et al. investigated TPMS scaffolds using the ML model to find input parameters and the mechanical and morphological properties of the structure. Additionally, 3 different ML models were developed to evaluate linear and non-linear approaches. The non-linear model showed a median error of less than 3% and found a coefficient of higher than 0.89 for desired features. Thus, the approach displayed the design of hydroxyapatite TPMS scaffolds with characteristics from a natural trabecular-like hydroxyapatite scaffold. Hence, the findings

showed that the ML model could effectively develop a TPMS scaffold with the desired biomechanical properties for bone tissue engineering [47].

Ye Wei et al. analyzed a dataset using the learning approach to advance the multiobjective cellular material design. Using additive manufacturing (AM), the cellular scaffold is applied for orthopedic implantation with adjustable parameters for elastic modulus, high yield strength, and fewer weights. The finding detailed several lightweight scaffold models with desirable elastic modulus and ideal yield strength, thus providing an innovative way for accelerating the discovery of complex cellular materials [48].

Darshil et al. provide a novel approach to generating TPMS and interpenetrating phase composites (IPC). They use a weighted combination of Schwarz P., Diamond, and Schoen's F-RD topology to develop the IPCs. It has shown that the elastic properties are satisfying with the mixture of TPMS and IPC structures with the evaluations of finite elements (FE). The findings detail that the IPCs generated with the novel method yield improved mechanical characteristics. Additionally, the opposite shows that the mechanical characteristics of IPC geometric mapping yield a shortcoming within the applications. They use deep learning-based computational approaches to predict the TPMS-based IPCs for a targeted, effective elastic property. Thus, a 5-layer deep neural network (DNN) is shown for 6 geometrical parameters prediction based on 5 different material properties. The proficiency of the DNN has demonstrated the capability to better the parameters prediction performance. Therefore, DNN aids in showing the predictions of the combinatorial TPMS and IPCs fraction of the computational cost, thus playing a vital role in design optimization [49].

Jordi et al. developed and trained a CNN model to aid bone segmentation in computed tomography (CT) scans. The CNN model was trained with 6 scanners and 20 patients who had

undergone craniotomy and cranioplasty using additively manufactured (AM) to fabricate a skull implant to be placed as the gold standard. The findings of the CNN model significantly overlap with the gold standard. Furthermore, this resulted in the mean Dice similarity coefficient of 0.92  $\pm$  0.04; the CNN STL model also yielded a mean surface deviation ranging between -0.19 mm  $\pm$  0.86 mm and 1.22 mm  $\pm$  1.75 mm. Thus, no significant differences were evaluated with the CNN STL models' mean deviations from the six CT scanners. The CNN model could accurately predict the implant, hence making this applicable to patient-specific treatment [50].

María et al. investigated using 3D CNN modeling to predict the mechanical properties of the robust scaffold model. Thus, the CNN model was trained using digital tomography from the CAD models. The addition of artificial intelligence (AI) and/or machine learning (ML) in developing the methodology aids in a novel approach within the area of tissue engineering scaffolds. This methodology has led to several application uses in the tissue engineering domain, along with filing gaps for discussion and future proposals sections of the research study [51].

Darlington et al. developed a CNN model to identify and classify Airbrushed,
Electrospun, and Steel Wire scaffolds. The CNN model is a 6-layer CNN framework trained and
validated based on 3000 images with its respective scaffold structures. Thus, the finding
displayed that the CNN model achieved an accuracy score of 99.44% for a 3-class CNN model.
Therefore, it can evaluate complex machine-learning problems for abstract spatial contexts and
screen complex, biological, and fibrous structures in cortical bone and fibrous shells [52].

Joseph et al. discussed that TPMS scaffold-like gyroid can mimic the mechanical properties and characteristics of bone by controlling the relative density within the scaffold. Additionally, the advantage of the structure is that it can aid in cell immigration due to its infinitely smooth architecture and relatively high fluid permeability [53]. Furthermore, Roberta

et al. observed that the biomimetic TPMS porous scaffold shows cell adhesion migration and proliferation. TPMS designs are versatile for developing the sheet scaffold, allowing it to satisfy several requirements and characteristics [54]. Additionally, it has been shown that the TPMS scaffold can support bone formation by mimicking the biological bone tissue to integrate well with the surrounding tissue [29, 55].

Veronica et al. discuss using an aggregated artificial neural network (AANN) to evaluate layer thickness, time delay between layer deposition, and print orientation effects on scaffold mechanical properties to develop optimal 3D printing parameters for creating small porous structures. Thus, Pareto font optimization was used to identify the ideal parameter conditions for developing scaffolds with desirable mechanical properties. Therefore, the developed method showed efficient management and optimization of the porous scaffold to overcome the design challenges [56].

The literature review discusses the relative findings regarding the mechanical and biological performance of TPMS bone scaffolds using machine learning and artificial intelligence methods. However, there are gaps regarding investigating different versions of the TPMS architecture. Most analyses have focused on the TPMS Schwarz family types, looking for optimal performance of the TPMS structures within bone tissue engineering.

Nevertheless, designs like Neovius and Schoen I-WP have been shown to have significant mechanical properties. In addition, it is used in the application of biological fluids. Thus, these sections can be seen within Chapter 5: Design Experiment.

Furthermore, recent CNN models have observed the effects of compression modulus or elasticity when dictating the performance of the TPMS scaffold. However, evaluating the TPMS scaffold by topology and porosity depictions is just as essential. Thus, the results of Chapter 5:

CNN Hyperparameter Optimization show the finding of an optimized CNN model for depicting these characteristics, aiding in filling this gap within the knowledge.

# Chapter 2: Investigation of the Influence of Nylon-6 vs. Nylon-66 on the Mechanical Performance of Composite Bone Tissue Scaffolds

# **Goal and Objectives**

Bone tissue engineering is an emerging field of regenerative medicine, combining the principles of tissue engineering, stem cell biology, as well as biomedical engineering to create functional tissues that can be implanted into a patient with the aim to repair or replace damaged/missing bone.

The mechanical strength of a fabricated scaffold is an essential factor in the success of tissue engineering as it needs to be strong enough to withstand the mechanical stress of the body while allowing nutrients as well as oxygen to flow through to the scaffold cells. The mechanical strength of a scaffold can be improved by increasing its porosity, which allows more cells to attach to the scaffold and create stronger tissue. Additionally, the scaffold can be mechanically enhanced using polymer composites to increase strength, flexibility, and biocompatibility. In addition, using composite materials with aligned fibers (such as PAPC) can increase mechanical strength in the direction of the fibers.

The goal of this work is to fabricate porous, biologically active, and mechanically robust bone tissue scaffolds for the treatment of bone fractures, defects, and diseases. In pursuit of this goal, the overall objective of the work is to systematically investigate the mechanical properties of three PAPC materials, i.e., PAPC-I (Nylon-6-based), PAPC-II (Nylon-6-based), and PAPC-V (Nylon-66-based), composed of polyamide, polyolefin, and cellulose fibers, using complex triply periodic minimal surface (TPMS) bone scaffolds fabricated by fused deposition modeling (FDM) additive manufacturing.

#### Material

The selected material for fabricating the TPMS scaffolds is PAPC (Innovative Plastics and Molding, Inc. doing business as FibreTuff, Perrysburg, Ohio, USA; being under the patent numbers of 11497837 and 10233309), which is a medical-grade biocompatible composite, produced from polyamide, polyolefin, and cellulose fibers. The material compounds display a high strength-to-weight ratio, yielding a high potential of flexibility with non-bioresorbable qualities.

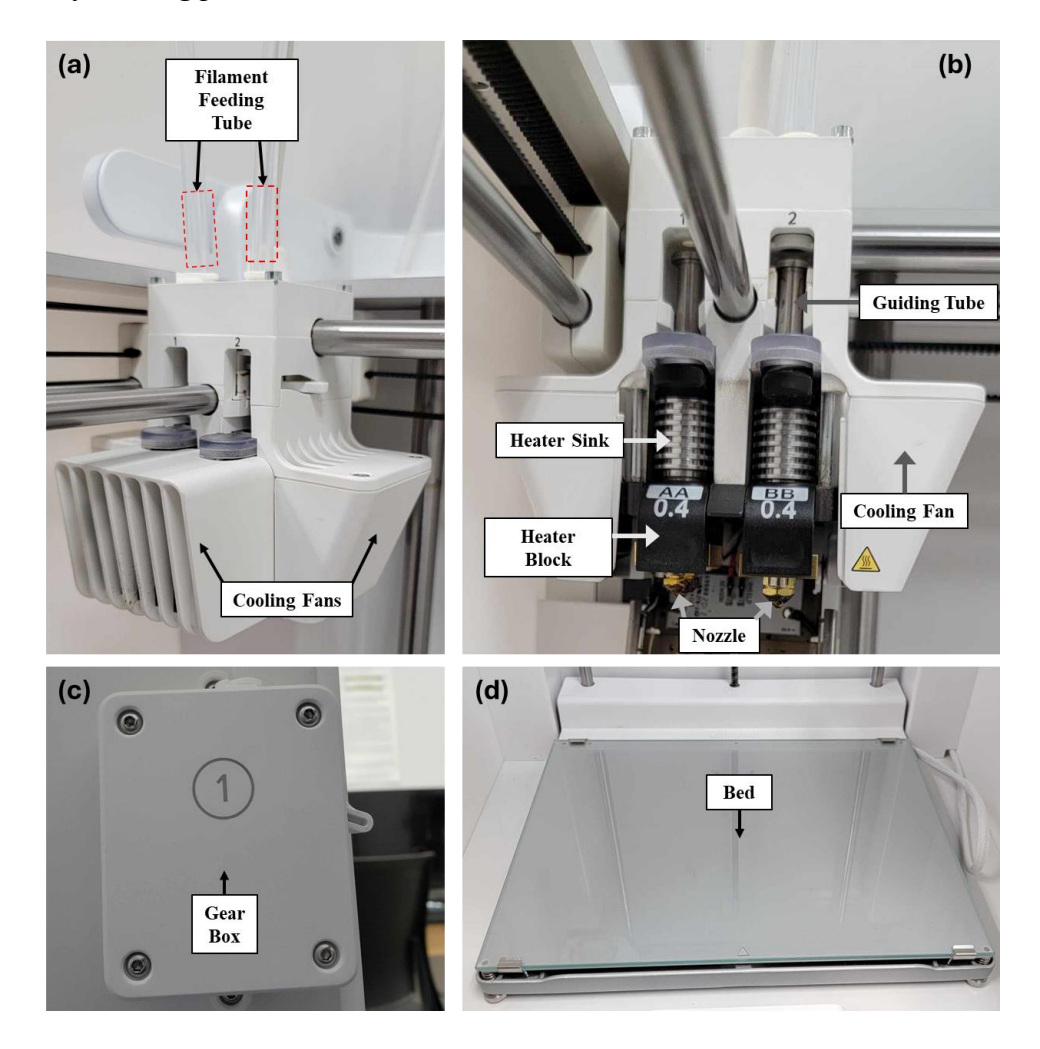
PAPC-I as well as PAPC-II are a composite mixture of Nylon 6, which is a material shown to have high tensile strength and elasticity. As for PAPC-V, it is a composite mixture of Nylon 6-6 which yields high mechanical strength, rigidity, and good stability, which are desirable features for bone regeneration.

#### **3D-Microfabrication Process**

Figure 1 demonstrates a schematic diagram of the fused deposition modeling (FDM) additive manufacturing process. The PAPC composite materials (used in this study) are fed as a thin monofilament (having a diameter of 2.85 mm) into the extruder head, where a stepper motor not only guides the filament along a Bowden tube but also makes the filament contact with the heating block, which turns the filament into a molten polymer flow [57, 58]. The molten filament has the resulting characteristics of a non-Newton fluid [59]. The heating block controls the viscosity as well as the rheological properties of the molten filament. The polymer flow is then guided through a microcapillary nozzle and subsequently extruded along the build plate as a laminar flow. The deposition of the molten polymer flow initially builds the first layer of a bone scaffold model. Furthermore, the following iterations of layer-by-layer material disposition bond the deposited layers into a solid scaffold structure (as exemplified in Figure 3).

Figure 1

A schematic diagram of material transport and deposition in fused deposition modeling (FDM) additive manufacturing process.

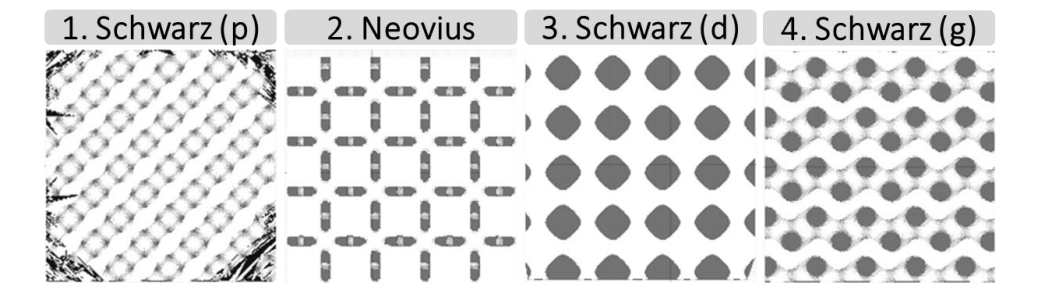


**Experimental Designs** 

Single-factor experiments were designed and conducted in this study to investigate the mechanical properties of four TPMS scaffold designs, as demonstrated in Figure 2 (and listed in Table 1 along with design, material, and extrusion process parameters), including: (i) Schwarz-Primitive, SW(p), (ii) Neovius, (iii) Schwarz Diamond, SW(d), and (iv) Schwarz Gyroid, SW(g).

Figure 2

Triply Periodic Minimal Surface of All Four TPMS designs (Schwarz-Primitive, Neovius, Schwarz-Diamond, and Schwarz-Gyroid)



*Note*. Used in this work for the fabrication and characterization of bone tissue scaffolds composed of PAPC-I, PAPC-II, and PAPC-V.

Ultimaker S5 (Utrecht, Netherlands) was the additive manufacturing platform of choice used in this study. As shown in Table 1, the fabrication process parameters were set at their optimal values based on the authors' prior characterization studies [57, 58, 60]. The manufacturing platform has a build volume of 330 mm × 240 mm × 300 mm, equipped with a brass microcapillary nozzle (having a diameter of 400 μm in this study). Furthermore, due to the brittle nature of PAPC-V (having a high Nylon-66 content), it was pre-heated prior to feeding. The PAPC-V material was pre-heated to a temperature of 80 °C for approximately 12 hours before material deposition as well as for the total duration of the 3D-printing process.

The slicing software used was Ultimaker Cura (Utrecht, Netherlands), which would convert the TPMS computer-aided design (CAD) models (imported as .stl file format) into a G-code to generate a toolpath for scaffold additive fabrication.

Table 1

The design, material, and extrusion process parameters

Parameter	Туре	Level [Unit]			
Variables					
Scaffold Design	Design	Schwarz-Primitive, SW(p)     Neovius     Schwarz-Diamond, SW(d)     Schwarz-Gyroid, SW(g)			
Medical Composite	Material	PAPC-II PAPC-V			
	Fixed Parar	neters			
Scaffold Porosity	Design	60 [%]			
Number of Shells	Design	1			
Scaffold Dimensions	Design	15×15×15 [mm]			
Layer Height (Thickness)	Design	200 [μm]			
Layer (Line) Width	Design	300 [µm]			
Infill Density	Design	100 [%]			
Nozzle Size	Machine	400 [μm]			
Bed Temperature	Machine	80 [°C] for PAPC-II			
Bed Temperature	Machine	95 [°C] for PAPC-I & V			
Print Speed	Machine	10 [mm/s]			
Deposition Head	Machine	215 [°C] for PAPC-II			
Temperature	iviaciiiiic	235 [°C] for PAPC-I & V			
Flow (Feed) Rate	Machine	120 [%]			
Build Plate Adhesion Type	Machine	Brim			

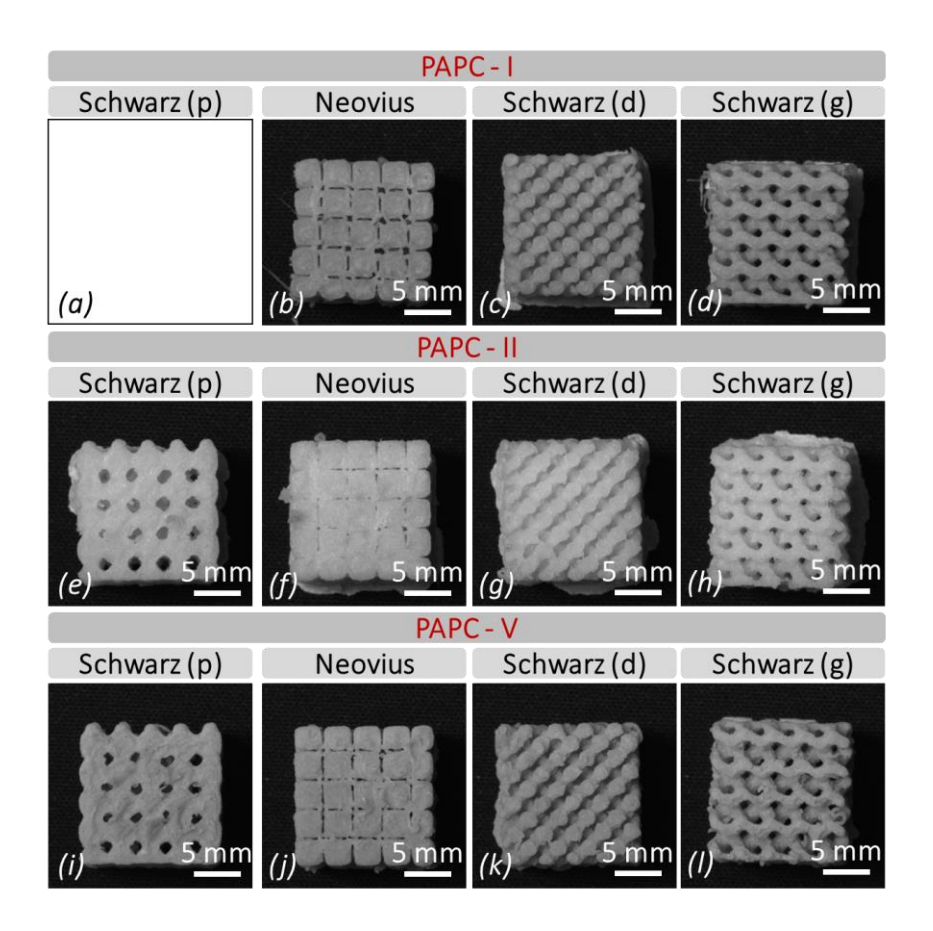
*Note.* Defined in this study to investigate the mechanical properties of four TPMS scaffold designs, each composed of three medical-grade composite materials, i.e., PAPC-I, PAPC-II, and PAPC-V.

We had initially observed that scaffolds with 60%-80% porosity would be suitable for cellular analysis [61]. Note that cell migration as well as the diffusion of nutrients within a scaffold are adversely affected if the pores are too small. Also, closed pores hinder not only material transport and cell proliferation, but also osteoconduction. In contrast, too large pores lead to a decline in the mechanical properties of a fabricated bone scaffold in addition to a decline in the surface area required for cell adhesion.

A precise balance (Mettler Toledo, Columbus, OH) was also used to measure the mass of the samples, along with using a digital caliper (Husky Tools, Home Depot, Atlanta, GA) to capture the dimensions of the fabricated scaffolds. In addition, a high-resolution (9.1 MP) charge-coupled device (CCD) camera (GS3-U3-91S6M-C, FLIR Systems, Inc., Richmond, BC, Canada) was used to capture the morphology and the microstructure of the fabricated bone tissue scaffold with monochromatic images as illustrated in Figure 3. The acquired images were saved in .tif file format.

Figure 3

Monochromatic images of the 3D-fabricated TPMS bone scaffolds



*Note*. The morphology and microstructure of each scaffold design. Note that the Schwarz (p) design was not successfully fabricated when PAPC-I was used (due to complexities associated with filament brittleness during material deposition) and thus was excluded from the figure.

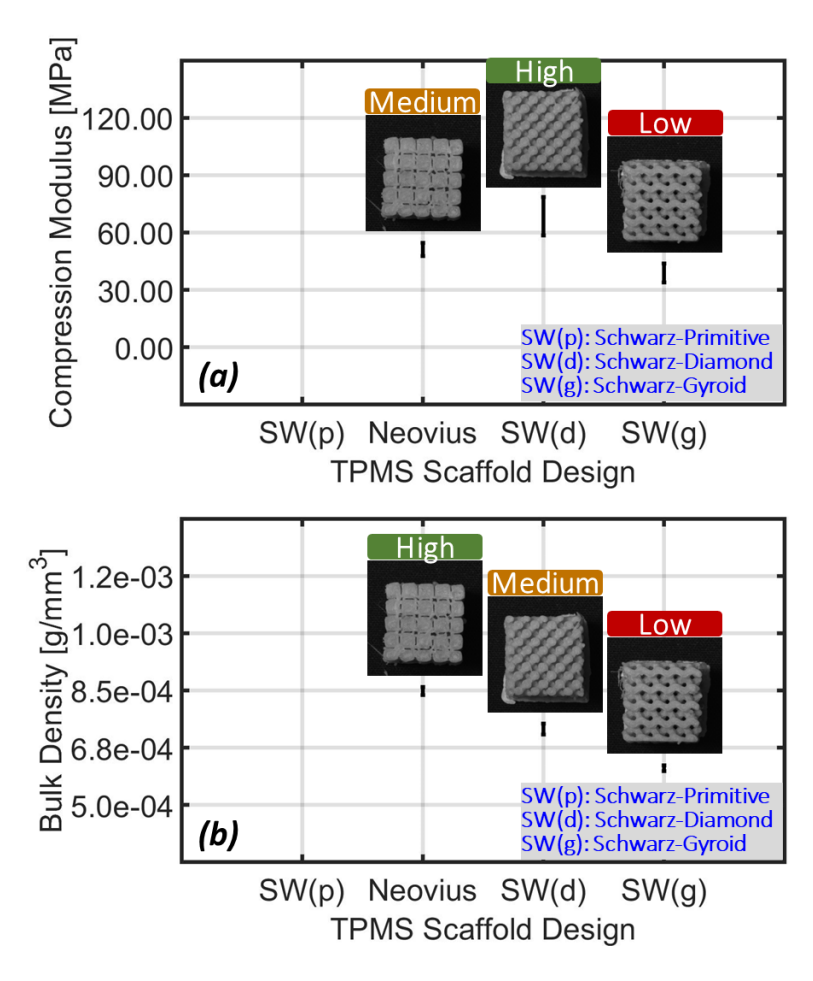
Finally, the compression modulus (stiffness) of the fabricated bone scaffolds was measured by using a compression testing system (MTI-10K, Measurements Technology Inc., Marietta, GA, USA). In addition, a MATLAB code was developed in-house to calculate the compression modulus of the fabricated scaffolds based on stress-strain plots.

#### **Results and Discussion**

Figure 4 demonstrates the compression modulus as well as the bulk density of the bone scaffolds composed of PAPC-I. It was observed that the Schwarz-Diamond design, SW(d), had the highest level of stiffness when compared to the other models, while the Neovius design had the highest level of bulk density. The Neovius design also appeared to have a medium level of stiffness. We were unable to fabricate the Schwarz-Primitive design, SW(p), composed of PAPC-I, due to complexities associated with filament brittleness during material deposition. In addition, poor "layer adhesion" was observed when fabricating SW(p). During the fabrication of SW(p) scaffolds, it was repeatedly observed that the loaded PAPC-I filaments were broken in the Bowden tube during material transport and deposition (with and without pre-heating). After further investigation, it was found that the use of an oven 3D-printer could be suitable for scaffold fabrication based on the PAPC-I composite material. In contrast, for PAPC-II and PAPC-V, the pre-heating process significantly helped achieve smooth material deposition (imparting flexible characteristics to both PAPC-II and PAPC-V).

Figure 4

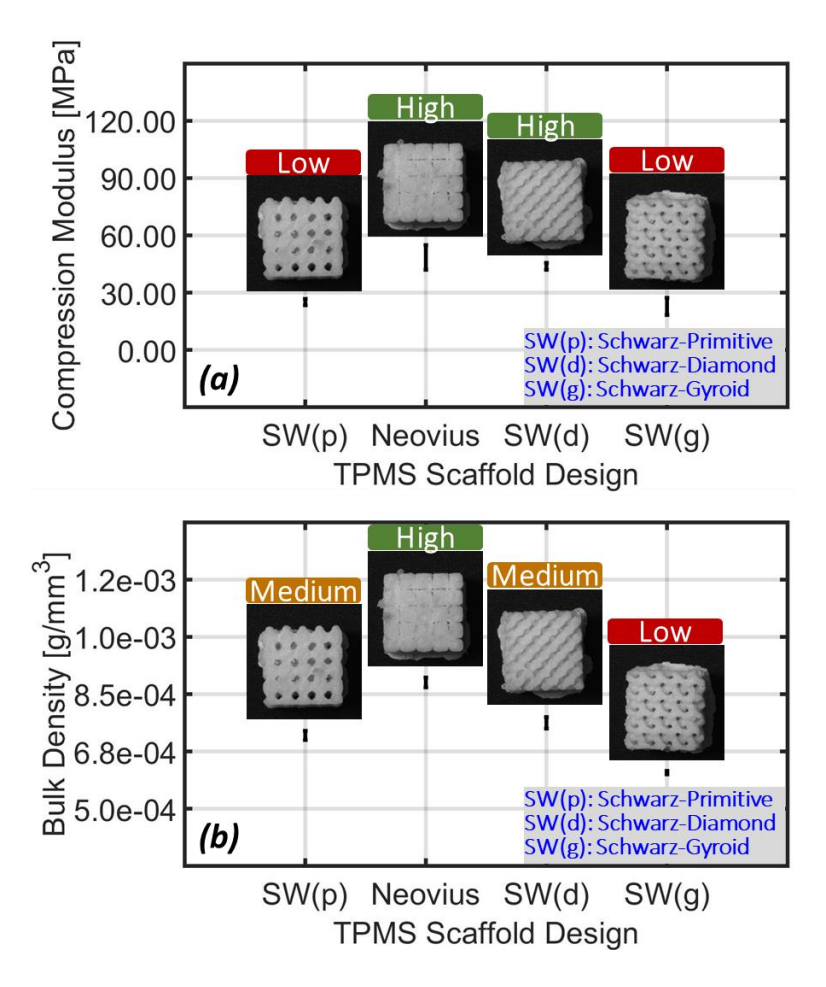
A comparison of the compression modulus (stiffness) as well as the bulk density of the FDM-fabricated TPMS bone scaffolds



*Note.* Composed of PAPC-I Each scaffold design was replicated five times (n=5).

Figure 5

A comparison of the compression modulus (stiffness) as well as the bulk density of the FDM-fabricated TPMS bone scaffolds

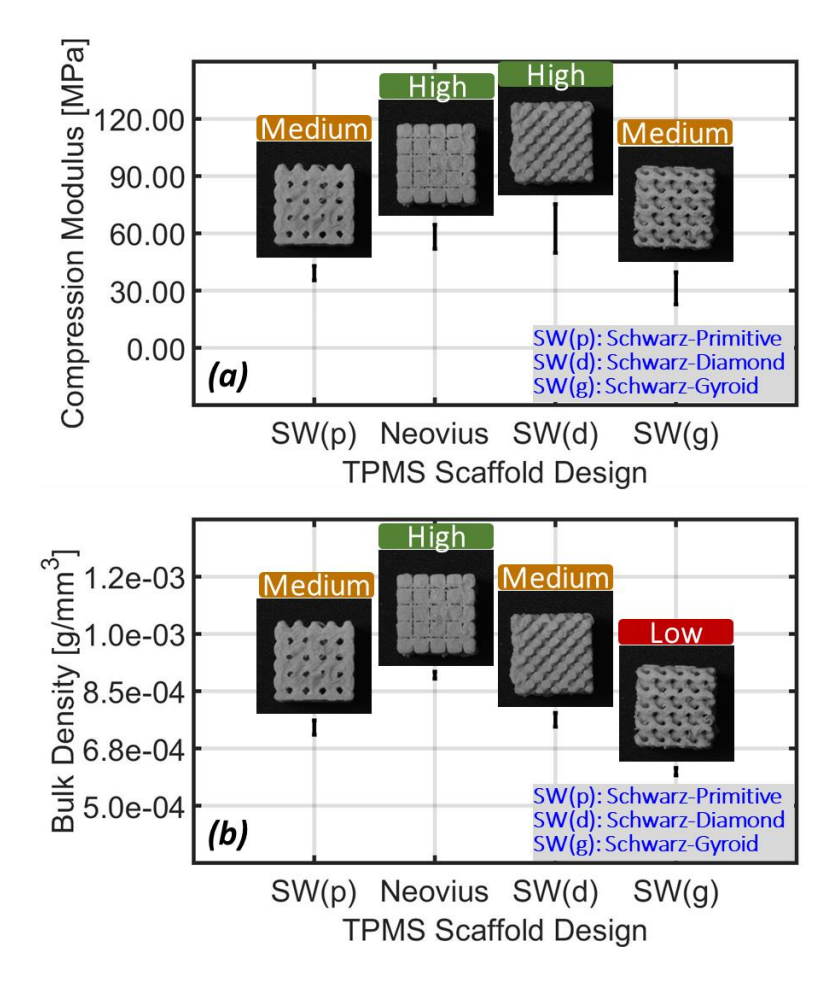


*Note.* Composed of PAPC-II. Each scaffold design was replicated five times (n=5).

Figure 5 illustrates the compression modulus and the bulk density of the bone scaffolds composed of PAPC-II. It was observed that the Neovius and Schwarz-Diamond designs had a high level of compression modulus. In contrast, the Schwarz-Primitive and Schwarz-Gyroid designs appeared to have a low level of stiffness. Similarly, the Neovius design had the highest level of bulk density. The Schwarz-Primitive and Diamond designs appeared to have a medium level of bulk density, while the Schwarz-Gyroid had the lowest density level.

Figure 6

A comparison of the compression modulus (stiffness) as well as the bulk density of the FDM-fabricated TPMS bone scaffolds



*Note.* Composed of PAPC-V Each scaffold design was replicated five times (n=5)

Figure 6 illustrates the compression modulus and the bulk density of the bone scaffolds composed of PAPC-V. It was observed that the Neovius and Schwarz-Diamond designs similarly had a high level of stiffness with Schwarz Diamond leaning to the higher end. The relatively high compression modulus of the Neovius design as well as the Schwarz-Diamond design, stems from their packed and regular internal microstructures, as implied from

Figure 3. Please note that the Neovius design inherently resembles a cubical unit cell, which has outward necks extended toward the middle of each edge [62, 63], as mathematically defined by Eq. (1).

$$3(\cos x + \cos y + \cos z) + 4(\cos x \cos y \cos z) = 0 \tag{1}$$

The internal structure of the Schwarz-Diamond design is based on two intertwined congruent labyrinths, similar to the diamond bond structure, which is not only inflated but also tubular, as mathematically expressed by Eq. (2) [63].

$$\sin x \sin y \sin z + \sin x \cos y \cos z + \cos x \sin y \cos z + \cos x \cos y \sin z = 0$$
 (2)

Relatively less packed, the Schwarz-Primitive and Schwarz-Gyroid designs appeared to have a medium level of stiffness. The Schwarz Primitive design is on the basis of two intertwined congruent labyrinths similar to an inflated tubular cubic lattice, as expressed mathematically by Eq. (3) [63]. Note that the Schwarz-Primitive design has relatively high *surface-to-volume ratio* [64] and therefore can be a potential, porous scaffold for bone tissue engineering. The Schwarz Gyroid design has three-fold rotational (not mirror) symmetry with no embedded straight lines, as mathematically given by Eq. (4) [62, 63].

$$\cos x + \cos z + \cos y = 0 \tag{3}$$

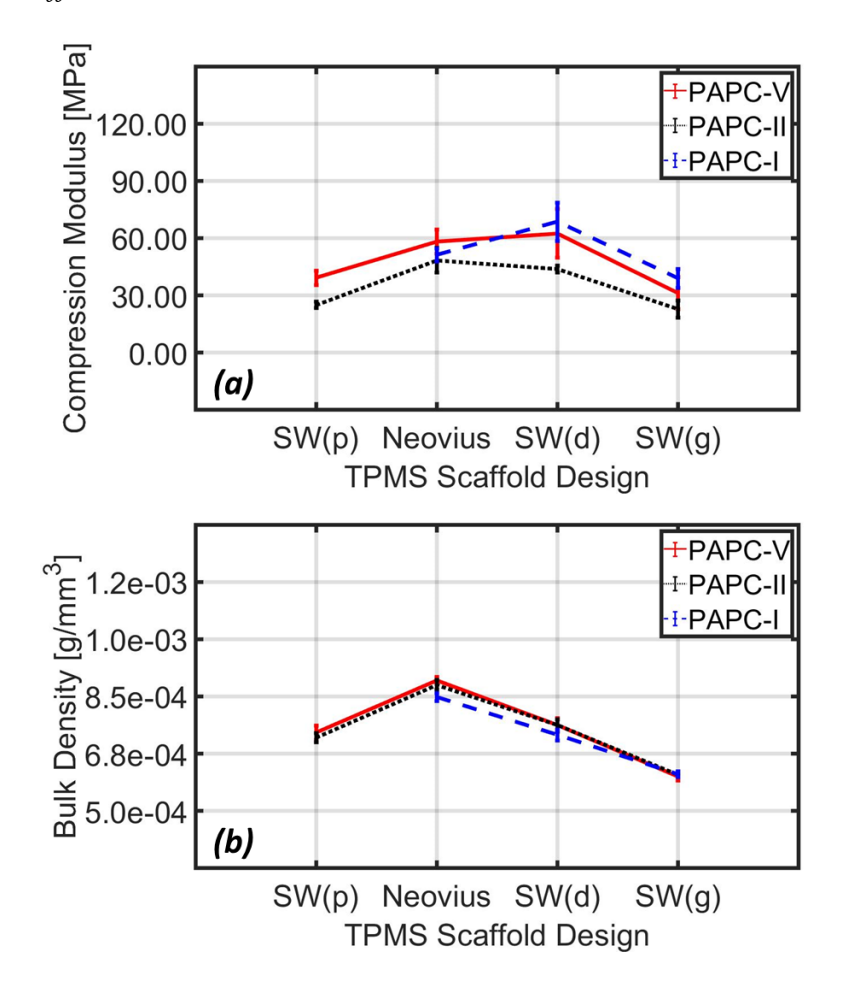
$$\cos x \sin y + \cos y \sin z + \cos z \sin x = 0 \tag{4}$$

Similar to PAPC-II, the Neovius design had the highest level of bulk density out of the test group. The Schwarz-Primitive and Diamond designs appeared to have a medium level of density, while the Schwarz-Gyroid had the lowest density level. It turned out that, with

consideration of all the four TPMS designs, while the compression modulus of PAPC-V is comparable to that of PAPC-I, its bulk density is close to that of PAPC-II.

Figure 7

An overall comparison of the compression modulus (stiffness) as well as the bulk density of all fabricated bone scaffolds



*Note*. Each design was replicated five times (n=5).

Overall, Figure 7 demonstrates a comparison of the compression modulus (stiffness) as well as the bulk density of PAPC-I, PAPC-II, and PAPC-V as a function of the four TPMS bone scaffold designs. It was observed that PAPC-V and PAPC-I had a relatable level of stiffness, while PAPC-II appeared to yield the lowest level of compression modulus. For the Schwarz-Primitive and Neovius designs, PAPC-V had a superior performance, while for the Schwarz-

Diamond and Gyroid, PAPC-I led to scaffolds with a higher level of stiffness. The bulk density of the PAPC-V-based scaffolds was comparable to that of PAPC-II-based scaffolds.

#### **Summary**

The objective of this research work was to investigate the mechanical properties of TPMS-based bone tissue scaffolds having complex microstructures, fabricated based on FDM additive manufacturing process, as a function of three medical-grade composite materials, i.e., PAPC-I, PAPC-II, and PAPC-V. Four TPMS designs (including Schwarz-Primitive, Neovius, Schwarz-Diamond, and Schwarz-Gyroid) were utilized in this study to assess the compression modulus as well as the bulk density of the three PAPC composite materials. It was observed that the Neovius and Schwarz-Diamond designs had a relatively high level of compression modulus in contrast to the Schwarz-Primitive and Schwarz-Gyroid designs. In addition, the Neovius design had the highest level of bulk density. PAPC-V and PAPC-I had a comparable level of compression modulus, while PAPC-II had the lowest level of stiffness. However, the bulk density of PAPC-V scaffolds was comparable to the bulk density of PAPC-II scaffolds.

# Chapter 3: Characterization of the Mechanical Properties of Bone-Like, Porous Tissue Scaffolds with Complex Microstructures Composed of a Medical-Grade Material for Bone Regeneration

# **Goal and Objectives**

Patient-specific treatment for bone pathology using porous osteoconductive scaffolds has faced clinical challenges due to the lack of mechanical strength and bioactivity. These properties are critical for osteogenesis, bone bridging, and bone regeneration to occur for the development of bone inside the patient. Thus, the need to formulate and characterize biocompatible and mechanically robust materials with low immunogenicity for bone regeneration would be inevitable.

The goal of this work is to investigate the mechanical performance of SimuBone material using tensile and torsion analysis. In addition, the SimuBone material used in developing the TPMS scaffold is biocompatible and biodegradable.

Moreover, the significance of our research is demonstrated in the analysis of the triply periodic minimal surface (TPMS) scaffold of 10 different designs, which is evaluated by mechanical compression analysis. Observing the effects of deposition mass and pore percentage on the scaffold performance is crucial. Importantly, our research utilizes the additive manufacturing (AM) process of fused deposition modeling (FDM) 3D printing, a practical and efficient method. With the fabrication of 200 TPMS scaffolds, each design has 20 replicates, further highlighting the robustness of the approach.

#### Material and Methods

The material and methods section will detail the development processes of creating the geometry of the TPMS scaffold within Rhion 7 using parametric equations. The torsion and

tensile bars were also based on machining standards. Furthermore, the fabrication method used for developing the models is fused deposition modeling (FDM) 3D printing, which all were developed with the same material similar to bone-like material to reflect simulated application capabilities.

#### **Experimental Designs**

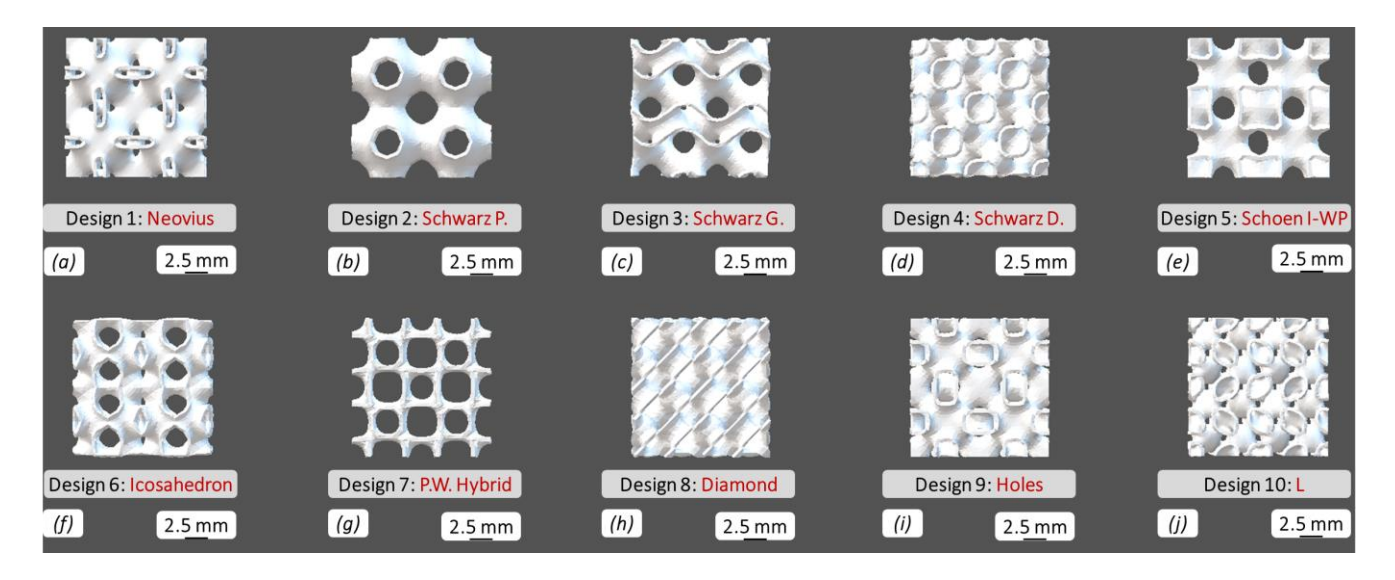
#### Scaffold Design

Triply periodic minimal surface (TPMS) scaffolds have a surface with minimal area and boundaries defined by closed curves. Each unit cell is given a thickness for its surface, which is then combined to formulate a cubically symmetric scaffold that will retain interconnected pores with periodic repetition [29].

Thus, this formulation yields a natural resemblance to the trabecular bone structure. In addition, the porous TPMS scaffolds are shown to have optimized bone regeneration for mechanical properties along with mimicking the biological bone tissue to aid in integrating bone tissue to promote cellular processes like oxygen diffusion, ion exchange, and nutrient transport [29].

Figure 8

TPMS designs of all 10 scaffolds



Furthermore, Figure 8 shows all 10 TPMS scaffold designs where (a) to (j) are design 1 Neovius to design 10 L. The scaffolds are 15 cubic mm. Notable features on scaffold designs of Neovius (a), Schwarz P. (b), Schoen I-WP (e), Icosahedron (f), P.W. Hybrid (g), and Holes (i) all show to have more simplistic curvature than their counterparts with more complex curvature of Schwarz G. (c), Schwarz D. (d), and Diamond (h). Additionally, design 10 L (j) shows a rich mixture of the 2 variants for (j) to have the deeply interconnected curvature and the sound structure of a more favorable cubic formulation.

# **Modeling Software**

The modeling software used to develop the TPMS parametric equations is Rhino 7 with the Grasshopper extension.

**Table 2** shows all 10 TPMS scaffold equations, with the design numbers arranged according to Figure 8 formatting. The Millipede and Weaverbird programs allow visualization of the 3D parametric equations as a solid model.

**Table 2**Parametric equations of TPMS design 1 - 10.

Equations	TPMS Design
$3(\cos(x) + \cos(y) + \cos(z)) + 4(\cos(x)\cos(y)\cos(x))$	(1)
$-(\cos(x) + \cos(y) + \cos(z))$	(2)
$\sin(x)\cos(y) + \sin(z)\cos(x) + \sin(y)\cos(z)$	(3)
$\cos(x)\cos(y)\cos(z) - \sin(x)\sin(y)\sin(z)$	(4)
$2(\cos(x)\cos(y) + \cos(y)\cos(z) + \cos(z)\cos(x)) - (\cos(2x) + \cos(2y) + \cos(2z)$	(5)
$\cos\left(x + \frac{1+\sqrt{5}}{2y}\right) + \cos\left(x - \frac{1+\sqrt{5}}{2y}\right) + \cos\left(y + \frac{1+\sqrt{5}}{2z}\right)$ $+\cos\left(y - \frac{1+\sqrt{5}}{2z}\right) + \cos\left(z + \frac{1+\sqrt{5}}{2x}\right) + \cos\left(z - \frac{1+\sqrt{5}}{2x}\right)$	(6)
$10(\cos(x)\cos(y)) + \cos(y)\cos(z) + \cos(z)\cos(x)$ $-0.01(\cos(x)\cos(y)\cos(z)$	(7)
$\sin(x)\sin(y)\sin(z) + \sin(x)\cos(y)\cos(z)$ $+\cos(x)\sin(y)\cos(z) + \cos(x)\cos(y)\sin(z)$	(8)
$\cos(x) + \cos(y) + \cos(z) + 4\cos(x)\cos(y)\cos(z)$	(9)
$\frac{1}{2}\sin(2x)\cos(y)\sin(z) + \sin(2y)\cos(z)\sin(x)$ $+\sin(2z)\cos(x)\sin(y) - \frac{1}{2}\cos(2x)\cos(2y)$ $+\cos(2y)\cos(2z) + \cos(2z)\cos(2x)$	

Thus, Table 3 shows the parameters used for all 10 TPMS scaffolds within Rhino 7. The parameters column section yields prominent features within the Grasshopper, Millipede, and Weaverbird programs. The model dimensions of the TPMS scaffold are uniform lengths of 6-by-6 cubic mm. Furthermore, the step iteration for models (b) through (i) is 7.710; for the step iteration for models (a) and (j) is 18.710; this was done to aid in improving the scaffold topology to allow for enhanced additive manufacturing (AM) process. Merged Toggle is a collection of Boolean functions of (True/False) values. These values for the development of the scaffold were

set to True. As for the IsoValue, it is a collection of double-precision floating-point values of -0.269. The ArrBox count function is to construct multiple units and attach them within a cubic formulation as a solid single structure. This value was set to 2 with a total of 4-unit cells being conformed into a solid structure, as shown in **Figure 8** The level parameters are set to 1 for this parameter, which affects the number of subdivision iterations for each face on the scaffold. In addition, the WBThickness affects the wall thickness, allowing this function to alter the porosity of the scaffolds. Thus, the value was set to 0.15 mm for all 10 TPMS scaffold designs.

**Table 3**Rhino 7 parameters for all 10 TPMS scaffolds.

Parameters	Values
Model Dimensions (mm <sup>3</sup> )	6
Step	7.710
step For Model (a) and (j)	18.710
Merged toggle	TRUE
IsoValue	-0.269
ArrBox (x,y,z) Count	2
Level	1
WBThickness Distance (mm)	0.15

Table 4 covers the parameters of the torsion and tensile bars. This will give insight into the model type and dimensions used within the analysis.

**Table 4**Parameters for torsion bar and tensile bar.

Parameters	<b>Torsion Bar</b>	Tensile Bar
Туре	SM 1001	ASTM [D638 – 14] Type IV
Width narrow section (mm)	6	6
Length narrow section (mm)	76.2	33
Width Overall (mm)	-	19
Length Overall (mm)	143	115
Gage Length (mm)	-	25
Distance Between Grips (mm)	-	65
Radius of Fillets (mm)	-	14
Outer Radius (mm)	-	25
Outer Area (mm <sup>2</sup> )	12	-

# Torsion Bar

The torsion bar type being used is the SM 1001 standard model. The narrow width section yields a 6 mm diameter and is 76.2 mm long. The overall length of the torsion bar is 143 mm, with an area of 11 for the outer sections. Table 4 covers the parameters of the torsion and tensile bars. This will give insight into the model type and dimensions used within the analysis.

## Tensile Bar

The tensile bar type is the ATSM [D638-14] type IV. This model's narrow width is 6 mm, and its narrow length is 33 mm. Additionally, the overall width is 19 mm, and the overall

length is 115 mm. The gage length is 25 mm, and the distance between the grips is 65 mm. The radius on the fillets is 14 mm, and the outer radius is 25 mm.

#### Compression TPMS Scaffolds

The compression analysis will be performed by the TPMS scaffold. Table 5 details the dimensions of the scaffold's geometry. The scaffold dimensions are 15 by 15 cubic mm. In addition, the compression machine being used has a compressive load of 5 kN.

#### Materials

The material selected for the fabrication of the TPMS bone scaffold is SimuBone. SimuBone properties are used for the development of bone-like structures. SimuBone can simulate both cortical and cancellous bone, which makes it a viable alternative to a realistic cadaver bone specimen. Thus, patient-specific pre-surgical assessment simulation and training are prominent materials for investigating bone scaffold applications.

In addition, SimuBone is ISO-certified for eliminating bacteria for the life of printed parts, which will help protect the bone scaffold. SimuBone also uses an additive mixture of PLA filament, thus allowing the fabrication of the bone scaffold to be easily printed.

#### **3D-Microfabrication Process**

#### Fused Deposition Modeling Process

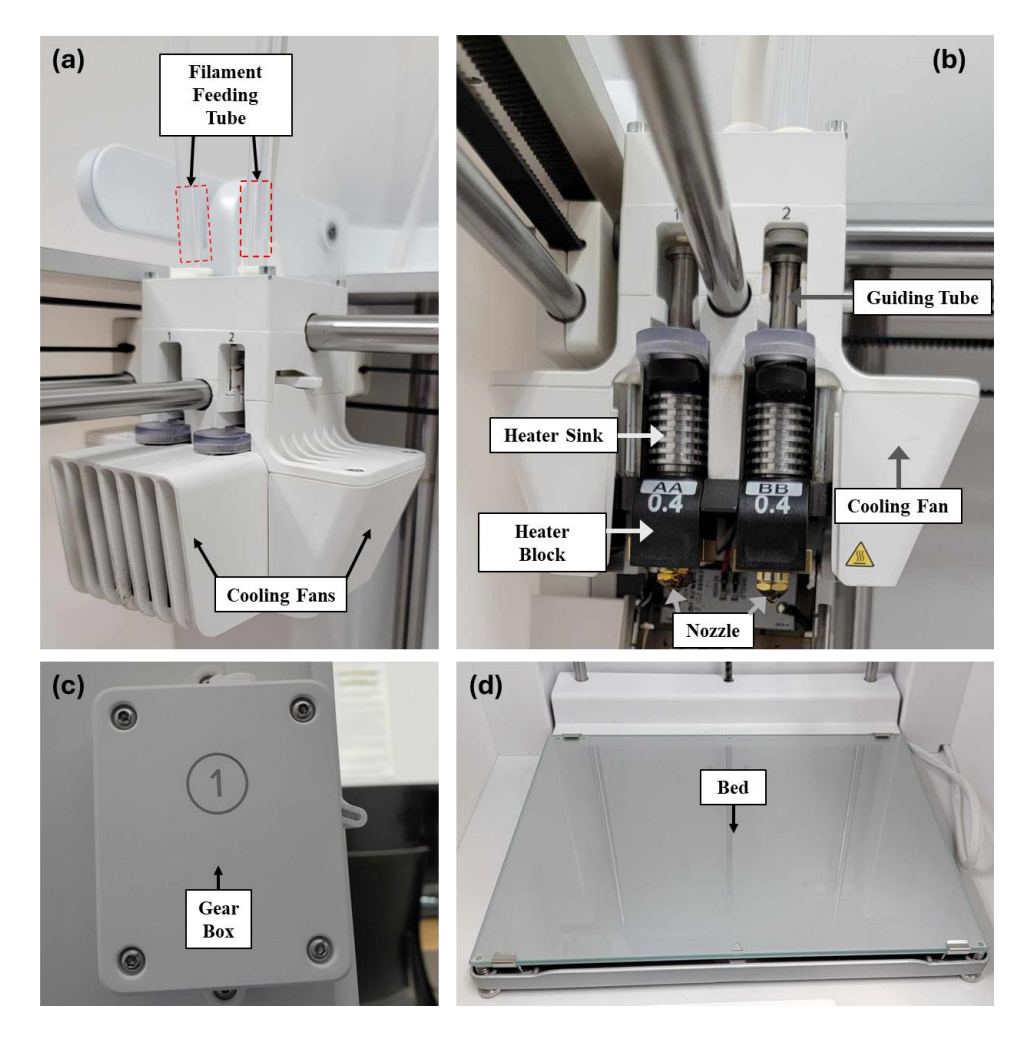
The FDM process is the method used to develop the TPMS bone scaffold. Thus, Figure 9 represents a diagram of the material transport and deposition of the AM process. The SimuBone filament material with a diameter of 2.85 mm is fed within the head of the extruder, where the stepper motors will lead the filament with the bowed tube, which will guide the SimuBone filament into the heating block of the FDM printer. From there, the filament will be heated up, resulting in the filament becoming moldable. The heating block controls the filament's viscosity

and the material's rheological properties. In addition, the filament will act on the characteristics of a non-Newtonian fluid flow, where the material will be extruded out of the micronozzle of the printer head. Thus, the polymer will be deposited onto the heated bed of the build plate. The heat between the nozzle and the bed plate differs, producing a temperature cooling and the molten polymer adhering to the bed plate. This process will be repeated in an iterative process using G-code to construct the TPMS scaffolds, where layer-by-layer of the molten polymer will bind to the previous polymer, allowing them to form a robust structural bond.

Figure 9

A Schematic Diagram of Material Transport and Deposition in Fused Deposition Modeling

(FDM) Additive Manufacturing Process



#### Cura Settings

The Cura setting can be denoted within Table 5 for all 10 TPMS designs, torsion bar, and tensile bar, where the parameters of the FDM printing process and values are listed below. The scaffold pore percentage was calculated within equation (1) by fabricating a solid cube made for the SimuBone material. In addition, finding the difference between the solid cube and the TPMS scaffold and then dividing the solid cube results in the missing volume with the TPMS scaffold, thus providing the scaffold's pore percentage.

Pore Percentage = 
$$\left(\frac{Solid\ Cube-Scaffold}{Solid\ Cube}\right) * 100\%$$
 (1)

The scaffold dimensions within Cura were scaled up to produce a 15 mm cubic scaffold. The layer height used for the FDM printing is 200  $\mu$ m with a layer width of 300  $\mu$ m. In addition, the scaffolds and test bars' infill density are 100%. The nozzle diameter used is 400  $\mu$ m; the bed temperature is 60 °C with a deposition head temperature of 240 °C. The printing speed of the FDM process is 10 mm/s with a flow rate of 120%. Furthermore, the build plate adhesion type for all TPMS scaffolds and testing bars is a brim.

Table 5

Cura Setting with The Fabrication Parameters of The TPMS Scaffold for All 10 Designs, Torsion

Bar, And Tensile Bar.

Parameter	Type	Level [Unit]
Medical Composite	Material	SimuBone
Scaffold Dimensions	Design	15x15x15 [mm]
Layer Height (Thickness)	Design	200 [μm]
Layer (Line) Width	Design	300 [µm]
Infill Density	Design	100 [%]
Nozzle Size	Machine	400 [μm]
Bed Temperature	Machine	60 [°C]
Print Speed	Machine	10 [mm/s]
Deposition Head Temperature	Machine	240 [°C]

Flow (Feed) Rate	Machine	120 [%]
Build Plate Adhesion Type	Machine	Brim

Thus, the quantity produced for the Cura FDM process resulted in 200 TPMS scaffolds, with a set of 20 for each different design. As the torsion bar has a total of 5 replicas were produced. The tensile bars were replicated 15 times, with each set of 5 replicas at different degrees of angles at 0, 45, and 90, which will provide insight into the optimal fabrication conditions.

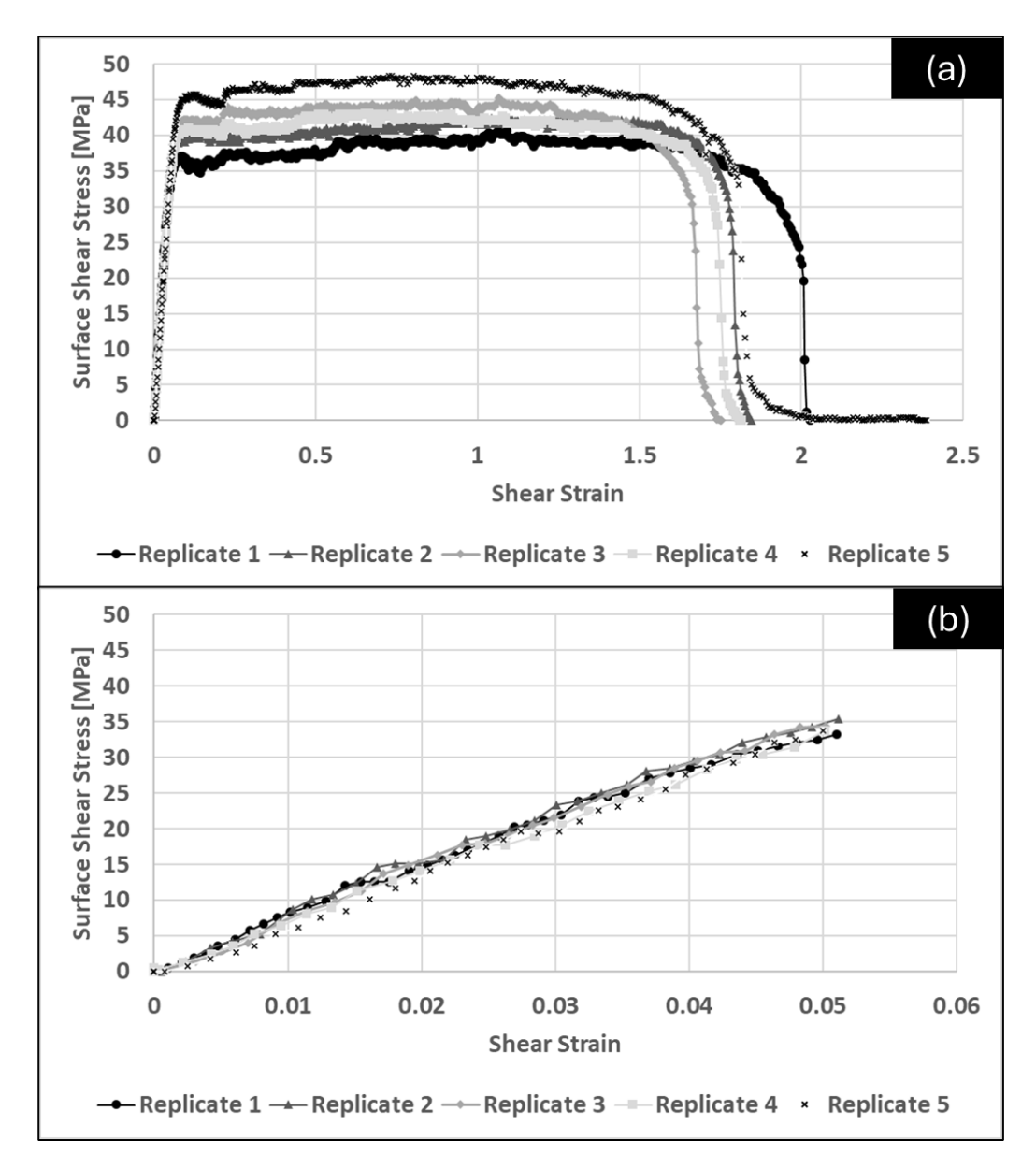
#### **Results and Discussion**

The results and discussion section will encompass the torsion, tensile, and compression analysis findings, as well as a discussion of the optimal performance of the TPMS scaffold designs.

# **Torsion Analysis**

Torsion analysis details the material's mechanical properties under the stress of angular displacement. Therefore, Figure 10 shows the total surface shear stress over shear strain. The material of Simubone can be seen to have a shear modulus of rigidity of  $714.79 \pm 11.97$  MPa. This value was calculated with the aid of Matlab over the course of 5 replications to determine the Youngs modulus of the process. Furthermore, the Ultimate yield strength average of all 5 replications is 44 MPa, along with the fracture region being noted at around 1.75, with the necking accruing at 1.5 on the shear strain axis. Additionally, Figure 10 depicts the consistency of all 5 replications, adding in validation that the Torsion models are repeatable.

Figure 10
Torsion SimuBone Elastic Curve Regions



*Note.* (A) depicts the full curved segment region, and (B) yields the elastic region section.

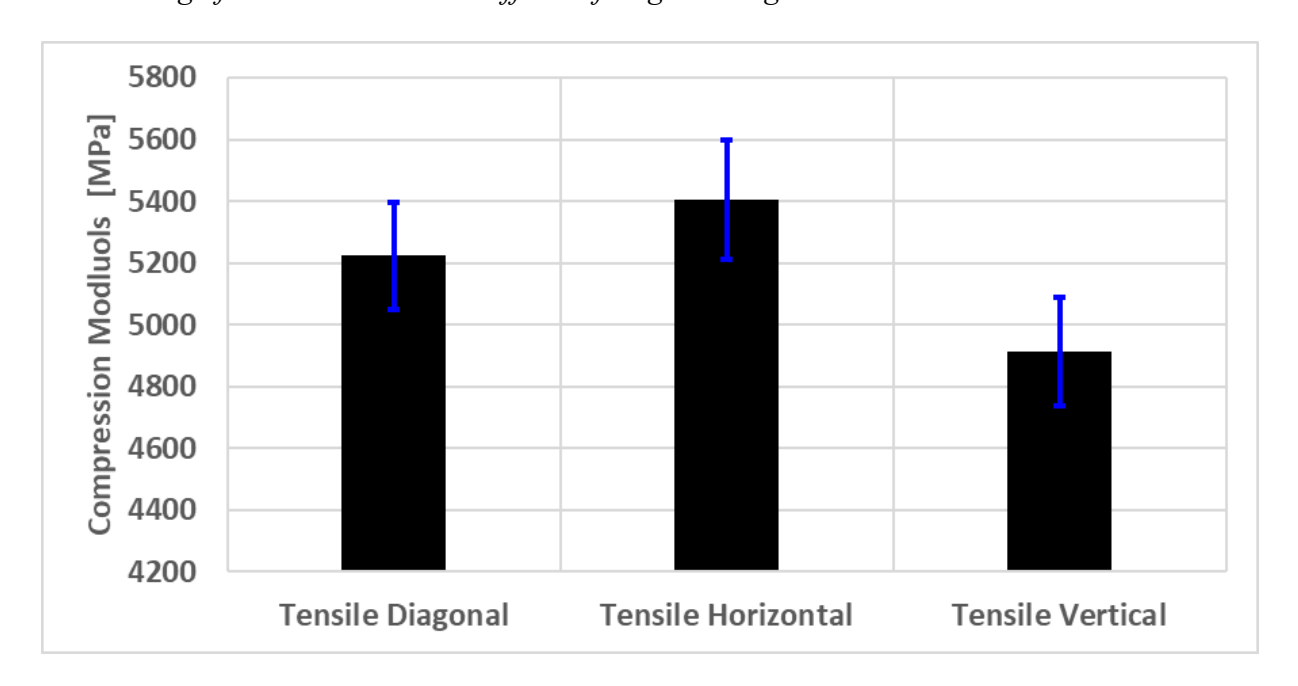
## Tensile Analysis

Tensile analysis details the mechanical strength of material while being placed under a pulling load. Thus, Figure 11 details the tensile strength of SimuBone under the effect of angel changes. The vertical tensile specimen yielded a compression modulus of an average of 4911.84

 $\pm$  175.18 MPa. The horizontal and diagonal average compression modulus are 5404.20  $\pm$  192.30 MPa and 5224.42  $\pm$  173.77 MPa, respectively. Therefore, the preferred direction of FDM printing is horizontal orientation. This orientation has been used in the development of the torsion bars. Simubone has been shown to have significant tensile strength, with only a standard deviation of 249.15 MPa in a sample size of 5 replications for each type. Thus, making it a quality material for use in bone tissue engineering.

Figure 11

Tensile Finding of SimuBone and The Effects of Angle Changes.



# Scaffold Compression Analysis and Optimal TPMS Scaffold Design

The scaffold compression analysis will detail the effect of compression strength and the relationship between pore percentage and the deposition mass of the TPMS scaffolds.

Figure 12

Visual comparison of the compression properties of the fabricated TPMS bone tissue scaffolds.

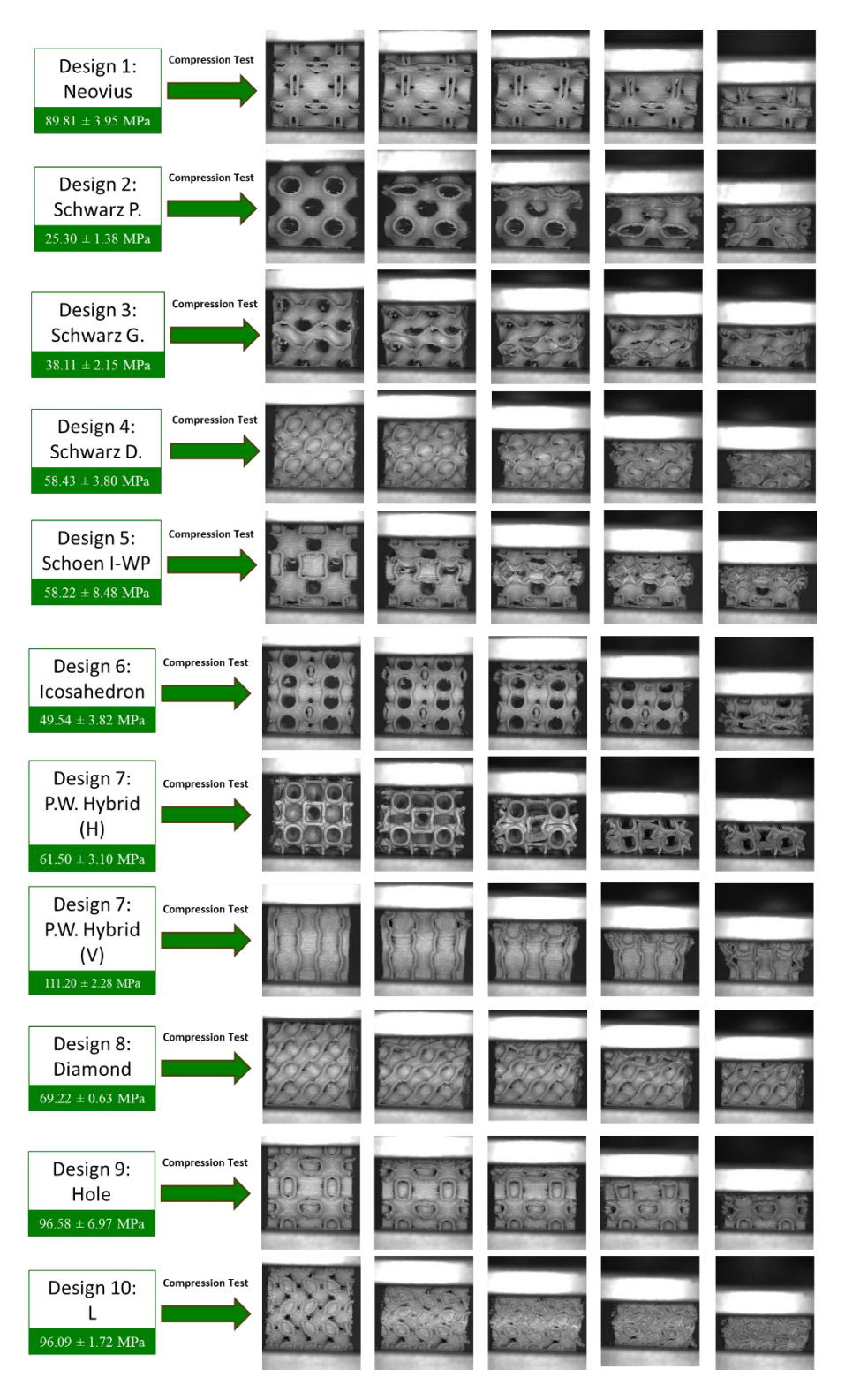


Figure 12 shows the compression performance of all 10 TPMS scaffolds. In addition, Figure 12 gives insight into failure point locations within the scaffold architecture. Thus, TPMS designs similar to Neovius, Schwarz P, Schoen I-WP, Icosahedron, P.W. Hybrid, and Holes all show a common trend of fracture points within the void locations of the TPMS scaffold. Neovius can be noted for having an architectural failure within the hollow regions in the scaffold where the structure would collapse on itself, leading to the need for a more robust wall thickness layer to improve the Neovius structure. Furthermore, it can be seen that the supports under the structure allowed for the structural resistance of the compression load. Only the hollow voids with the structure collapse underneath it, thus signifying the need for improved wall thickness around those regions. This common trend can be seen within TPMS scaffold with simple curvature and more cubic formulated architecture.

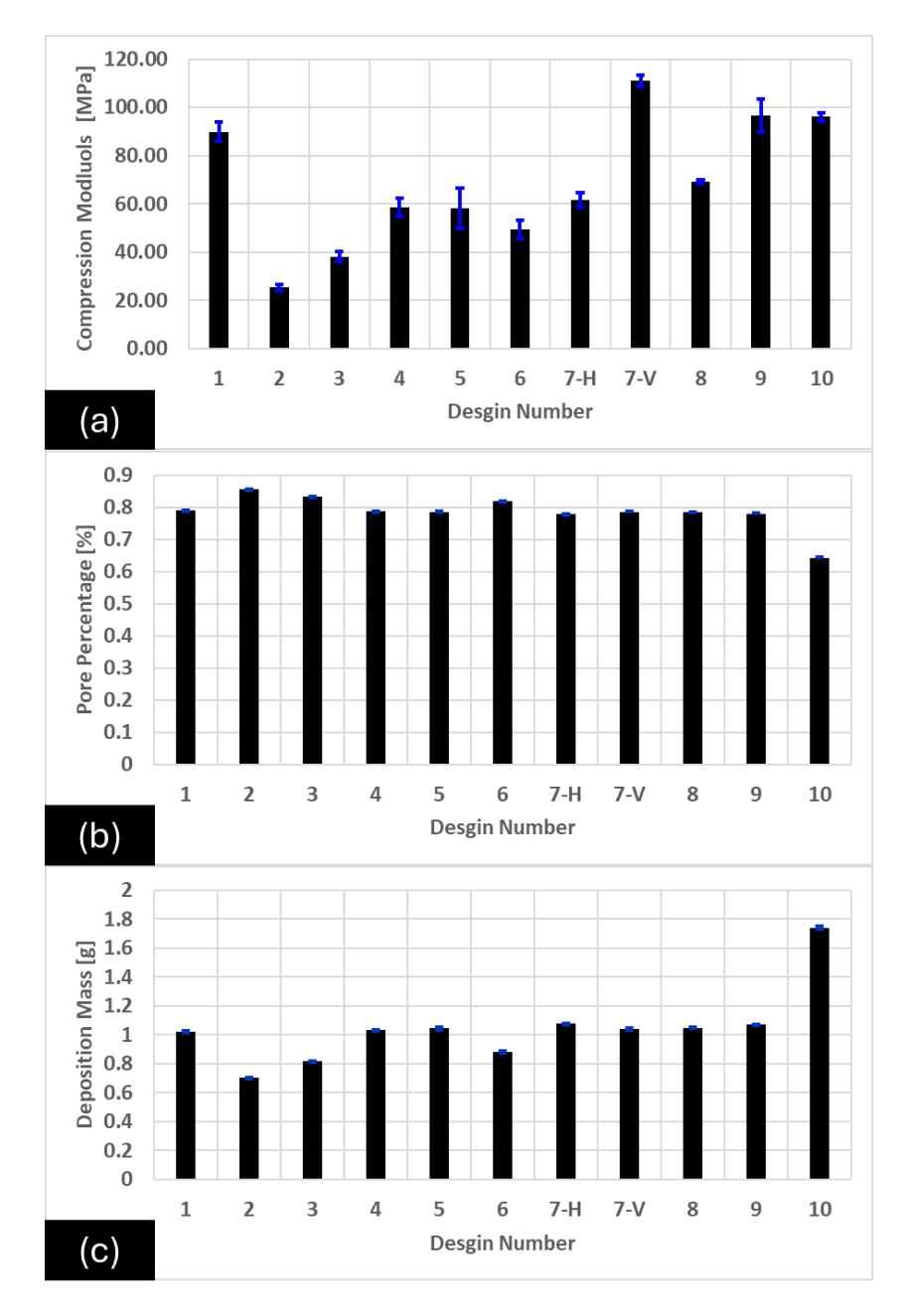
As for the TPMS scaffold, like that of Schwarz G, Schwarz D, Diamond, and L, with more enriched curvature and pore opening, yields a consistent trend within the failure locations of the scaffold architecture. Much like the cubic formulation shown in detail, the void with the scaffold is the weak point of all TPMS architecture. It can be further evaluated with designs like that of Schwarz G, yielding multiple pores regions with the structure, resulting in a uniform constructive failure to accrue. This is because all channels within the architecture do not have a solid support structure to aid against compressive loads. To improve the TPMS scaffold's compression performance, an increase in wall thickness and a decrease in pores opening will yield an improved robust compression score.

Furthermore, Figure 13 (a) details the compression modulus of all 10 TPMS designs. The weakest TPMS scaffold design is Schwarz P., with a  $25.30 \pm 1.38$  MPa compression modulus. Additionally, Schwarz G. and Schwarz D. have a compression value of  $38.11 \pm 2.15$  MPa and

 $58.43 \pm 3.80$ . It can be noted that the Schwarz D. compression modulus performs the most optimally out of the Schwarz family. For its compression modulus, it came in 7th in strength out of the 11 different variation types. The top 5 TPMS scaffold designs for compression modulus are P.W. Hybrid, Holes, L, Neovius, and Diamond, with the compression values being  $111.20 \pm 2.28$  MPa,  $96.58 \pm 6.97$  MPa,  $96.09 \pm 1.72$  MPa,  $89.81 \pm 3.95$  MPa, and  $69.22 \pm 0.63$  MPa respectively.

Figure 13

Evaluation of Compression modulus, Pore Percentage, and Deposition mass of all 10 TPMS scaffolds



*Note*. Design 7-h is the horizontal compression, and 7-v is the vertical compression. (a) shows the compression modulus of the TPMS scaffolds, (b) yields the pore percentage of the scaffold design, and (c) shows the deposition of mass per scaffold.

Furthermore, the TPMS design P.W. Hybrid was compressed vertically and horizontally due to the model not being identical based on its topology when rotated to different views of its sides. It was shown that the compression modulus of the vertical direction is far superior to that of the horizontal placement. This is due to the vertical version analysis showing that the structure will collapse on top of its supportive regions. Additionally, the horizontal version shows a more constructive collapse and consistent failure area where its pore size is significant. These gaps between the P.W. Hybrid design show that yield weak points are placed at the scaffold pore diameter regions.

Figure 13 (b) and (c) show the pore percentage of the scaffolds along with the deposition of the mass of the scaffolds. A common trend that can be discerned for the 2 figures is that when the pore percentage increases, an inverse relationship accrues with the deposition mass of the scaffolds. In addition, the TPMS scaffold Schwarz P. has the highest pore percentage; in return, it also has the lowest mass. The scaffold also shows the lowest compression modulus. As for the TPMS scaffold design, L is shown to have the lowest pore percentage along with the highest mass of all 10 TPMS designs. However, the compression modulus of the TPMS scaffold falls 3rd best in compression performance. Therefore, the increase in mass of the scaffold does not guarantee optimal performance of the scaffold design compression performance. Designs 7 show a pore percentage and a deposition of the mass of  $78.5\% \pm 0.10\%$  and  $1.041 \pm 0.004$  g, respectively. Along with performing the best compression modulus, the TPMS topology structure dictates compression performance more than mass quantity.

Therefore, the optimal performing TPMS bone scaffold with this analysis is the vertical version of P.W. Hybrid. Its pore percentage is acceptable for biological fluid and can withstand

compression stress within the human body. The reported range of human trabecular bone's yield strength is 0.56-64 MPa, respectively [34].

#### **Summary**

To reiterate, the torsion analysis of Simubone reveals its suitability for bone tissue engineering. With a shear modulus of rigidity of  $714.79 \pm 11.97$  MPa and an Ultimate yield strength average of 44 MPa, it is a highly rigid material. Its significant tensile strength, with a horizontal average compression modulus of  $5404.20 \pm 192.30$  MPa, further supports its use in FDM printing in the horizontal orientation. This makes Simubone a quality material for bone tissue engineering applications.

Furthermore, the optimal performance concluded with the compression analysis is the vertical version of P.W. Hybrid. Its pore percentage is acceptable for biological fluid, and in addition, it can surpass the yield strength of human trabecular bone.

# Chapter 4: Investigation of Material Transport through Triply Periodic Minimal Surface (TPMS) Bone Scaffolds Using Computational Fluid Dynamics (CFD) Goal and Objectives

Bone tissue engineering is an emerging field of regenerative medicine, using the principles of tissue engineering, stem cell biology, and biomedical engineering to fabricate functional tissue implants that can be inserted within a patient to repair or replace damaged/missing bone.

The motivation for this study is to observe the fluid flow dynamics within a porous scaffold, which will aid in understanding complex geometry structures with fluid interaction.

Fluid transport is crucial in material interaction and cell proliferation to develop bone scaffolds. The characteristics of permeability help in bone growth, but the induction of fluid flow wall shear stress (WSS) characteristics affects the biological development of the scaffold. For WSS, the fluid flow can hinder or improve cell growth. A high WSS can eliminate cellar development and vice versa for a lower WSS. Thus, the objective of this study is to use computational fluid dynamics (CFD) to analyze fluid flow through the scaffolds' internal/external geometry structure. A wide range of properties, such as pressure, velocity streamlines, and WSS, will be evaluated within this study. The aim is to explore how a fluid flow will pass through and over the pores of a scaffold and how it will interact with the geometry of the scaffold. This will give insight into how biological fluids interact within scaffold pores and microstructures, allowing for more efficient design and additive fabrication of scaffolds.

#### **Material and Methods**

The material and methods section will detail what development method was used for producing the CFD TPMS Scaffold Design, along with meshing, applied governing equation, fluid properties, and boundary conditions used within the simulation. In addition, the numerical solution will discuss the scheme and method used within the ANSYS simulation.

# **Scaffold Design**

A total of 10 TPMS scaffolds were designed using Rhion 7 with the Grasshopper extension. The designs can be seen in Figure 14, and the equation can be denoted by Table 6. The Millipede and Weaverbird programs were used to develop an algorithm to construct the TPMS design. Millipede and Weaverbird programs can visualize parametric equations into 3D rendering in a mesh structure.

Figure 14

TPMS designs (in order of Design 1-10) developed in this study for fabrication of bone scaffolds having complex, porous internal microstructures.

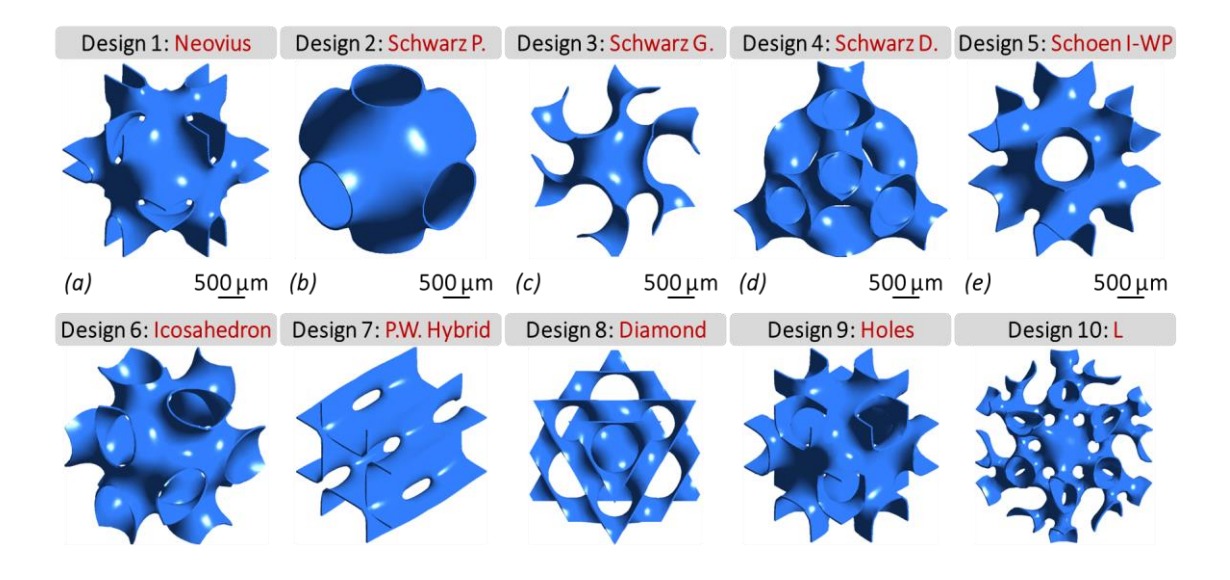


**Table 6**Parametric Equations of TPMS Design 1 - 10.

Equations	TPMS Design
$3(\cos(x) + \cos(y) + \cos(z)) + 4(\cos(x)\cos(y)\cos(x))$	(1)
$-(\cos(x) + \cos(y) + \cos(z))$	(2)
$\sin(x)\cos(y) + \sin(z)\cos(x) + \sin(y)\cos(z)$	(3)
$\cos(x)\cos(y)\cos(z) - \sin(x)\sin(y)\sin(z)$	(4)
$2(\cos(x)\cos(y) + \cos(y)\cos(z) + \cos(z)\cos(x)) - (\cos(2x) + \cos(2y) + \cos(2z))$ $+ \cos(2z)$	(5)
$\cos\left(x + \frac{1+\sqrt{5}}{2y}\right) + \cos\left(x - \frac{1+\sqrt{5}}{2y}\right) + \cos\left(y + \frac{1+\sqrt{5}}{2z}\right)$ $+\cos\left(y - \frac{1+\sqrt{5}}{2z}\right) + \cos\left(z + \frac{1+\sqrt{5}}{2x}\right) + \cos\left(z - \frac{1+\sqrt{5}}{2x}\right)$	(6)
$10(\cos(x)\cos(y)) + \cos(y)\cos(z) + \cos(z)\cos(x)$ $-0.01(\cos(x)\cos(y)\cos(z)$	(7)
$\sin(x)\sin(y)\sin(z) + \sin(x)\cos(y)\cos(z)$ $+\cos(x)\sin(y)\cos(z) + \cos(x)\cos(y)\sin(z)$	(8)
$\cos(x) + \cos(y) + \cos(z) + 4\cos(x)\cos(y)\cos(z)$	(9)
$\frac{1}{2}\sin(2x)\cos(y)\sin(z) + \sin(2y)\cos(z)\sin(x)$	
$+\sin(2z)\cos(x)\sin(y) - \frac{1}{2}\cos(2x)\cos(2y)$	(10)
$+\cos(2y)\cos(2z) + \cos(2z)\cos(2x)$	

The parameters for these designs can be denoted in Table 7. All designs have the dimensions of a cube with a width, length, and height of 3 mm, respectively. The Step parameter is the iteration for the model generation. The Merged Toggle represents a collection of Boolean (True/False) values, and IsoValue represents a collection of double-precision floating point values. The ArrBox (x, y, z) Count supports constructing multiple units and attaching them into a cube to form a single structure. In addition, the level parameters control the number of subdivision iterations for each face on the designed model. The WBThickness controls the wall thickness of the model structure. In addition, design models 5, 9, and 10 have their step blocks changed to 16 to improve the simulation accuracy. The dimensions of the TPMS scaffold for the cubic 2-cell unit model are 6 mm cubic. In addition, the step size of the model is 11.710, with only dimensions 6 set to 18.710 for improved model accuracy. Furthermore, the ArrBox (x, y, z) Count is set to 2, allowing the cell units to merge and stack to formulate a single TPMS structure.

 Table 7

 TPMS design parameters within Rhino 7

Parameter	Values
Model Dimensions [internal/external]	3x3x3 mm
Model Dimensions [Cubic]	6x6x6 mm
Step	18.710
Merged Toggle	True
IsoValue	-0.269
ArrBox(x, y, z) Count	1
Level	3
WBThickness Distance	0.042 mm

*Note*. Designs 5, 9, and 10 have a step value of 16.000. For the cubic TPMS scaffold, set the ArrBox (x, y, z) to 2. Along with the cubic designs being set to 18.710 for improved accuracy.

After rendering the TPMS design, they are exported into a file form of .3dm (Rhino 7 3D Models files) respectively. The design will be imported within Fluid Flow (Fluent with Fluent Meshing) ANSYS 2023 R2. Once the design is entirely imported, the conversion from facets to a solid will be done by the built-in function from SpaceClaim ANSYS. An encloser box is then built around the design geometry, placing it within the center of the encloser box.

#### Meshing

The 3D geometry is defined as watertight for fluid flow in the internal and all external flow analysis. Furthermore, these parameters can be denoted in Table 8. For internal flow, the model's geometry wall distance is set to 0.2 mm uniformly from the inlet outlet and wall. As for the external flow geometry wall distance, the inlet and wall are set to 2 mm, and the outlet distance is 5 mm away for the model. A distance of 5 mm is used to capture any development wake regions within the analysis. The local surface meshing sizes for both internal and external are 0.01, 0.001, and 0.0001 m, respectively, to the inlet, outlet, wall, domain, and scaffold model. In addition, for the surface and volume mesh, the growth is set to 1.2 with a minimum surface size of 1.00E-05 m and a maximum surface size of 0.01 m.

Polyhedral was the meshing portion used to fill the cell volume elements. Furthermore, the solution residual sensitivity of the analysis is set at a convergence of 1.0E-06. In addition, the Fill Type used for volume meshing is Uniform and Smoothing Transition. For the internal flow analysis, designs 1, 9, and 10 used Smoothing Transition, with the rest using Uniform. As for the external flow analysis, only Design 1 used Smoothing Transition, and the rest used Uniform. Designs 9 and 10 did not need the Smoothing Transition because of the enlarged enclosure box

around the design geometry. Furthermore, the Uniform's function is that each layer's thickness remains the same throughout the volume mesh.

Along with the direction vector at each node, it maintains uniformity. In addition, it can easily be maintained for flat or lightly curved surfaces [65]. As for the Smoothing Transition boundary layer, mesh thickness and first layer height vary along the surface depending on the local surface mesh size, resulting in a smooth transition on the model.

Table 8

Number of Elements in Each CFD Design Model.

External Cubic Cell Volume Elements	External Cell Volume Elements	Internal Cell Volume Elements	Design Models
v oranic Elements	V Oranic Elements	V oranic Elements	
1666191	277566	257064	(1)
596974	110624	102928	(2)
878019	164854	151406	(3)
863602	168451	154217	(4)
785368	183322	165557	(5)
1252607	205754	190276	(6)
1392475	204218	189620	(7)
1072130	199373	186856	(8)
922325	305409	285650	(9)
4051629	462513	446121	(10)

*Note.* The minimum orthogonal quality is at 0.2 meshing metrics spectrum.

**Table 9**CFD Meshing Parameters for Design 1 – 10 For Internal and External Flow Analysis

Parameter	Value
Internal Geometry Wall Distance from Model	0.2 (mm)
External Geometry Wall Distance from Model (Inlet and Wall)	2 (mm)
External Geometry Wall Distance from Model (Outlet)	5 (mm)
Local Surface Meshing Sizing (Inlet, Outlet, and Wall)	0.01 (m)
Local Surface Meshing Sizing (Domain)	0.001 (m)
Local Surface Meshing Sizing (Model)	0.0001 (m)
Surface and Volume Growth Rate	1.2
Surface Mesh Minimum Size	1.00E-05 (m)
Surface Mesh Maximum Size	0.01 (m)
Cell Volume Element	Polyhedral
Fill Type	Uniform, Smoothing Transition

# **Governing Equations in CFD Analysis**

The Navier-Stokes equation for a fully developed laminar fluid flow (Body water) with a constant density ( $\rho$ ) and dynamic viscosity ( $\mu$ ) was used in solving the CFD simulation.

$$\rho \frac{\partial u}{\partial t} - \mu \nabla^2 u + \rho(u. \nabla) u + \nabla p = F, \tag{1}$$

The variables of  $\rho$ , u, and  $\mu$  are density (kg/m³), velocity (m/s), and dynamic viscosity (kg/m.s).  $\nabla$  this is defined as the del operator, and p is defined as pressure (Pa). F is forces within the system [18, 66-68].

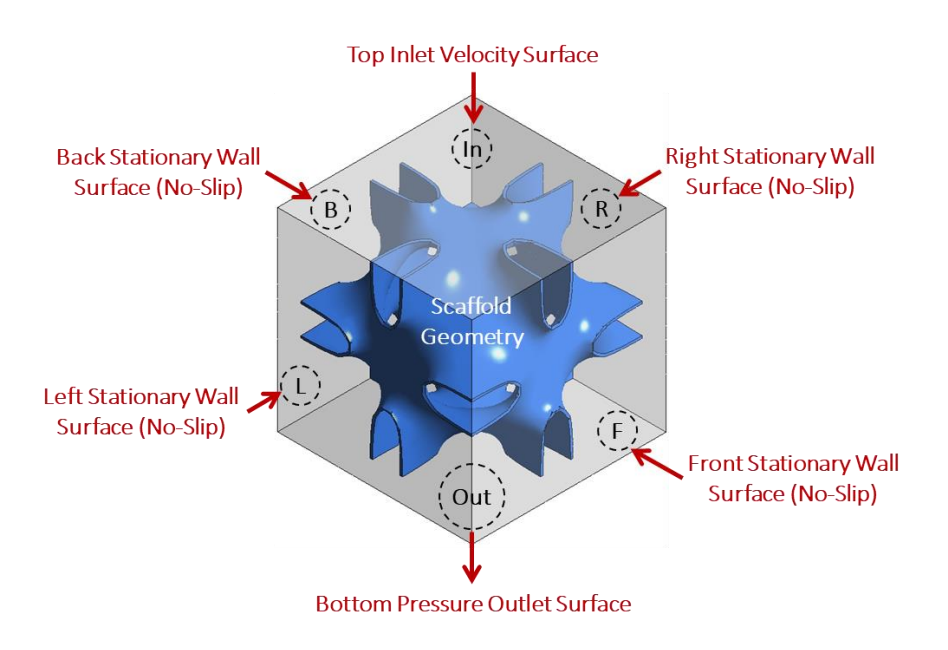
# Fluid Properties and Boundary Conditions

Fluid dynamics analyses are essential for understanding blood flow through porous micro-structures, as they determine the transport of nutrients and oxygen to cells and the flushing of toxic waste [69]. No stem cells were directly included in this study. It is assumed that the flow of material is Newtonian, and the presence of stem cells will not significantly affect fluid properties. However, the parameters chosen for this study are based on a simulated body fluid reported in [16], having a temperature of 37 °C, a density of 1000 kg/m³, and a dynamic viscosity of 1.45E-3 Pa.s. The boundary conditions of the CFD models are demonstrated in

Figure 15. The inlet velocity value is 0.001 m/s [16]. In addition, the model and the wall have the no-slip condition applied to their surface structures. As for the pressure outlet, the gauge pressure is set to 0 Pa.

Figure 15

The boundary conditions of the CFD models



*Note.* The inlet velocity is set at 0.001 m/s, and the pressure outlet is at 0 Pa-g.

#### **Numerical Solutions**

The method that was used for the scheme of the simulation is the coupled scheme. The coupled scheme has an improvement over a non-coupled or segregated approach. The coupled scheme has a robust and efficient single-phase implementation for steady-state flows. In addition, it is using the coupled scheme benefits when the mesh quality is poor or if significant time steps are used [65].

The method used for the Gradient is a least squared cell-based. If a mesh is a skewed and distorted structure, the accuracy of the least-squares gradient method is equivalent to that of a node-based gradient. In addition, this method is less expensive in computing than a node-based gradient. As for the momentum, a Second-order upwind scheme is used to solve the momentum equation. The Second-order upwind Scheme is less diffusive than that of its First-order counterpart.

Furthermore, for the pseudo-time method, a Global Time Step was applied. It yields a specific explicit under-relaxation of the equation that can be controlled for an update of the computed variables for each iteration [65].

#### Verification and Validation

Verification and validation of computational modeling are critical to ensure the accuracy of the analysis. The numerical solution will reflect the natural transportation phenomena of the bone scaffold fluid properties.

## Validation

The published work of *Wang et al.* [16] was followed to validate the CFD models' accuracy. Their work focused on CFD analysis of a bone scaffold using Schwarz P design. The pressure and velocity values observed in this study are comparable to the results reported by

Wang *et al*. Only minor differences can be observed where both results show favorable values and likeness to one another. The variation of the values can be due to our CFD model's dimensions as well as the flow domain's tolerance around the bone scaffolds. In addition, the same boundary conditions and fluid properties were used in this study.

## Verification

The pressure and velocity boundary conditions were contrasted against the computational pressure and velocity results. For all simulations, it was observed that the boundary conditions were satisfied, remaining unchanged at the set boundary values, with the inlet velocity being at 0.001 m/s and the pressure outlet gauge being at 0 Pa.

#### **Results and Discussion**

## Internal Flow Simulation Pressure Contours Analysis

The internal flow simulation results for the models' profile pressure are shown in Figure 16. The pressure within the model displays higher pressure at the inlet velocity and gradually dissipates the pressure at the outlet. It results in satisfying the boundary condition of the model requirements.

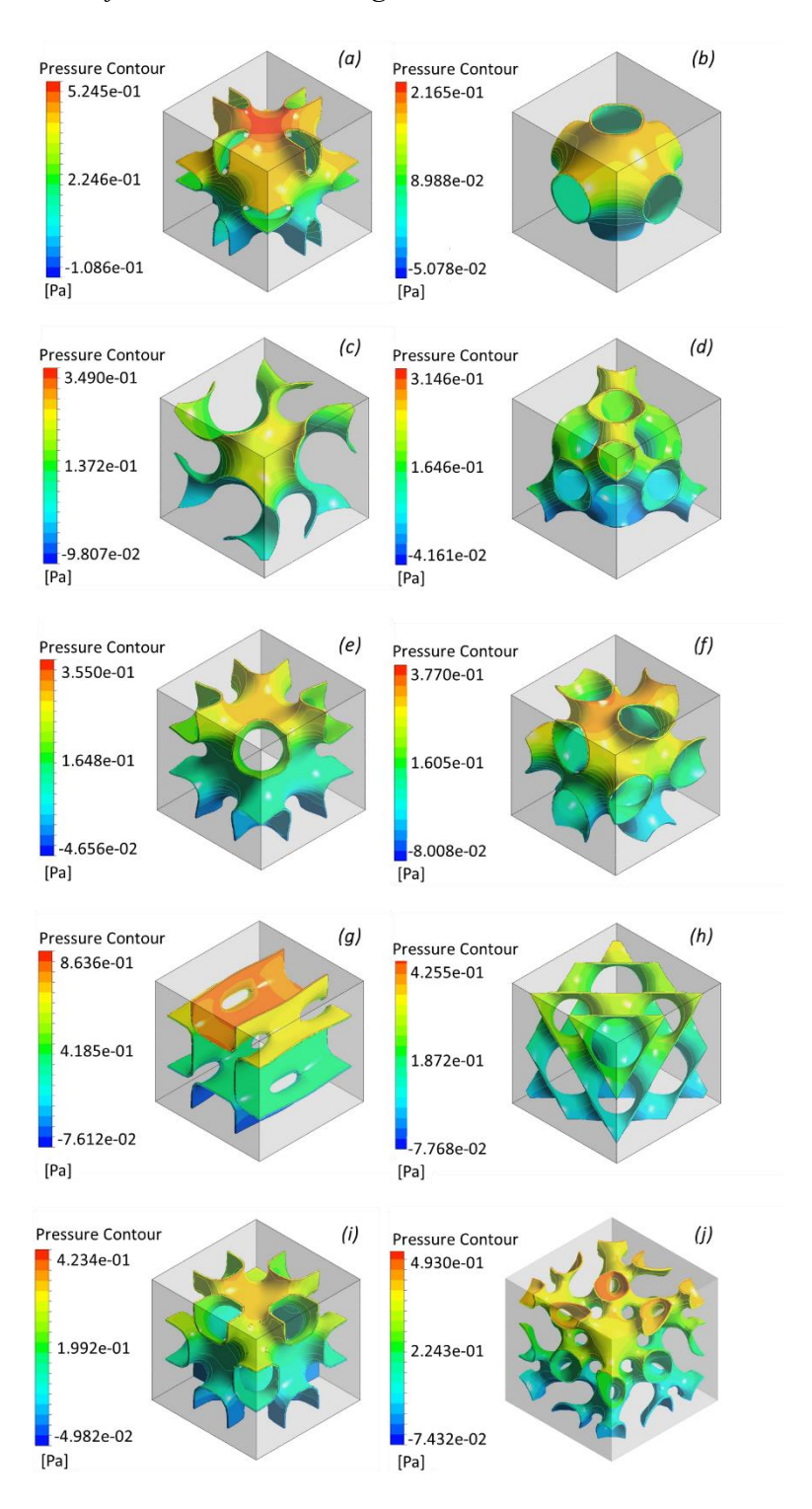
Thus, design (g) has the highest-pressure output, with design (a) following second to it. These models have a flatter surface area compared to design (b), i.e., Schwarz P, which has a more curved geometry. The range of the pressure output is 8.64E-1 to 2.17E-1 Pa.

In addition, design (b) has the lowest pressure output of all 10 TPMS models within the analysis. The geometry of design (b) has a decrease in pressure along the sides of the curved portion of the model. This results in the side of the scaffold increasing velocity in those areas. Furthermore, designs (h), (i), and (j) have moderate pressure value output within the study; these geometries have a greater curved surface area than that of design (b). Therefore, it leads to the

fluid passing through the model's pores to interact with the wall and cause a fraction on the surface, thus resulting in a pressure build-up.

Figure 16

Internal pressure contours for all 10 TPMS designs



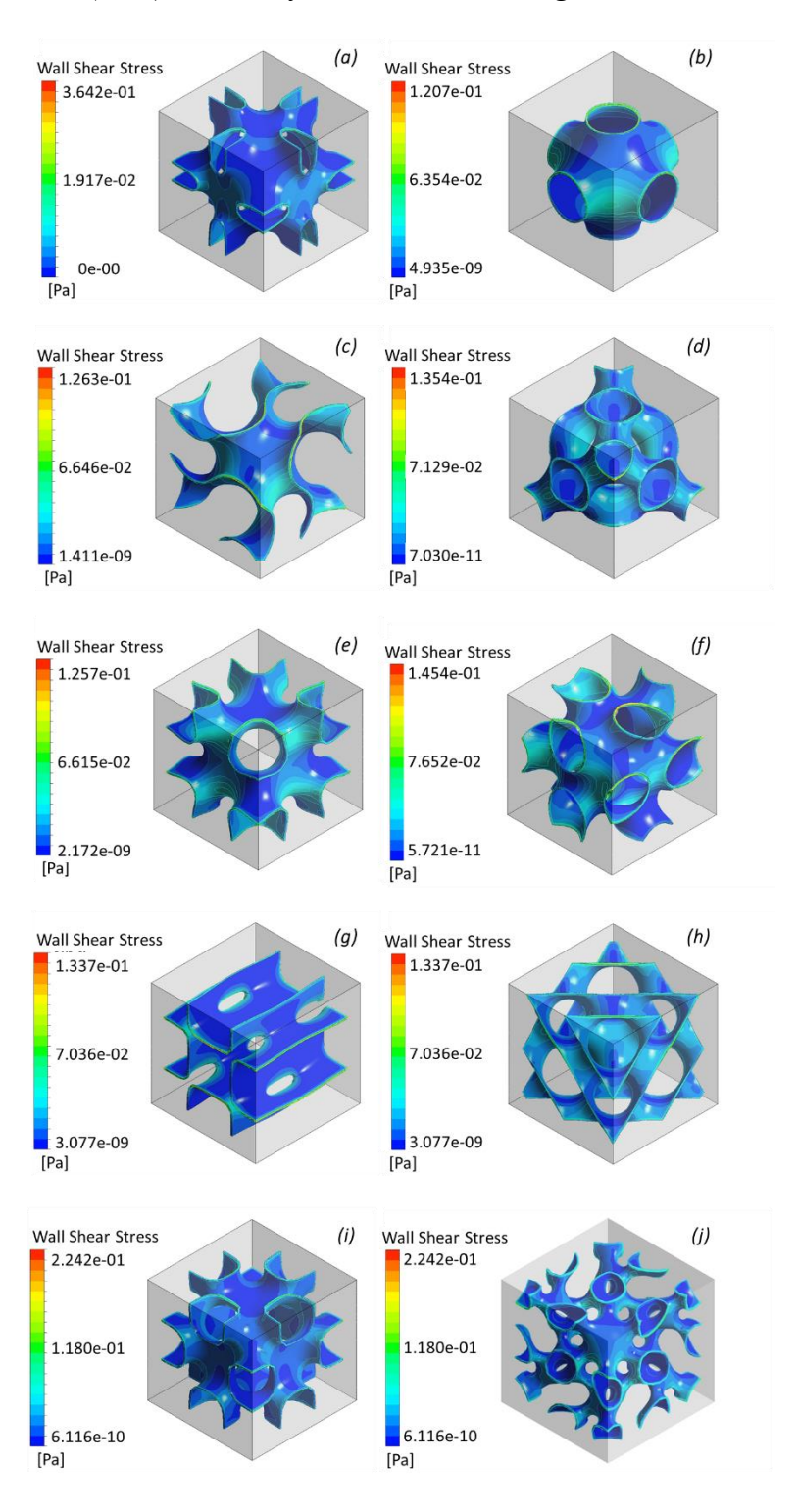
#### Internal Flow Simulation Wall Shear Stress Analysis

A Wall Shear Stress (WSS) Analysis was performed on all 10 TPMS designs; WSS is regarding the forces of fluid interactions along the wall of the structure on the model. Furthermore, the model's boundary condition is no-slip, and the fluid flow is laminar for the fluid properties. In Figure 11, the WSS's highest and lowest max ranges can be seen at 3.64E-1 to 1.21E-1 Pa, respectively. Design (a) and (g) have the highest values of WSS. In addition, these models also demonstrated higher pressure values.

Furthermore, the scaffold designs display a lower value gradient of WSS on curved segments on the models. Thus, these conditions of lower WSS values can promote bone proliferation for cell development. For average WSS values, 0.1 to 10 mPa must be around to induce healthy bone development. Thus, with the observation within Figure 17, the curved geometry can live within those desired conditions of lower WSS values that can be detailed with the channel and curved section of the geometry [21].

Figure 17

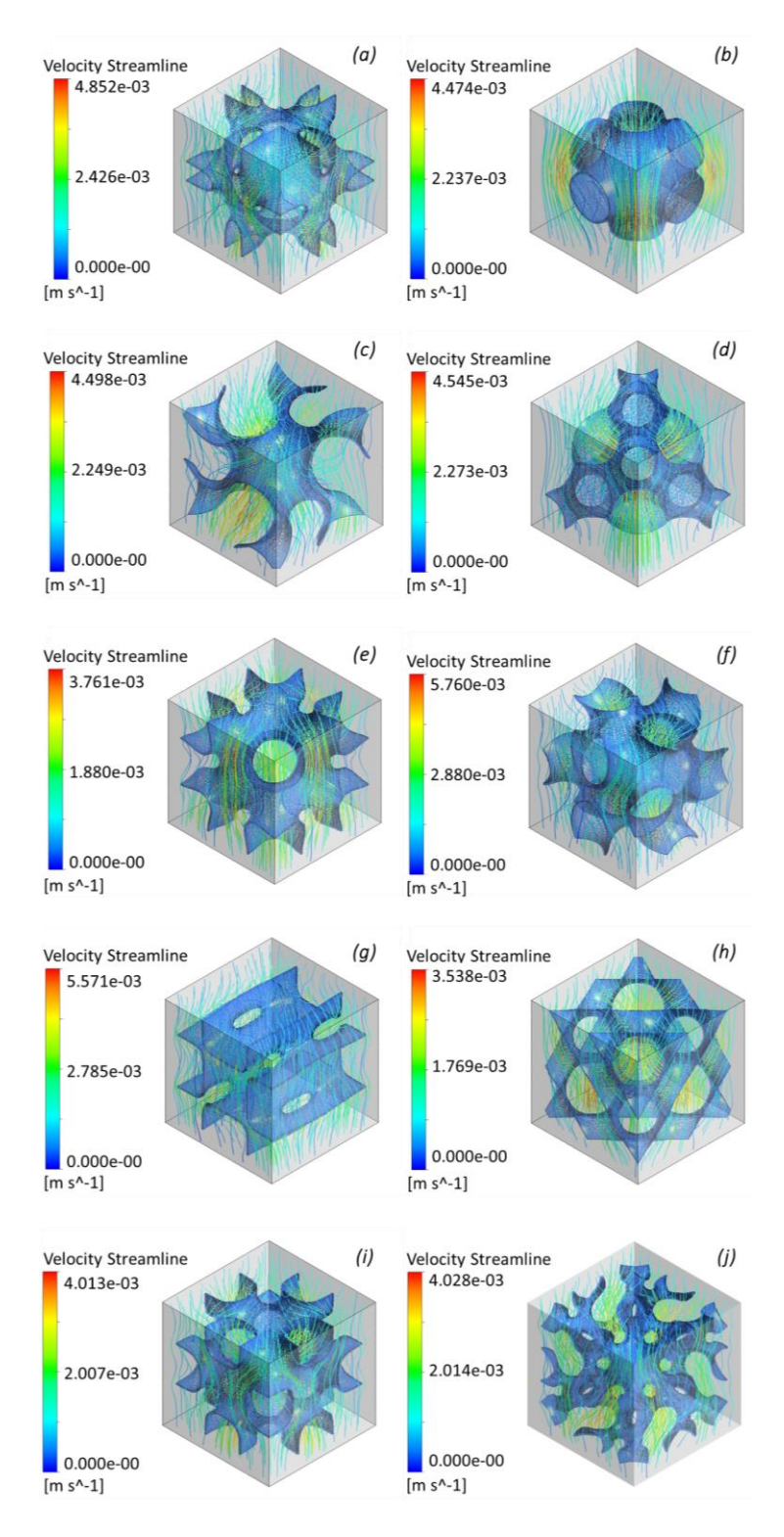
Internal wall shear stress (WSS) contours for all 10 TPMS designs.



## Internal Flow Simulation Velocity Streamline Analysis

Within Figure 18, the velocity streamlines analysis shows an increase in velocity along the curved section of the geometry. The range of max velocity streamlines is 5.76E-03 to 3.54E-03 (m/s). Furthermore, the max velocity value of design (f) is 5.76E-03 (m/s), with design (h) having a max velocity of 5.57-03 (m/s). Design (h), velocity can be seen slowing down at the flat segments of the structure due to the no-slip condition. The fluid flow passes into the narrow channels of the structure, resulting in an increase in velocity due to a decrease in cross-sectional area. As for design (d), the geometry consists of the structure mainly being developed into curved portions. Therefore, the velocity will increase within the narrow channels of the structure, resulting in a decrease in pressure within those sections. Thus, WSS can have an effect resulting in biofluid interaction along the surface structure. That will allow for bio-development to take place.

Figure 18
Internal velocity streamlines for all 10 TPMS designs.



#### External Flow Simulation Pressure Contour Analysis

The models' profile pressure of external flow simulation results can be seen in Figure 19. The pressure within the model displays higher pressure at the inlet velocity and gradually dissipates the pressure at the outlet. Thus, the results satisfy the boundary condition requirements. In addition, the maximum pressure value range is 9.14E-2, with the lowest being 4.0E-2 Pa.

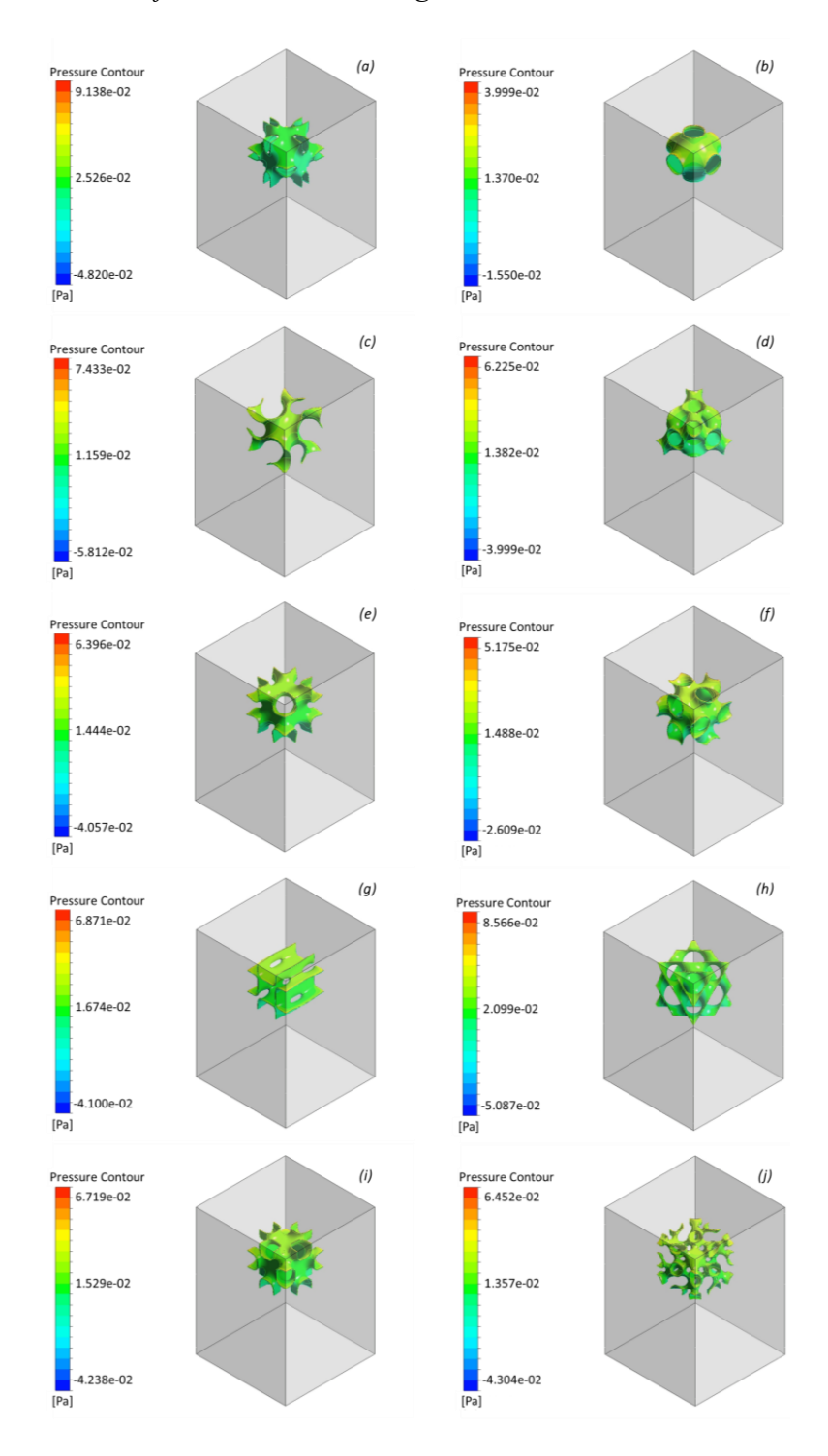
Design (a) yields the highest-pressure output within the inlet section, which contains the area of the highest-pressure location. In parallel to the internal flow, the flat surface area of the geometry, in collaboration with the small pores, creates a difficult flow path for the fluid to pass through. Thus, a cumulation of pressure is built up within the inlet portion of the fluid flow.

The design (b) produced the lowest pressure value output, much like it did within the internal flow. The geometry of design (b) has a decrease in pressure along the sides of the curved portion of the model, similar to the past result. In addition, the reduction in pressure can also be attributed to the dominant open pore at the inlet position, thus allowing the fluid flow to pass without difficulty.

Furthermore, design (h) yields a pressure output value of 8.57E-02. Unlike the internal flow counterpart, it yields an average pressure output of 4.26E-01. The increase in pressure can be attributed to the flow build-up within the scaffold along the inlet portion of the flow. Due to the complexity of the curvature, the flow is induced to interact along the structure's wall, slowing it down. This results in a model with a complex curvature structure capture the fluid, which will allow for biofluid to interact with the structure, resulting in the promotion of bone proliferation.

Figure 19

External pressure contours for all 10 TPMS designs.



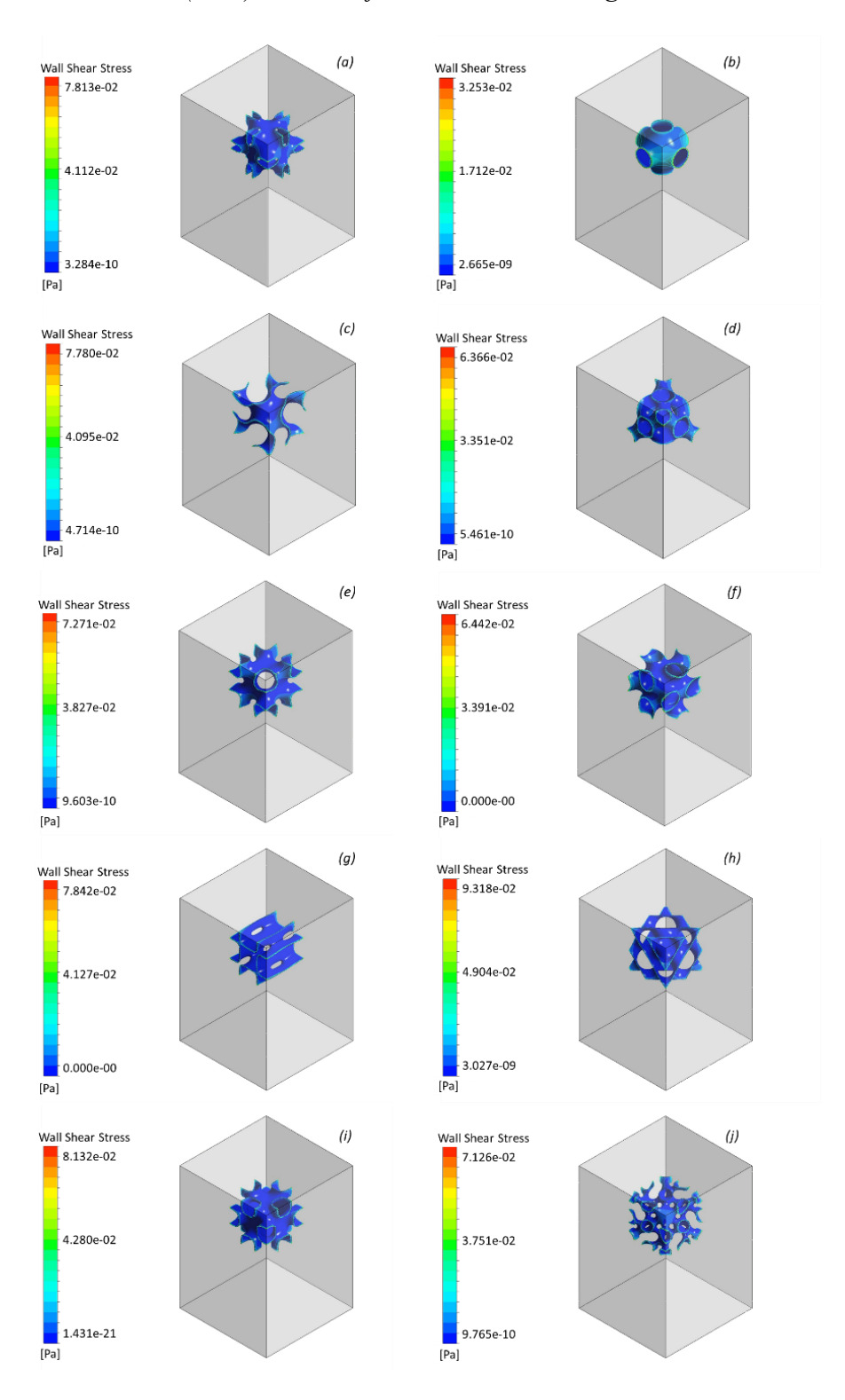
# External Flow Simulation Wall Shear Stress Analysis

With the evaluation of the WSS Analysis on the external flow that can be seen in Figure 20, the highest to lowest max values of WSS are 9.32E-02 and 3.25E-02 Pa. Thus, this also satisfies the desired conditions in promoting bone proliferation cell development [21], where the WSS average needs to be around 0.1 and 10 mPa.

Furthermore, design (h) displays the highest WSS value within the external flow analysis due to the fluid interaction that accrues with complex curved structures. With design (b), the curvature is simple compared to design (h), where design (b) WSS value is 3.25E-02 Pa and design (h) shows 9.31E-02 Pa.

Figure 20

External Wall Shear Stress (WSS) contours for all 10 TPMS designs.



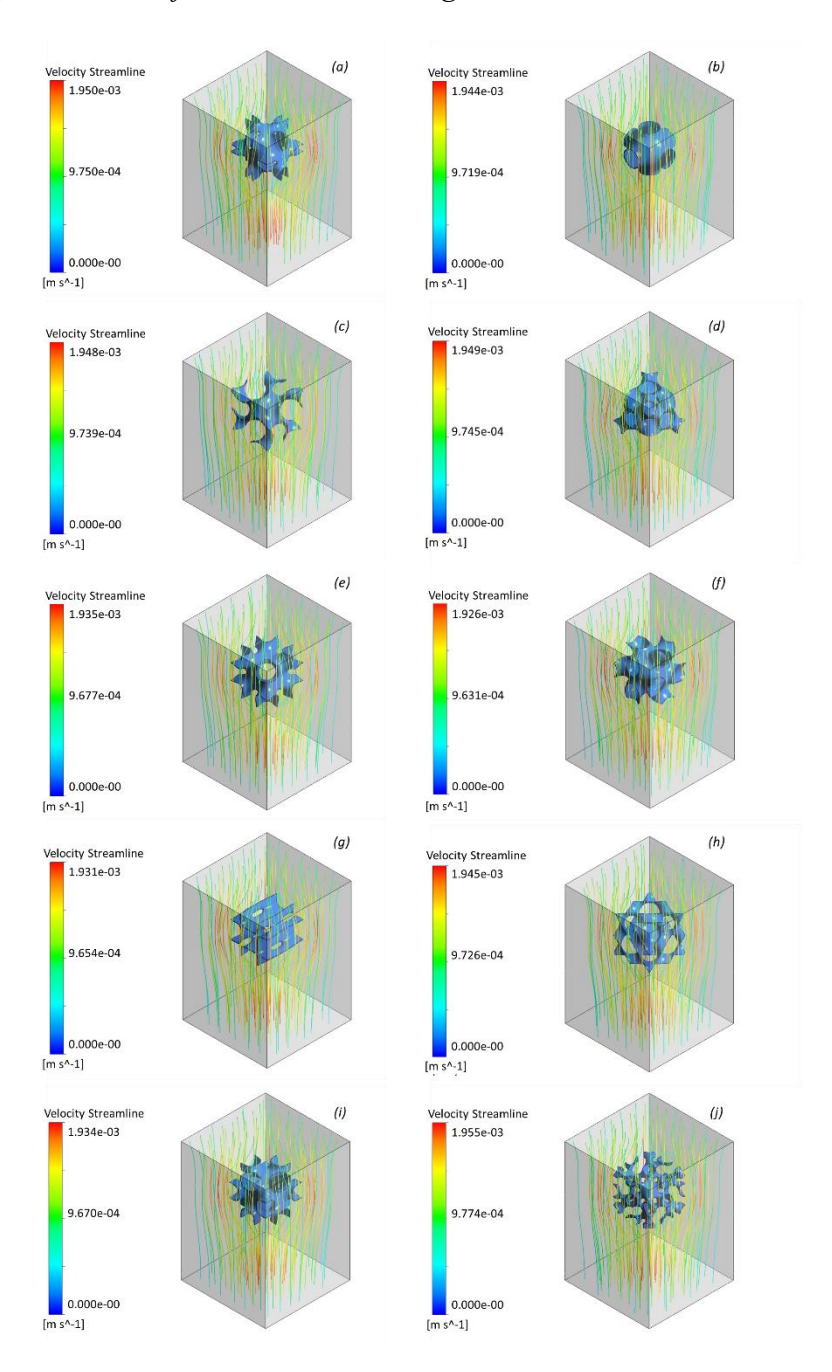
## External Flow Simulation Velocity Streamline Analysis

Within Figure 21, external velocity streamlines analysis shows the increase in velocity along the curved section of the geometry. The range of max velocity streamlines is 1.955E-03 (m/s), and the lowest velocity is 1.926E-03 (m/s).

Furthermore, the average max velocity is 1.942E-03 of all 10 TPMS designs. The velocity streamlines can be seen in increasing velocity as the fluid passes over the structure. In addition, the induction of a turbulent wake region development toward the end of the model is absent. This is due to the low-velocity initial conditions. Furthermore, when looking at designs like Schwarz G (design (c)), the depiction of turbulent motion can be seen along the internal curved sections of the scaffold. As the external velocity streamlines decrease within the inner channels of designs, this will lead to an increased pressure buildup as the fluid interacts with the model's walls. Furthermore, this will support the production of biofluid interaction and the development of bone structure.

Figure 21

External velocity streamlines for all 10 TPMS designs.



#### External Cubic Flow Simulation Pressure Contour Analysis

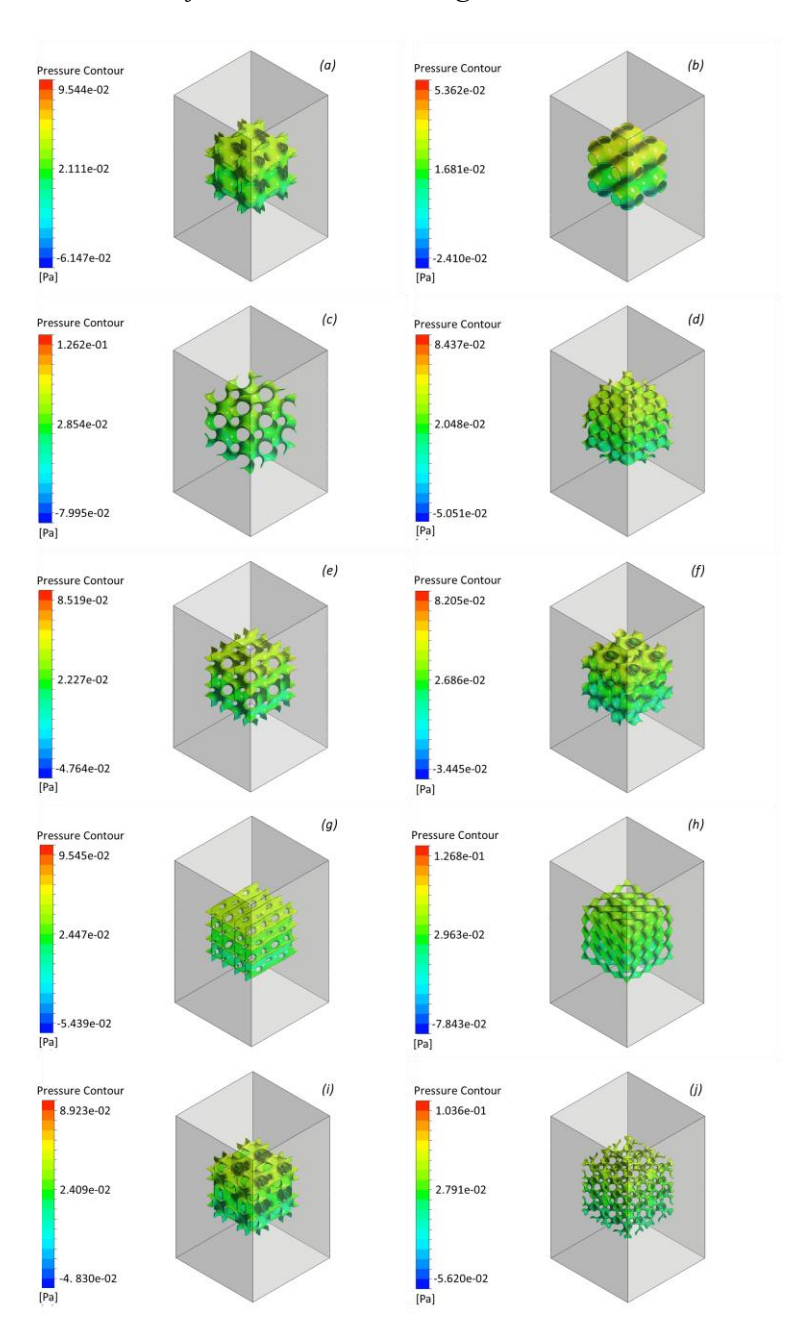
Figure 22 shows the models' profile pressure of external 6-by-6 mm cube flow simulation results. The pressure within the model displays higher pressure at the inlet velocity and gradually dissipates the pressure at the outlet. Thus, the results verify the boundary condition requirements. In addition, the maximum pressure value range is 1.262E-1 Pa, with the lowest being 5.362E-02 Pa, which comes for Schwarz Gyroid and Schwarz Primitive, respectively.

High pressure can be seen in designs Schwarz Gyroid, Diamond, and L models. A typical inclination they show is that the complex curvature allows fluid to build up within the model, resulting in pressure build-up. Additionally, the maximum pressure values are located at the top edges of the models, where the fluid would interact first. Furthermore, negative pressure values can result from suction occurring within the TPMS design, facilitating fluid flow in reverse to normal fluid.

As for models similar to Neovius and P.W. Hybrid, they have more surface area, yielding more interaction of moderate levels of pressure built up on the structures' surface. Thus, the Schwarz Primitive has optimal pressure output, yielding a maximum pressure of 5.362E-02, the lowest out of the 10 TPMS designs. Therefore, aiding in cell viability and survival within the hemodynamics of the blood shear flow, for pressure affects the biological activity of scaffolds and influences scaffold-cell interactions [15].

Figure 22

External Cubic pressure contours for all 10 TPMS designs.



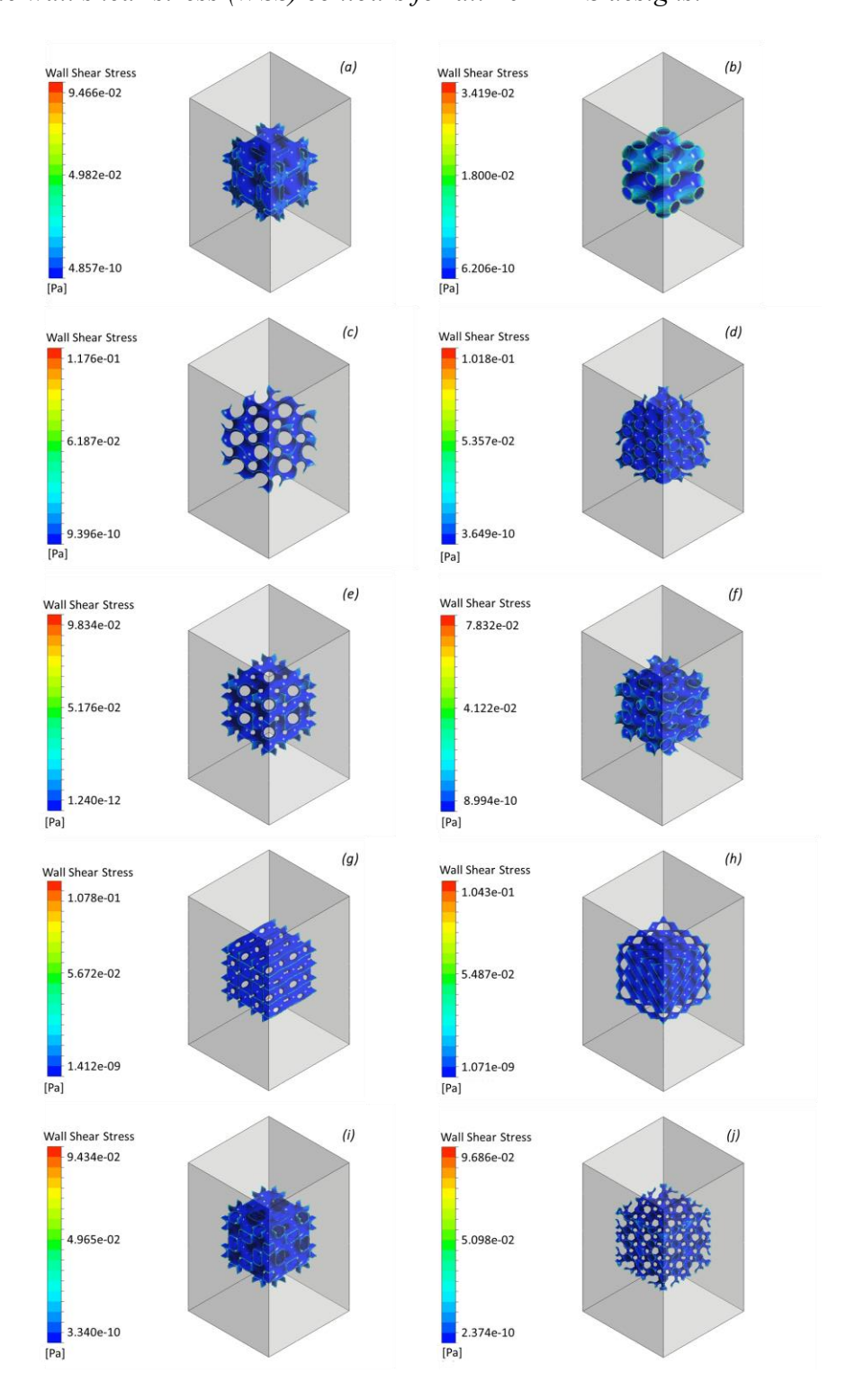
#### External Cubic Flow Simulation Wall Shear Stress Analysis

A wall shear stress (WSS) Analysis was performed on all 10 TPMS designs; WSS concerns the forces of fluid interactions along the structure's wall on the model. Furthermore, the boundary condition applied to the model is the no-slip condition on the walls, and the fluid flow properties are laminar. Within Figure 23, the highest and lowest maximum values of WSS are 1.176E-01 to 3.419e-02 Pa, respectively, for Schwarz Gyroid and Schwarz Primitive designs.

Additionally, this Schwarz Gyroid was also demonstrated to have higher pressure values, whereas the Schwarz Primitive displays had the lowest pressure outputs, which can be seen in Figure 22. Furthermore, it is essential to note that to satisfy the desired conditions for promoting bone proliferation cell development [6], the WSS average values should range around 0.1–10 mPa. In addition, if WSS is in the range of 0–30 mPa, it stimulates the overall biological activity of mesenchymal stromal cells (MSCs), which allows for the differentiation of a variety of cell types like bone cells, cartilage cells, etc., As for the range of 0.55–24 mPa stimulates the mineralization process of bone cells. Furthermore, WSS values above 60 mPa are linked to cell death [15]. Therefore, the analysis shows that Schwarz Primitive displays optimal characteristics for cell viability where the maximum WSS yields are at 3.419E-02 Pa—the lowest value within the 10 TPMS designs.

Figure 23

External Cubic wall shear stress (WSS) contours for all 10 TPMS designs.

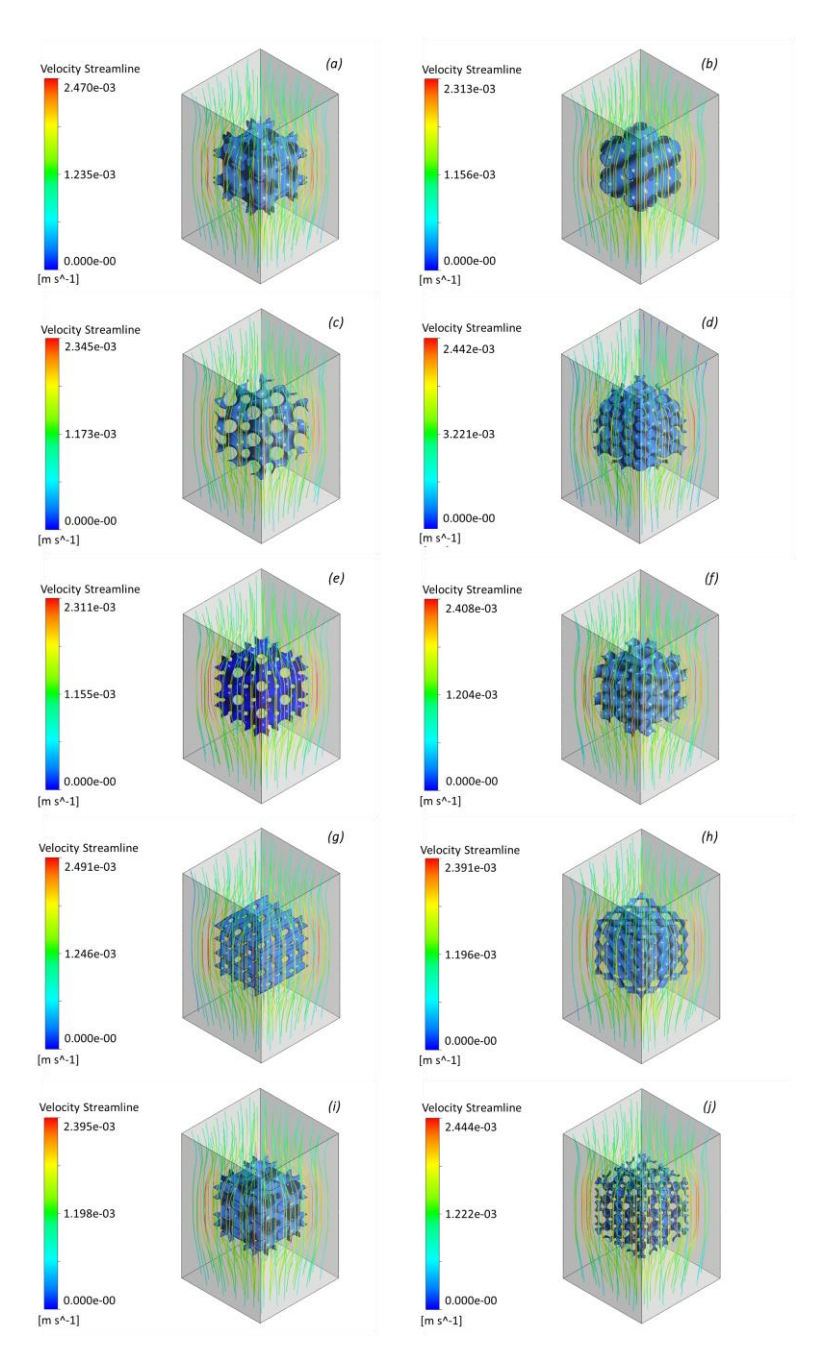


## External Cubic Flow Simulation Velocity Streamline Analysis

Within Figure 24, external velocity streamlines analysis shows the velocity increase along the geometry's outer section. The maximum to lowest velocity streamline range is 2.470e-03 and 0.00 m/s. Furthermore, Neovius yielded the maximum velocity in addition, with all 10 TPMS designs having the lowest velocity value being 0.00 m/s. Thus, a fluid characteristic that shows the velocity streamlines is the fluid flowing over the scaffold at a higher velocity with all 10 designs. Furthermore, designs with more complex curvature structures like Schwarz Gyroid or Diamond show decreased fluid flow velocity within the structure due to the fluid flow interacting with the scaffold wall. In addition, the induction of a turbulent wake region development toward the end of the model is absent due to the low-velocity initial conditions. Furthermore, this will support the production of biofluid interaction and the development of bone structure.

Figure 24

External Cubic velocity streamlines for all 10 TPMS designs.



## Significance and Biological Implications of the Results

It is critical to understand the influence of WSS, pressure, and velocity and how they affect cell viability. WSS affects the differentiation ability of cells to renew tissues and aids in forming a single cell layer that lines all blood vessels and regulates exchanges between the bloodstream and the surrounding tissues [69]. In addition, pressure affects cell viability and survival within the hemodynamics of the blood shear flow, potentially acting as a mechanical stimulus on cells; pressure also affects the biological activity of scaffolds and influences scaffold-cell interactions [69]. As for the importance of velocity, streamlines show how the bloodstream would pass through the scaffolds' architecture. Furthermore, velocity streamlines reveal how the bloodstream passes through the scaffold channels. Besides, capturing changes in velocity leads to implications in terms of cell-wall interactions, which give insights into where cell attachment and adhesion may occur.

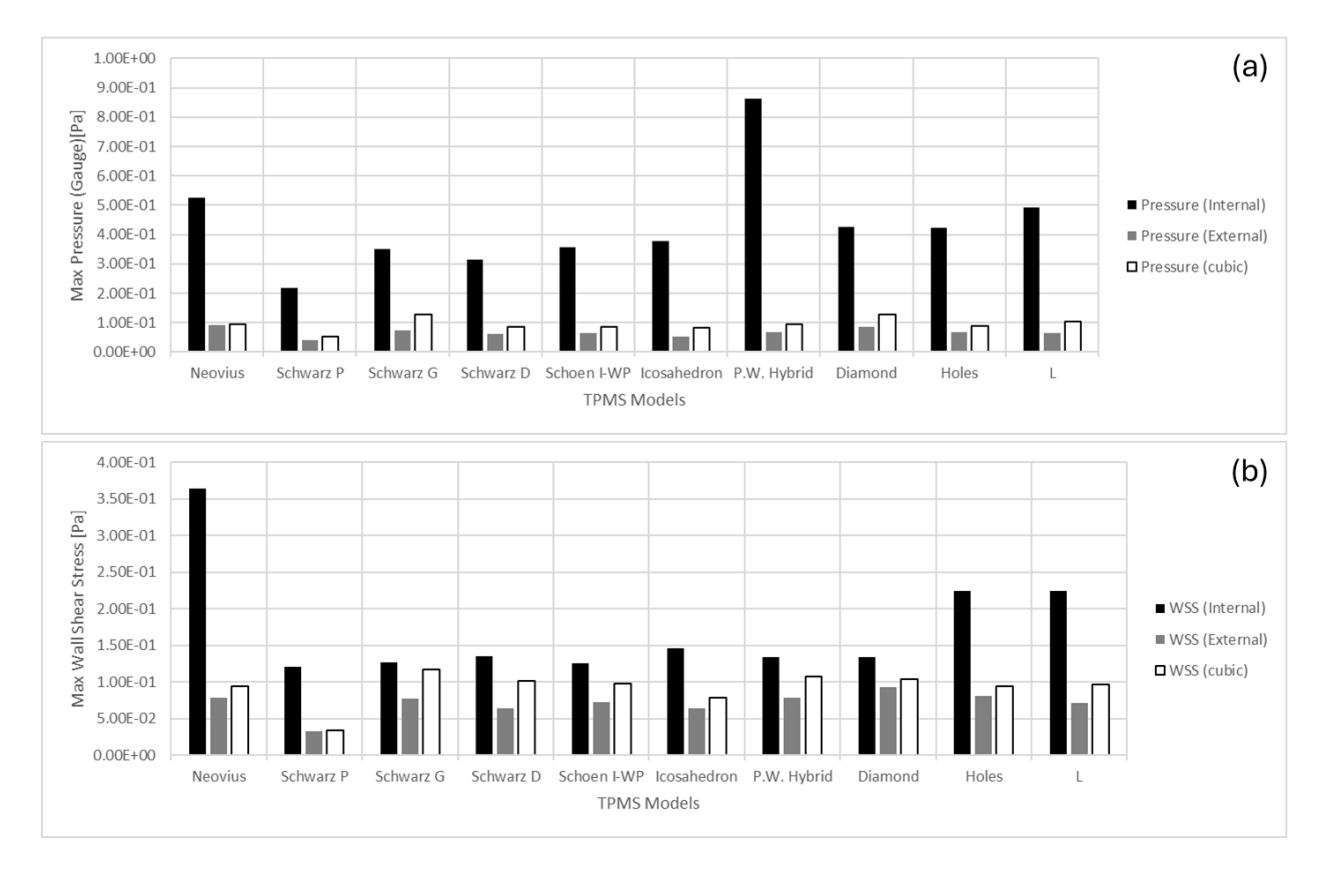
## **Identification of Optimal Designs**

It is essential to note that the lowest pressure and WSS results have the most potential for stem cell viability and allow osteoblast to occur.

Figure 25 illustrates a bar graph of maximum pressure (a) and WSS (b) for all TPMS scaffold designs. It was observed that *Schwarz P* would have a relatively favorable performance, having the lowest pressure and WSS level. Therefore, Schwarz P is the optimal design when considering the interaction of fluid properties. Furthermore, all Schwarz designs similarly showed favorable outcomes, having a low level of pressure and WSS. In addition, Schoen I-WP turned out to be a viable option as it comes as the second design in terms of WSS.

Figure 25

Bar graphs comparing maximum pressure and wall shear stress with respect to design 1-10



Please note that in terms of geometrical factors, porosity, shape, dimensions, and fluid-material interactions, additively manufactured scaffolds are expected to yield results similar to those reported in this study. However, material properties, composition, and manufacturing-related properties (such as surface roughness) will play a significant role in the fluid transport through the scaffolds, which may considerably affect the reported values of pressure, WSS, and velocity.

## **Summary**

In conclusion, the overall objective of this work is to fabricate a CFD model from Rhinoceros 3D software to identify the significant mechanisms within internal and external material transport for porous bone scaffolds using ANSYS software. Furthermore, the TPMS

scaffold designs of 10 internal-flow and 10 external-flow CFD models observed material transport fluid characteristics of flow velocity, flow pressure, and wall shear stress, respectively.

#### Internal Flow

The pressure flow analysis for internal flow findings shows that design 7 P.W. Hybrid has the highest-pressure output at 8.636E-01 Pa; this is a result of the architecture of the design being flatter than that of the more complex curved geometry. For instance, design models 2, 3, and 4 (Schwarz P, Schwarz G, and Schwarz D) are shown to have lower pressure due to the channels of the design allowing for more effortless fluid flow within the geometry, which can be seen within the internal flow velocity characteristics were the velocity streamline show an increase in the rate at a section where the design yields more complex curvature and more narrow channel for the fluid to travel. Furthermore, the WSS analysis of max ranges delivered at 3.64E-1 to 1.21E-1 Pa, Design 1: Neovius, and Design 7: P.W. Hybrid have the highest values of WSS in addition, and these scaffold designs also demonstrated to have higher values of pressure as well. In addition, average WSS values of 0.1 to 10 mPa induce bone development within a curved section and channels of the scaffolds that yield lower WSS values.

#### External Flow

The pressure flow analysis for external flow showed that the maximum pressure value range is 9.14E-2 to 4.00E-2 Pa, respectively. Thus, design 1: Neovius yields the highest-pressure output along the inlet section; this is due to the flat surface area of the geometry in collaboration with the small pores. This results in a difficult flow path; thus, a cumulation of pressure is built up within the inlet portion of the fluid flow. The geometry of design 2: Schwarz P has a decrease in pressure along the sides of the curved portion; the reduction in pressure can also be attributed to the dominant open pore at the inlet position, allowing the fluid flow to pass without difficulty.

Design 8: Diamond has an increase in pressure at a value of 8.57E-02 Pa; this can be attributed to the flow build-up within the structure along the inlet portion of the flow. The scaffold design has complex curved channels capturing the fluid, which can be seen within the velocity streamline section of the results, aiding in this understanding of fluid dynamics analysis. In addition, the max values of WSS are 9.32E-02 and 3.25E-02 Pa from highest to lowest. Thus, the desired conditions for promoting bone proliferation cell development can be produced within the scaffold design section where the channels and curved portion of the geometry yield lower values.

Furthermore, design 8: Diamond displays have the highest WSS values within the external flow analysis due to the fluid interaction that accrues with complex curved structures. External velocity streamlines analysis shows the range of max velocity streamlines is 1.955E-03, and the lowest velocity is 0.00 (m/s), with an average max velocity of 1.942E-03. The analysis shows an increase in rate as the fluid passes over the structure. In addition, the induction of a turbulent wake region development toward the end of the model is absent. Also, designs with curved geometries, like that of Schwarz G, can be seen to have turbulent motion within the internal channels of the scaffold. Furthermore, external velocity streamlines decrease within the inner channels of designs, leading to an increased pressure build-up as the fluid interacts with the model's walls, thus aiding in the production of biofluid interaction and the development of bone structure.

#### External Cubic Flow

The profile pressure of the external cubic TPMS model's flow simulation findings has displayed favorable low pressure for the Schwarz Primitive model with a max gauge pressure of 5.362E-02 Pa. Furthermore, high pressure can be seen in Schwarz Gyroid, Diamond, and L

scaffold designs. This is due to the complex curvature of the structure's designs, which have fluid buildup with the porous regions. Therefore, negative pressure has also been noted due to the suction occurring within the TPMS design, which aids in biofluid interaction that will induce proliferation—as for the TPMS scaffold of Neovius and P.W. Hybrid displayed moderate levels of pressure built along the surface of the structures within the environmental interaction.

Likewise, WSS observations have shown that Schwarz Primitive designs yield the lowest value with the external cubic evaluation; Schwarz Primitive has a WSS of 3.4 mPa, respectively. This value of WSS falls within the range of promoting bone proliferation cell development and the ability to stimulate the biological activity of MSCs to aid in differentiating bone cell types of cells. Therefore, Schwarz Primitive displays optimal characteristics for cell viability within WSS out of all 10 TPMS designs. In addition, optimal pressure output will improve cell viability and survival within the hemodynamics of the blood shear flow.

# Chapter 5: A Convolutional Neural Network Model for In-Process Assessment of the Complex Porosity of Additively Manufactured Bone Tissue Scaffolds Goal and Objectives

The future use of bone scaffold tissue engineering has considerable potential for treating and regenerating bone fractures, defects, and breaks. Even with significant improvements in bone tissue engineering, further understanding of the design aspect of the bone scaffold is still needed.

This work aims to develop a Convolutional Neural Network (CNN) model for predicting the different topologies of triply periodic minimal surface (TPMS) scaffolds. 500 images were taken from a monochromatic, high-resolution charge-coupled device (CCD) camera of the SimuBone scaffold developed for the fused deposition modeling (FDM) process.

The results of this study provide a detailed analysis of the CNN model's performance.

The accuracy metric indicates the percentage of correct class predictions made by the model during the training phase. Conversely, the loss metric represents the percentage of incorrect predictions. The validation accuracy and loss metrics, derived from the training phase, contribute to developing the F-Score, a comprehensive measure of the CNN model's overall performance determined by the testing phase.

#### **Material and Methods**

The material and method section details the development and fabrication process for the TPMS scaffold geometry using Rhino 7 software. The additive manufacturing process used is fused deposition modeling (FDM) printing, with the material filament being SimuBone. Furthermore, this section will also discuss the details of image acquisition for the CNN machine-learning process.

#### Materials

The material selected for the development of the TPMS bone scaffold is SimuBone. SimuBone properties yield similarities to bone structure. It can stimulate cortical and cancellous bone, thus allowing it to be a viable alternative to cadaver bone specimens. Therefore, SimuBone is ideal for patient-specific treatments because it is ISO-certified to eliminate bacteria attraction on developed bone scaffolds. SimuBone also contains an additive property of PLA, allowing it to function efficiently in the FDM extrusion process.

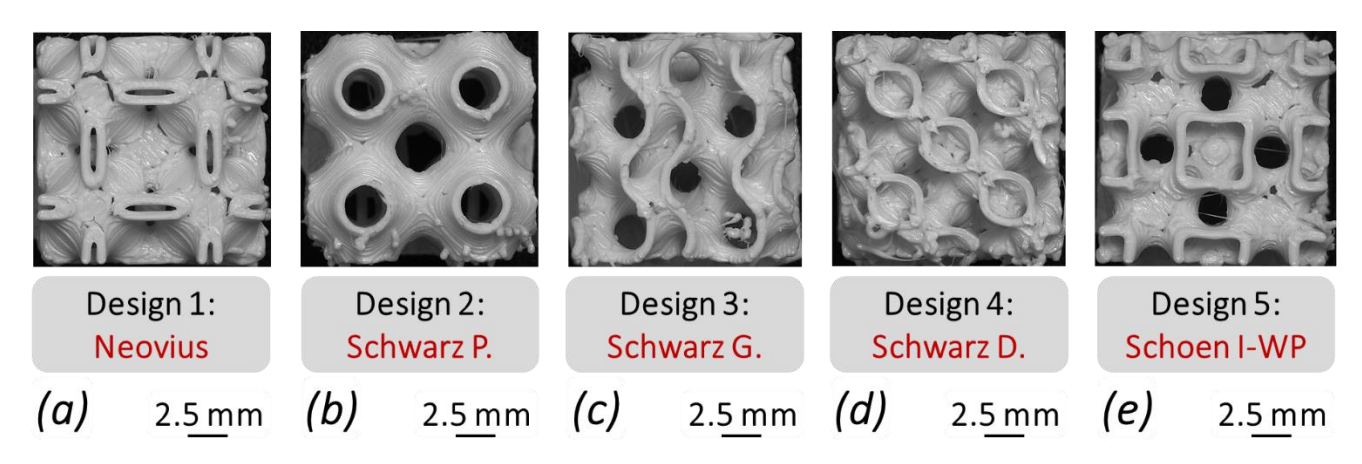
# **Experimental Designs**

## TPMS Scaffolds

This study selected a triply periodic minimal surface (TPMS) scaffold for analysis due to its significant benefits in bone regeneration and mechanical properties. The TPMS scaffolds mimic biological bone tissue and allow for improved integration of the surrounding tissue, aiding in cellular processes [55]. Additionally, the TMPS scaffolds have shown the capability to be versatile, allowing them to satisfy several design requirements and mechanical characteristics [54].

Figure 26

TPMS designs of all 5 scaffold designs.



Thus, Figure 26 shows all 5 TPMS scaffold designs used in the analysis. The TPMS scaffold is 15 by 15 mm and was additively manufactured using the fused deposition modeling (FDM) 3D printing process.

Furthermore, significant features of the scaffold designs of Neovius (a), Schwarz P. (b), and Schoen I-WP (e) show similar simplistic curvature that allows for ease of fabrication. In contrast, the counterparts show more complex curvature for Schwarz G. (c) and Schwarz D. (d), resulting in a more complicated fabrication process.

# **Modeling Software**

The modeling software used in developing the TPMS scaffold is Rhino 7 Grasshopper, with the Millipede and Weaverbird programs. Table 10 shows the parameters equations used for all 5 TPMS designs with respect to Figure 26. Thus, this modeling software aided in producing 3D solid models of the parametric equations.

**Table 10**Parametric equations of TPMS design 1 - 5.

Equations	TPMS Design
$3(\cos(x) + \cos(y) + \cos(z)) + 4(\cos(x)\cos(y)\cos(x))$	(1)
$-(\cos(x) + \cos(y) + \cos(z))$	(2)
$\sin(x)\cos(y) + \sin(z)\cos(x) + \sin(y)\cos(z)$	(3)
cos(x) cos(y) cos(z) - sin(x) sin(y) sin(z)	(4)
$2(\cos(x)\cos(y) + \cos(y)\cos(z) + \cos(z)\cos(x)) - (\cos(2x) + \cos(2y) + \cos(2z)$	(5)

Furthermore, Table 11 yields the parameters used in developing the TPMS scaffold for Rhion 7. The scaffold dimensions used within the Rhino 7 software were 6 cubic mm. The step iteration of Schwarz P. (b) design through Schoen I-WP design (e) has their step values set to 7. step values set to 7.710; additionally, designs Neovius have step parameter functions as an iterative tool that will improve the sharpness of the TPMS scaffold design as it computes through the parametric equations. Therefore, TPMS scaffold Neovius has a high step value set to aid in developing an improved 3D rendering of the TPMS scaffold model. The Merged Toggle function was used with its values set to true. This parameters operation is a collection of Boolean functions within the 3D development of the TPMS models.

Furthermore, the IsoValue is a collection of double-precision floating-point values; the value set for this parameter is -0.269. The ArrBox Count parameter values are set to 2 for this operation, merging multiple unit structures concerning the x, y, and z coordinates to formulate a solid single cubic structure. Thus, a value of 2 results in the production of a 4-unit cell configuration. The level parameter values are set to 1 for the level operates the effects of subdivision iteration on the surface face on the scaffold design. As for the WBThickness

parameter, it affects the wall thickness of the scaffold, thus operating as the porosity function for all scaffold designs. This value was set to 0.15 mm for all 10 TPMS scaffold models.

**Table 11**Rhion 7 parameters for all 5 TPMS scaffolds.

Parameters	Values
Model Dimensions (mm <sup>3</sup> )	6
Step	7.710
step For Model (a) and (j)	18.710
Merged toggle	TRUE
IsoValue	-0.269
ArrBox (x,y,z) Count	2
Level	1
WBThickness Distance (mm)	0.15

*Note.* Neovius has a step value of 18.710 to aid model accuracy.

# Image Capturing

Images for all 5 TPMS scaffolds were acquired using a monochromatic, high-resolution charge-coupled device (CCD) camera, following the procedure detailed in [70, 71]. A total of 500 images were captured for the development and validation of the CNN model. Furthermore, only the four sides of the scaffolds were utilized in the classification process, and the top image was excluded due to significant topology differences between the designs.

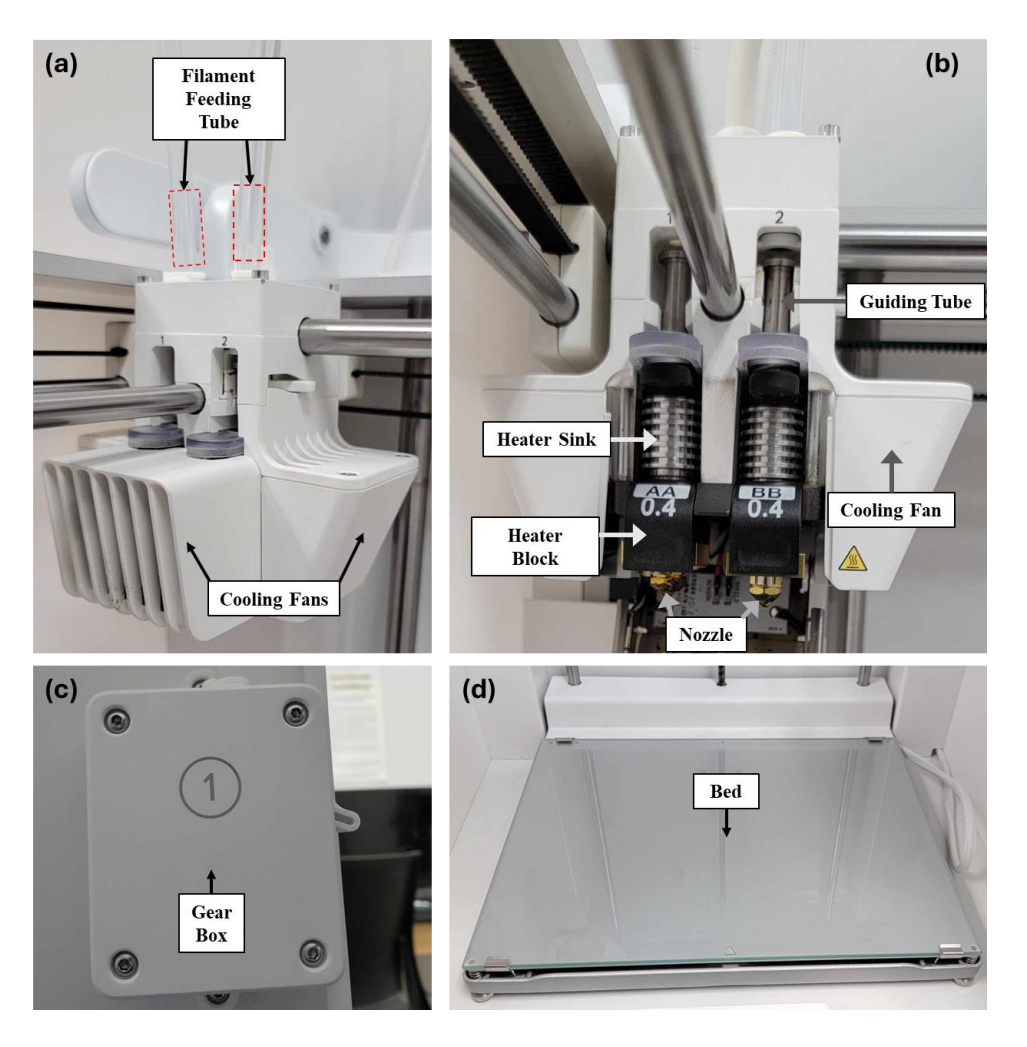
#### **3D-Fabrication Process**

## Fused Deposition Modeling Process

The fabrication process used in developing the bone scaffold is FDM 3D printing. Thus, Figure 27 yields a material transport and deposition diagram in the fused deposition modeling (FDM) additive manufacturing (AM) process. Therefore, filament material is fed within the head of the extruder using SimuBone material with a diameter of 2.85 mm. This led to the stepper motor within the bowed tube, which will guide the filament within the heating block of the FDM printer. The filament will be heated, altering the material structure to make it moldable. The heating block significantly affects the viscosity and rheology of the filament's materials. This moldable form of the filament will have the characteristic of a non-Newtonian fluid flow, with the material deposited out of the micronozzle printer head below the heating block. As polymer material is being deposited onto the heated bed of the build plate, the heat difference between the micronozzle head and the build plate will allow the molten polymer to adhere, producing the first layer of the TPMS scaffolds. The adhesion of the polymer to the bed plate will repeat in an iterative process to construct the bone scaffold, with each layer building on one another, binding the molten polymer into a robust structural bond.

Figure 27

A schematic diagram of material transport and deposition in fused deposition modeling (FDM) additive manufacturing process.



#### Cura Parameters

Cura was used for the G-coding software to fabricate the TPMS scaffolds. Thus, Table 12 yields the parameter types and values reflective of the FDM process. Equation (1) calculates the pore percentage for a solid cube produced from the same SimuBone material that was fabricated. Comparing the difference in mass for the solid cube and porous scaffold with equal dimensional size and dividing it by the solid cube results in a percentage of the scaffold's missing mass, thus representing the pore percentage of the TPMS bone scaffold value.

$$Pore\ Percentage = \left(\frac{Solid\ Cube - Scaffold}{Solid\ Cube}\right) *\ 100\%$$
 (1)

As mentioned before, the dimension of the cubic scaffold is 15-by-15 mm after scaling the model using a built-in function of the Cura program. The layer height parameter is set to 200  $\mu$ m, followed by a layer width of 300  $\mu$ m. The porous bone scaffold's infill density is also set to 100 %. The nozzle size is 400  $\mu$ m, with the bed plate temperature set to 60 °C and a printing speed of 10 mm/s. The deposition head (heating block) temperature is set to 240 °C with a flow rate of 120 %; for the build plate adhesion type used, it is a brim. This adhesion type was selected to aid in the protection of the warpage along with the print quality of the scaffolds. This FDM Cura process produced 200 TPMS bone scaffolds, with each design replicated 20 times.

**Table 12**Cura setting with the fabrication parameters of the TPMS scaffold for all 5 designs and fatigue bar, torsion bar, and tensile bar.

Parameter	Type	Level [Unit]	
Medical Composite	Material	SimuBone	
Scaffold Porosity Average	Design	78 [%]	
Scaffold Dimensions	Design	15x15x15 [mm]	
Layer Height (Thickness)	Design	200 [μm]	
Layer (Line) Width	Design	300 [μm]	
Infill Density	Design	100 [%]	
Nozzle Size	Machine	400 [μm]	
Bed Temperature	Machine	60 [°C]	
Print Speed	Machine	10 [mm/s]	

Deposition Head Temperature	Machine	240 [°C]
Flow (Feed) Rate	Machine	120 [%]
Build Plate Adhesion Type	Machine	Brim

#### **CNN Process**

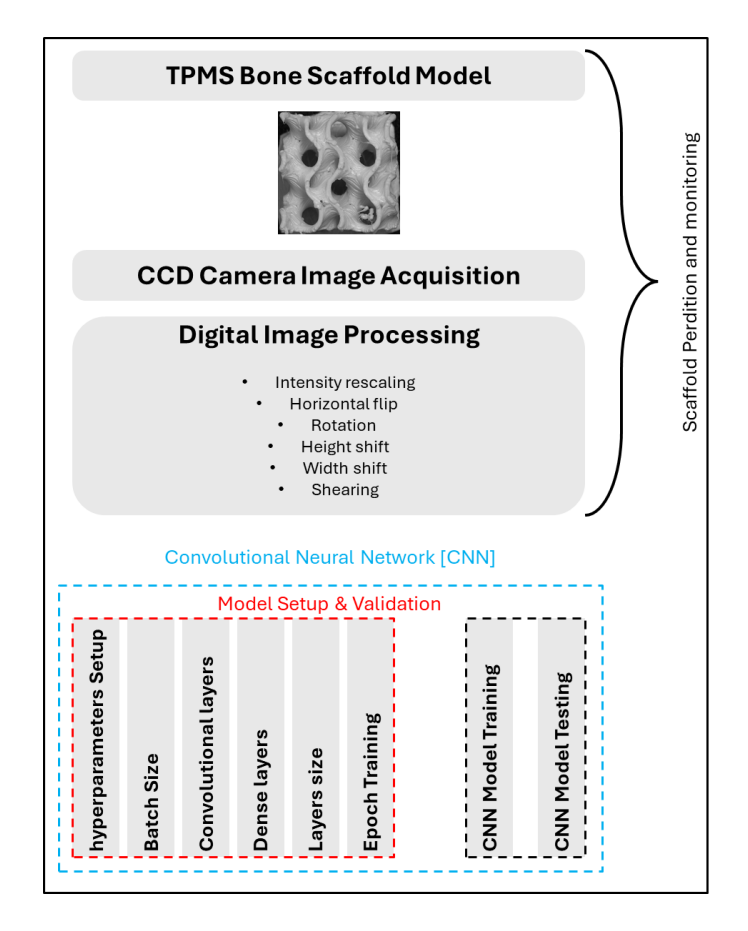
Convolutional neural network (CNN) machine learning is an artificial neural network for image recognition and processing. CNN has the capability to recognize and predict images for a vast data sample pool. It will be trained to be proficient in calculating different topologies of TPMS scaffolds. The CNN model was developed using Python coding software and imported libraries.

## Class Categorization

The CNN process evaluates a 5-class CNN framework that consists of all TPMS designs. Figure 28 depicts the workflow of the CNN model process. The first phase of the CNN process consists of scaffold perdition and monitoring for the image acquisition, which is collected from the CCD camera process. In addition, the digital image process will have its properties distorted by rescaling, horizontal flip, rotation, height, and width shifts, and shearing of the scaffold image. The second phase will consist of a CNN model, where the setup and validation will be conducted using the training and testing code.

Figure 28

Workflow of CNN code model, image acquisition, model setup, and validation



## Training Code for Prediction

The training phase of the CNN model uses the Tensorflow and Keras libraries, importing the image data generator, sequential, dense, activation, flatten, conv2D, and max pooling 2D functions within the training code. Furthermore, the data processing of the digital image process uses the image data generator function to rescale the image intensity. Additionally, this function allows for the images to be altered during training of the images. The initial/ input layer uses Con2D, a function of the layer size with a step size/stride of the x and y coordinates. Con2D operation creates a convolution kernel with the layer input over a single spatial dimension to

produce a tensor of outputs. In addition, the activation function used for its operations must be rectified in a linear unit.

Furthermore, the max pooling 2D was used with a pool size of 2-by-2 for the max pooling 2D input along its spatial dimensions of the maximum value over an input for each input channel. The flatten function controls the reduction dimensionality, which converts the 2D images into a 1D output that can be calculated within the dense layers. The dense operates by classifying images based on production from convolutional layers.

## Testing Code for Validation

The testing phase of the CNN model uses Tensorflow, Keras, and sklearn libraries, importing the cv2, regular expression (re), random, and numpy functions within the testing code. The cv2 function operates the main module in OpenCV, a straightforward interface for working with image and video processing functions. The re function specifies a set of strings matching the module, which allows the check on specific string matches within a re. The random function is an operator that allows for the mix of data to ensure that the testing code can make correct predictions. The numpy function is a multidimensional array object used for scientific computing. Numpy is used to calculate the confusion matrix calculation and F-score.

## Hyper Parameters

The Hyper Parameters section will encompass the following parameters: batch size, convolutional layers, dense layers, layer size, and epoch iterations. It will also detail each parameter's operating functions on the CNN system.

Batch size defines the number of samples used within one epoch to train a neural network for the low values of the batch size, which results in the collection of greater sample pool data for training within the classes. The convolution layer converts all the pixels in its receptive field

into a single value. Additionally, layer size is a variable function that adjusts the system's complexity. Increasing convolutional layers will improve the overall accuracy of the CNN model.

Furthermore, the single value produced from the convolutional layer is then calculated through the dense layer. Moreover, layer size is also a variable function within the dense layer, similar to the convolutional layer. The dense layer for each neuron within the neural network will compute a weighted average of the input to pass through the respective output. Layer size functions are similar to those of computational meshing. Layer size operates similarly to a grid system for higher numbers, resulting in a more refined grid placement. This allows for an image for the CNN model for more accurate calculation with the respective convolution and dense layer function. Epoch training is an iterative process that consists of analyzing data that is sorted by batch size. Thus, a higher epoch value allows for more refined accuracy within the CNN model.

#### **Results and Discussion**

## CNN Hyperparameter Optimization

The CNN hyperparameter optimization section encompasses the CNN code's value parameters and their effect on accuracy, loss, validation accuracy, validation loss, and F-score for a 5-class model.

**Table 13**Hyperparameters optimization setting ranges for Batch size, Convolutional layers, Dense layers, Layer size, and Epoch iteration

Batch Size	Convolutional Layers	Dense Layers	Layer Size	Epoch Iterations
8	4	2	32	20

16	4	2	32	20
32	4	2	32	20
64	4	2	32	20
128	4	2	32	20
16	2	2	32	20
16	3	2	32	20
16	4	2	32	20
16	5	2	32	20
16	6	2	32	20
16	4	2	32	20
16	4	3	32	20
16	4	4	32	20
16	4	5	32	20
16	4	6	32	20
16	4	2	2	20
16	4	2	4	20
16	4	2	8	20
16	4	2	16	20
16	4	2	32	20
16	4	2	32	10
16	4	2	32	15
16	4	2	32	20
16	4	2	32	25

16	4	2	32	30

Furthermore, Table 13 shows the ranges used in determining the optimal values. The default values within this analysis are 16 for Batch size, 4 for Convolutional layers, 2 for Dense layers, 32 for layer size, and 20 for Epoch training iterations. Additionally, the ranges for the hyperparameter of Batch size are 8, 16, 32, 64, and 128. The convolutional and dense layers range from 2 to 6, increasing by 1 per simulation group. As for layer size analysis, it ranges from 2, 4, 8, 16, and 32. The epoch training iterating range is 10 to 30, increasing by 5 per simulation group.

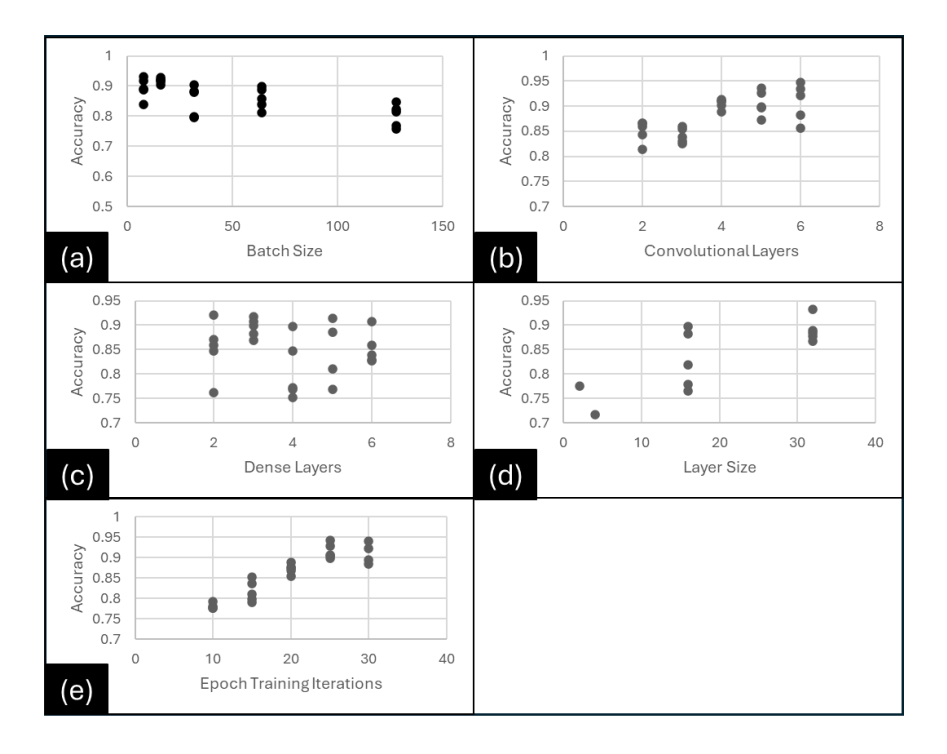
# Accuracy of CNN

Therefore, Figure 29 yields the effect of accuracy concerning the hyperparameter ranges within a 5-class CNN model. Figure 29 (a) shows the impact of the Batch size of lower to higher values, with a Batch size of 8 and 16 shown to produce an accuracy percentage of 89% and 91%, respectively, as the Batch size increases to higher values like that of 64 and 128 the accuracy of decreased linearly and for a Batch size of 128 yielded an accuracy of 80%. Therefore, batch sizes with lower values showed more preferred accuracy, which will aid in developing the CNN model for the higher classes. Additionally, the accuracy of the batch sizes 8 and 16 yields similar accuracy; however, 16 showed improved grouping over the accuracy of the batch size 8. This can be due to feeding the CNN model with a larger sample pool than a size 16.

Figure 29 (b) shows the effect of convolutional layers. Low accuracy is associated with low convolutional layers. Convolutional layers 2 and 3 produce a value of 84%. In addition, similar to batch size, the convolutional layers have a linear increase, with a convolutional layer of 6 having a value of 90%. Thus, increasing the convolutional layer allows for a more detailed depiction of the CNN model.

Figure 29

Change in accuracy with respect to hyper parameters



Note. (a) accuracy vs. batch size, (b) accuracy vs. convolutional layers, (c) accuracy vs. dense layers, (d) accuracy vs. layer size, (e) accuracy vs epoch iterations

Figure 29 (c) shows the relationship between the effects of dense layers on accuracy. The dense layers show that 3 produces the most optimal parameters, while the grouping of the 5 replications shows the most consistent. Additionally, the average accuracy produced from it is 89.50%. Values that were not a dense layer of 3 showed inconsistent results, with the grouping average significantly decreasing as the dense layer values were increased. Dense layers 4, 5, and 6 showed an average accuracy of 80.77%, 81.30%, and 85.22%, respectively. Thus, the dense layer value of 3 performs the most adequately.

Figure 29 (d) yields the influence of layer size on the CNN model. Since layer size affects the performance of convolutional and dense layers, layer size is a function of the 2

operators. A sufficient amount of data is not transmitted to the convolutional layer at lower values. This also results in inadequate dense layer neurons to compute the values into a precise response, thus having the CNN model diverge with incorrect values. Therefore, a higher layer size value will result in significantly improved accuracy of the CNN model. The increase in layer size also increases computational time for lower values of 2, the training section to a 10-minute run time. For higher values, the run time equaled 17 minutes, but with great accuracy and no diverted solutions.

Figure 29 (e) details the Epoch training iterations for optimal performance from a range of 10 to 30 simulations. A plateau in performance can be seen at the start of the 25-iteration.

Additionally, the range stability continues to yield similar accuracy values when increased to 30 Epoch. Furthermore, it can be seen that lower values will yield poor accuracy performance, leading to a divergence in image predictions of the CNN model. Additionally, the grouping of the iteration mark at 25 Epoch shows an improved grouping of more than 30 Epoch values. This is due to the over-training within the CNN model, causing overfeeding of the prediction solution, leading to slower convergence.

## Loss of CNN

Figure 30 shows the loss within the train portion of the CNN model. Thus, Figure 30 (a) shows that the loss is affected by changes in batch size. For accuracy, a trend can be seen much like that of Figure 29, where the loss within the system will increase as the batch size increases. Therefore, the batch size of 16 delivers the lowest loss percentage, at 22.64% on average.

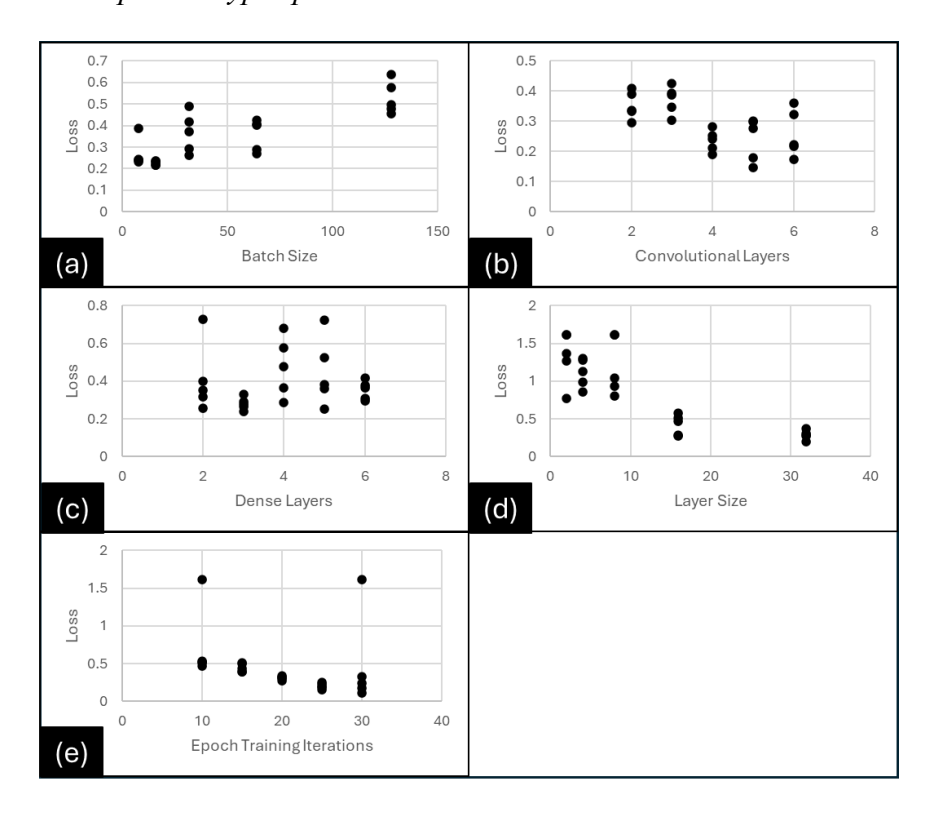
Figure 30 (b) yields the effects of how the Convolutional layers improve the loss percentage within the CNN model. Thus, a conventional layer of 4 shows to deliver a more

consistent and reliable value within the CNN model, making it the most preferred parameter when evaluating for loss efficacy.

Figure 30 (c) shows dense layers with a similar pattern to the previous analysis. The optimal parameter within the loss observation is a dense layer of 3 due to consistent grouping and low loss percentage values, which aids in creating a more accurate CNN model for predicting the TPMS scaffold topology.

Figure 30

Change in loss with respect to hyper parameters



*Note*. (a) loss vs. batch size, (b) loss vs. convolutional layers, (c) loss vs. dense layers, (d) loss vs. layer size, (e) loss vs. epoch iterations

Figure 30 (d) patterns also display that a higher layer size results in optimal performance due to the layer size yielding a loss value of 28.52% average at 32-layer size and with a layer

size of lower is shown to produce a loss value of 132.43% average at a layer size of 8. Furthermore, Figure 30 (e) also displays the consistency and optimal performance of iteration values of 25 Epoch, for the grouping of the simulation shows the plateau around that section.

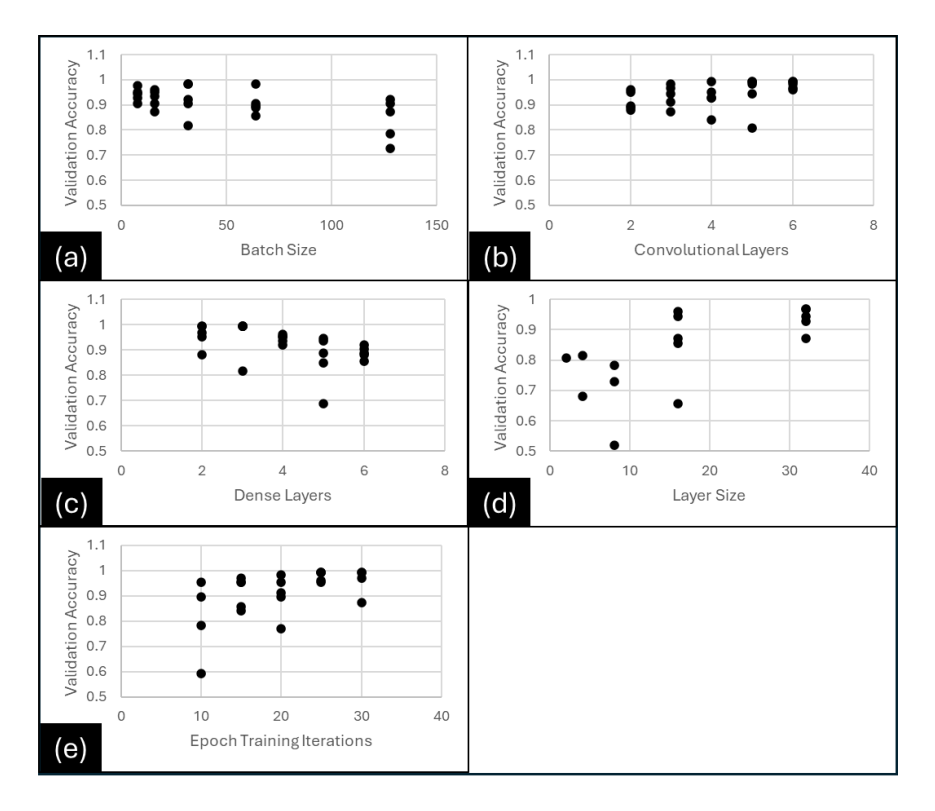
## Validation Accuracy of CNN

Figure 31 shows the validation accuracy of the training section of the code. The observation of Figure 31 (a) shows that a batch size of 8 has outperformed a batch size of 16 due to the grouping consisting of an average validation accuracy percentage. A batch size of 8 produced 94.08%, and a batch size of 16 produced 92.48% validation accuracy. Additionally, an increase in batch size value leads to a decrease in validation accuracy.

Thus, Figure 31 (b) yields that the optimal convolution layer quantities for validation accuracy are still seen at 6 layers. This shows that it outperforms all other ranges within the study. As for the dense layer within Figure 31 (c) shows that a dense layer of 3 is still seen as the preferred parameter setting. All ranges of the 5 replications of the test show only 1 outline falling below 81.60%. For the other 4 replications show a validation accuracy of 99.2%.

Figure 31

Change in validation accuracy with respect to hyper parameters



Note. (a) validation accuracy vs. batch size, (b) validation accuracy vs. convolutional layers, (c) validation accuracy vs. dense layers, (d) validation accuracy vs. layer size, (e) validation accuracy vs epoch iterations

Figure 31 (d) shows that a layer size of 32 is still preferred for the most optimal validation accuracy. A trend similar to that of the pass evaluation has been demonstrated that lower values yield poor CNN model performance. Furthermore, Figure 31 (e) shows the same trend of plateauing at 25 Epoch, with this parameter being the most consistent and robust setting.

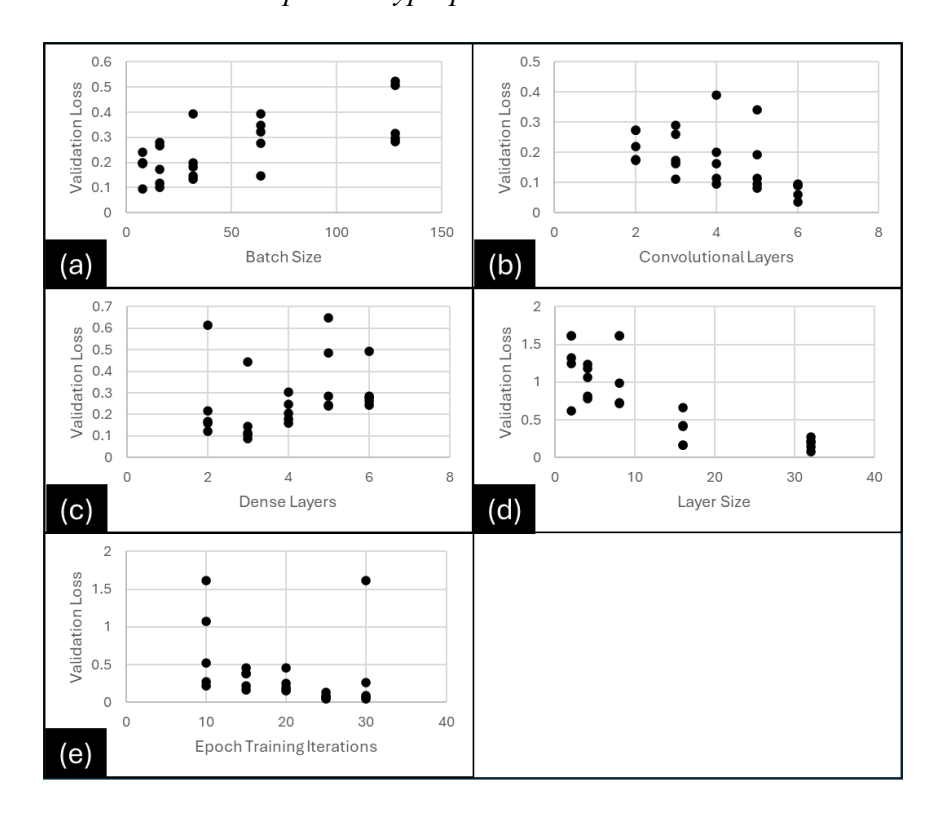
# Validation Loss of CNN

Figure 32 displays the finding of the loss percentage validation within the code's training section, and Figure 32 (a) shows the validation loss percentage of batch size 8 to 128. It is noted

that the performance of 8 and 16 shows the preferred optimal range for the CNN model. The batch sizes of 8 and 16 yield a validation loss of an average of 18.61% and 18.75%. Furthermore, a batch size of 16 has been shown to yield more consistent results of lower loss, thus making it the optimal section. Additionally, Figure 32 (b) shows similar patterns to the previous analysis for the convolutional layer quantity of 6, which was shown to have the highest performance and most consistent outputs.

Figure 32

Change in validation loss with respect to hyperparameters



*Note*. (a) validation loss vs. batch size, (b) validation loss vs. convolutional layers, (c) validation loss vs. dense layers, (d) validation loss vs. layer size, (e) validation loss vs. epoch iterations

Figure 32 (c) displays the effects of dense layers on validation loss. Furthermore, the finding shows that the dense layer size of 3 has outperformed the other selected values.

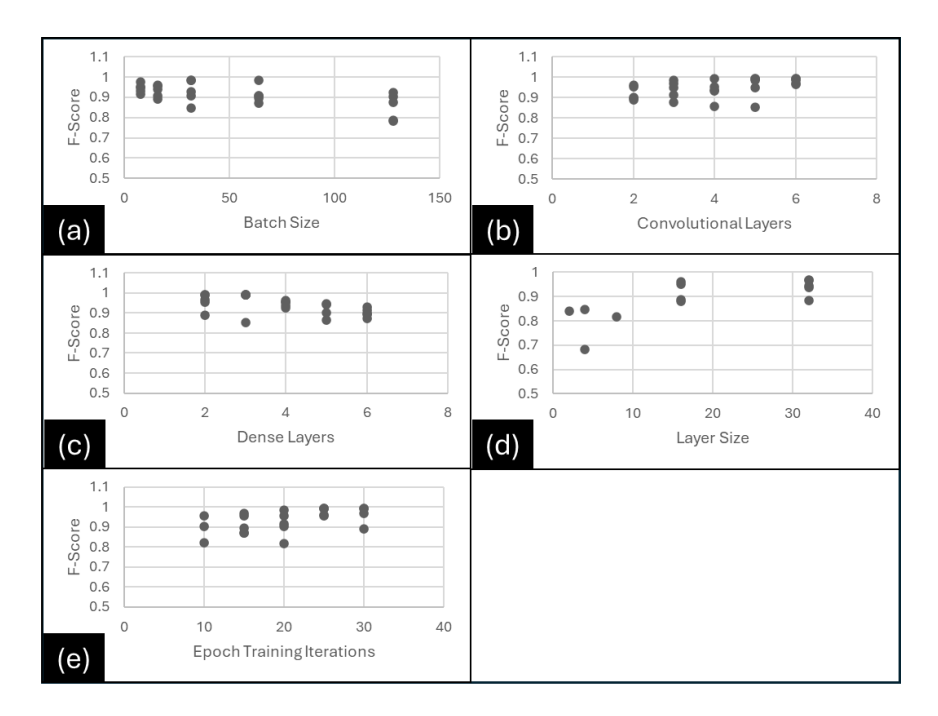
Additionally, Figure 32 (d) confirms that higher layer size produces a more accurate solution due to the low loss values. Figure 32 (e) shows that an Epoch value of 25 produces more accurate and reliable training than prior parameters.

## F-Score Effects on Hyper Parameters

Figure 33 shows the effects of the hyperparameters on the F-Score. For F-Score, the ability of the CNN model to accurately predict the classification dataset. The F-score was acquired within the testing analysis portion of the code. Thus, the data in Figure 33 shows a similar consist of the hyperparameters displaying that convolutional layer, dense layer, layer size, and Epoch training parameters are all acceptable at 6, 3, 32, and 25, respectively. The only parameter that showed differences from the previous evaluation was batch size. The most favorable parameter within this scenario is a batch size of 8. For having a greater F-Score with an average percent of 94.55% than that of a batch size of 16.

Figure 33

Change in F-Score with respect to hyper parameters



*Note*. (a) F-Score vs. batch size, (b) F-Score vs. convolutional layers, (c) F-Score vs. dense layers, (d) F-Score vs. layer size, (e) F-Score vs. epoch iterations

Therefore, Table 14 shows the optimized hyperparameters for the CNN model for a classification size of 5. The batch size is set to 16 due to the consistent grouping that 16 can produce. Furthermore, the difference between the 16 and 8 batch size percentages is negligible. Convolutional layer parameters are 6, for it showed superb performance within all evaluations for accuracy to F-Score. Dense layer and layer size are set to 3 and 32, respectively. For also show significant performance within all evaluations. Epoch training parameters are set to 25 for this parameter, which displays quality F-Score production and is consistent throughout the other analysis.

**Table 14**Hyperparameters optimization values for Batch size, Convolutional layers, Dense layers, Layer size, and Epoch iteration

Batch Size	Convolutional Layers	Dense Layers	Layer Size	<b>Epoch Training Iterations</b>
16	6	3	32	25

#### **Summary**

In conclusion, the findings of the CNN model's optimal parameters are 16, 6, 3, 32, and 25 for the respective hyperparameters of batch size, convolutional layers, dense layers, layer size, and Epoch training. The batch size evaluation of performance within the CNN model details that a batch size of 16 shows significant improvement with a batch size of 16, along with improved replication consistency. A trend can be seen following batch size 16, which shows improved CNN model accuracy within loss, validation accuracy, and validation loss. Only the F-Score shows improved performance with a batch size of 8. Thus, the significant improvement of a batch size 16 leads to the optimal selection. As for the convolutional layer within all analyses shows that the value of 6 displayed the most optimal CNN model performance, producing the most accurate and consistent findings within the replications. A dense layer value of 3 also leads to a similar trend when observing the evaluation tests. Furthermore, the same pattern trend can be depicted in the following way: the layer size of 32 and Epoch training of 25. Thus, the optimal parameter values yield for the 5-class framework CNN model achieves ideal accuracy for topology prediction for TPMS scaffolds.

#### **Chapter 6: Conclusion**

This overarching research investigates bone tissue engineering treatment of bone regeneration in the application of fractures, defects, and diseases. A significant understanding of porous bone scaffold design for patient-specific treatment was evaluated to understand design parameters.

To investigate the mechanical performance of the material PAPC (I, II, and V) on the TPMS scaffold of Schwarz-Primitive, Neovius, Schwarz-Diamond, and Schwarz-Gyroid.

Displayed that Neovius and Schwarz-Diamond designs had a relatively high level of compression modulus compared to the Schwarz-Primitive and Schwarz-Gyroid designs.

Furthermore, the Neovius TPMS scaffold yielded the highest level of bulk density. Additionally, PAPC-I and V showed the most comparable level of compression modulus, while PAPC-II performed the lowest level of stiffness within the analysis. In addition, PAPC-V bulk density is similar to PAPC-II bulk density.

As for the biomaterial of SimuBone, the findings detail that it is suitable for bone tissue engineering. The torsion analysis showed a highly rigid shear modulus of  $714.79 \pm 11.97$  MPa and an ultimate yield strength average of 44 MPa. The tensile strength evaluations showed impressive strength with a compression modulus of  $5404.20 \pm 192.30$  MPa. In addition, the 10 TPMS designs compared to its compression modulus show that P.W. Hybrid performance was superior to that of the other TPMS scaffolds.

Furthermore, the evaluation of the 10 TPMS scaffold for internal, external, and cubic external flow of material transport characteristics was assessed for flow velocity, pressure, and WSS within the CFD analysis. The internal observation showed that the TPMS design of the P.W. Hybrid yields the highest-pressure outputs. In addition, the Schwarz family model design

yielded lower pressure due to the open and accessible flow provided by the Schwarz architecture. The WSS analysis shows that Neovius and P.W. Hybrid yield the highest values. Still, they are not the most optimal for the induction of bone development compared to other designs like that of Schwarz Primitive.

The external flow details the trend of the TPMS model Neovius producing the highest pressure within the external flow evaluation. This is due to Neovius having pre-dominant flat surface faces, causing the fluid to have built-up pressure collecting on the inlet section of the model. Furthermore, it shows that the Schwarz Primitive yields ideal performance within fluid dynamics. The Schwarz Primitive displays low fluid pressure resistance due to its dominant open pores from the architecture of the scaffold, which allows for easy flow. In addition, Schwarz Primitive yields the lowest WSS value of all 10 TPMS designs, thus making it ideal for promoting bone proliferation cell development.

The external cubic flow evaluation also shows that a 2-by-2-unit cell scaffold structure yields a Schwarz Primitive design with the most optimal performance out of the observation, for Schwarz Primitive shows to generate the lowest value of WSS with 3.4 mPa respectively. This makes Schwarz Primitive fall within range to promote bone proliferation cell development and the ability to stimulate the biological activity of MSCs to aid in differentiating bone cell types. Additionally, the scaffold pressure output allows the model to support improved cell viability and survival for hemodynamics shear flow.

Furthermore, the topology evaluation for the TPMS scaffold to aid in design prediction has shown the optimal hyperparameter values to be 16, 6, 3, 32, and 25 concerning batch size, convolutional layers, dense layers, layer size, and Epoch training. When evaluating the accuracy, loss, validation accuracy, validation loss, and F-Score, all respectably common trends of this

hyperparameter setting yield ideal performance along with consistent grouping between replications of 5.

Thus, this research has evaluated the machinal performance of 2 different biomaterials with application within bone scaffold regeneration. It has shown that P.W. Hybrid vertical orientation outperforms all 10 TPMS scaffolds. Additionally, the CFD analysis has demonstrated the performance of all 10 TPMS scaffolds for evaluating internal and environmental effects. It displays that Schwarz Primitive has the ideal hemodynamics behavior compared to other TPMS scaffolds. In addition, a 5-class CNN framework was successfully developed by determining the optimal for hyperparameter TPMS topology prediction. This study will aid in designing and experimenting with TPMS scaffolds for bone tissue engineering.

#### References

- [1] Oladapo, B. I., Ismail, S. O., Bowoto, O. K., Omigbodun, F. T., Olawumi, M. A., and Muhammad, M. A., 2020, "Lattice Design and 3D-Printing of PEEK with Ca10 (OH)(PO4) 3 and In-Vitro Bio-Composite for Bone Implant," International Journal of Biological Macromolecules, 165, pp. 50-62, DOI: 10.1016/j.ijbiomac.2020.09.175.
- [2] Han, X., Yang, D., Yang, C., Spintzyk, S., Scheideler, L., Li, P., Li, D., Geis-Gerstorfer, J., and Rupp, F., 2019, "Carbon Fiber Reinforced PEEK Composites Based on 3D-Printing Technology for Orthopedic and Dental Applications," Journal of clinical medicine, 8(2), p. 240, DOI: 10.3390/jcm8020240.
- [3] Manzoor, F., Golbang, A., Jindal, S., Dixon, D., McIlhagger, A., Harkin-Jones, E., Crawford, D., and Mancuso, E., 2021, "3D Printed PEEK/HA Composites for Bone Tissue Engineering Applications: Effect of Material Formulation on Mechanical Performance and Bioactive Potential," Journal of the Mechanical Behavior of Biomedical Materials, 121, p. 104601, DOI: 10.1016/j.jmbbm.2021.104601.
- [4] Ferroni, L., D'Amora, U., Leo, S., Tremoli, E., Raucci, M. G., Ronca, A., Ambrosio, L., and Zavan, B., 2022, "PEEK and Hyaluronan-Based 3D Printed Structures: Promising Combination to Improve Bone Regeneration," Molecules, 27(24), p. 8749, DOI: 10.3390/molecules27248749.
- [5] Zheng, J., Zhao, H., Dong, E., Kang, J., Liu, C., Sun, C., Li, D., and Wang, L., 2021, "Additively-Manufactured PEEK/HA Porous Scaffolds with Highly-Controllable Mechanical Properties and Excellent Biocompatibility," Materials Science and Engineering: C, 128, p. 112333, DOI: 10.1016/j.msec.2021.112333.
- [6] Kang, J., Zheng, J., Hui, Y., and Li, D., 2022, "Mechanical Properties of 3D-Printed PEEK/HA Composite Filaments," Polymers, 14(20), p. 4293, DOI: 10.3390/polym14204293.
- [7] Singh, S., Singh, G., Prakash, C., Ramakrishna, S., Lamberti, L., and Pruncu, C. I., 2020, "3D Printed Biodegradable Composites: An Insight Into Mechanical Properties of PLA/Chitosan Scaffold," Polymer Testing, 89, p. 106722, DOI: 10.1016/j.polymertesting.2020.106722.
- [8] Ali, M. G., Mousa, H. M., Blaudez, F., Abd El-sadek, M., Mohamed, M., Abdel-Jaber, G., Abdal-hay, A., and Ivanovski, S., 2020, "Dual Nanofiber Scaffolds Composed of Polyurethane-Gelatin/Nylon 6-Gelatin for Bone Tissue Engineering," Colloids and Surfaces A: Physicochemical and Engineering Aspects, 597, p. 124817, DOI: 10.1016/j.colsurfa.2020.124817.
- [9] Abdal-Hay, A., Oh, Y. S., Yousef, A., Pant, H. R., Vanegas, P., and Lim, J. K., 2014, "In Vitro Deposition of Ca-P Nanoparticles on Air Jet Spinning Nylon 6 Nanofibers Scaffold for Bone Tissue Engineering," Applied surface science, 307, pp. 69-76, DOI: 10.1016/j.apsusc.2014.03.161.
- [10] Wear, K. A., 2008, "Ultrasonic Attenuation in Parallel-Nylon-Wire Cancellous-Bone-Mimicking Phantoms," The Journal of the Acoustical Society of America, 124(6), pp. 4042-4046, DOI: 10.1121/1.2998784.
- [11] Das, S., Hollister, S. J., Flanagan, C., Adewunmi, A., Bark, K., Chen, C., Ramaswamy, K., Rose, D., and Widjaja, E., 2003, "Freeform Fabrication of Nylon-6 Tissue Engineering Scaffolds," Rapid Prototyping Journal, 9(1), pp. 43-49, DOI: 10.1108/13552540310455656.

- [12] Chen, X., Lian, T., Zhang, B., Du, Y., Du, K., Xiang, N., Jung, D.-W., Wang, G., and Osaka, A., 2021, "Design and Mechanical Compatibility of Nylon Bionic Cancellous Bone Fabricated by Selective Laser Sintering," Materials, 14(8), p. 1965, DOI: 10.3390/ma14081965.
- [13] Pant, H. R., Kim, H. J., Bhatt, L. R., Joshi, M. K., Kim, E. K., Kim, J. I., Abdal-Hay, A., Hui, K., and Kim, C. S., 2013, "Chitin Butyrate Coated Electrospun Nylon-6 Fibers for Biomedical Applications," Applied Surface Science, 285, pp. 538-544, DOI: 10.1016/j.apsusc.2013.08.089.
- [14] Abbasian, V., Emadi, R., and Kharaziha, M., 2020, "Biomimetic Nylon 6-Baghdadite Nanocomposite Scaffold for Bone Tissue Engineering," Materials Science and Engineering: C, 109, p. 110549, DOI: 10.1016/j.msec.2019.110549.
- [15] Mehrabanian, M., and Nasr-Esfahani, M., 2011, "HA/nylon 6, 6 porous scaffolds fabricated by salt-leaching/solvent casting technique: effect of nano-sized filler content on scaffold properties," International journal of nanomedicine, pp. 1651-1659, DOI: 10.2147/IJN.S21203.
- [16] Wang, S., Liu, L., Zhou, X., Zhu, L., and Hao, Y., 2020, "The Design of Ti6Al4V Primitive Surface Structure with Symmetrical Gradient of Pore Size in Biomimetic Bone Scaffold," Materials & Design, 193, p. 108830, DOI: 10.1016/j.matdes.2020.108830.
- [17] Ma, S., Tang, Q., Han, X., Feng, Q., Song, J., Setchi, R., Liu, Y., Liu, Y., Goulas, A., and Engstrøm, D. S., 2020, "Manufacturability, Mechanical Properties, Mass-Transport Properties and Biocompatibility of Triply Periodic Minimal Surface (TPMS) Porous Scaffolds Fabricated by Selective Laser Melting," Materials & Design, 195, p. 109034, DOI: 10.1016/j.matdes.2020.109034.
- [18] Ali, D., Ozalp, M., Blanquer, S. B., and Onel, S., 2020, "Permeability and Fluid Flow-Induced Wall Shear Stress in Bone Scaffolds with TPMS and Lattice Architectures: A CFD Analysis," European Journal of Mechanics-B/Fluids, 79, pp. 376-385, DOI: 10.1016/j.euromechflu.2019.09.015.
- [19] Kim, D., Peng, C., Tran, J., and Philip, J., "An Experimental Study of Pressure Drop and Fluid Flow in Triply Periodic Minimal Surface (TPMS) Scaffolds," Proc. 12th International Symposium on Turbulence and Shear Flow Phenomena (TSFP12), Osaka, Japan, July 19–22, 2022, ReH, pp. 1-4, DOI: N/A.
- [20] Li, Z., Chen, Z., Chen, X., and Zhao, R., 2022, "Effect of Surface Curvature on the Mechanical and Mass-Transport Properties of Additively Manufactured Tissue Scaffolds with Minimal Surfaces," ACS Biomaterials Science & Engineering, 8(4), pp. 1623-1643, DOI: 10.1021/acsbiomaterials.1c01438.
- [21] Pires, T. H., Dunlop, J. W., Castro, A. P., and Fernandes, P. R., 2022, "Wall Shear Stress Analysis and Optimization in Tissue Engineering TPMS Scaffolds," Materials, 15(20), p. 7375, DOI: 10.3390/ma15207375.
- [22] Pires, T., Dunlop, J. W., Fernandes, P. R., and Castro, A. P., 2022, "Challenges in Computational Fluid Dynamics Applications for Bone Tissue Engineering," Proceedings of the Royal Society A, 478(2257), p. 20210607, DOI: 10.1098/rspa.2021.0607.
- [23] Kumar, J., Nirala, N. s., Singh, N. K., Gupta, N., Dwivedi, Y. D., Verma, R., Rai, S. K., and Gupta, M., 2023, "Design, Development and Fluidic Behavior Analysis of Triply Periodic Minimal Surface (TPMS) Based Scaffolds for Bone-Aplications," International Journal on Interactive Design and Manufacturing (IJIDeM), pp. 1-11, DOI: 10.1007/s12008-023-01441-2.

- [24] Deng, F., Liu, L., Li, Z., and Liu, J., 2021, "3D Printed Ti6Al4V Bone Scaffolds with Different Pore Structure Effects on Bone Ingrowth," Journal of biological engineering, 15, pp. 1-13, DOI: 10.1186/s13036-021-00255-8.
- [25] Daver, A., "Scaffolds for Bone Using Inclined Schwarz TPMS; Design and Finite Element Analysis," Proc. International Science and Art Research Congress (ISARC), Istanbul, Turkey, 24-25 December 2022., p. 5, DOI: N/A.
- [26] Singh, S., Yadav, S. K., Meena, V. K., Vashisth, P., and Kalyanasundaram, D., 2023, "Orthopedic Scaffolds: Evaluation of Structural Strength and Permeability of Fluid Flow via an Open Cell Neovius Structure for Bone Tissue Engineering," ACS Biomaterials Science & Engineering, 9(10), pp. 5900-5911, DOI: 10.1021/acsbiomaterials.3c00436.
- [27] Guerreiro, R., Pires, T., Guedes, J. M., Fernandes, P. R., and Castro, A. P., 2020, "On the Tortuosity of TPMS Scaffolds for Tissue Engineering," Symmetry, 12(4), p. 596, DOI: 10.3390/sym12040596.
- [28] Li, Z., Chen, Z., Chen, X., and Zhao, R., 2023, "Design and Evaluation of TPMS-Inspired 3D-Printed Scaffolds for Bone Tissue Engineering: Enabling Tailored Mechanical and Mass Transport Properties," Composite Structures, p. 117638, DOI: 10.1016/j.compstruct.2023.117638.
- [29] Dong, Z., and Zhao, X., 2021, "Application of TPMS Structure in Bone Regeneration," Engineered Regeneration, 2, pp. 154-162, DOI: 10.1016/j.engreg.2021.09.004.
- [30] Naghavi, S. A., Tamaddon, M., Marghoub, A., Wang, K., Babamiri, B. B., Hazeli, K., Xu, W., Lu, X., Sun, C., and Wang, L., 2022, "Mechanical Characterisation and Numerical Modelling of TPMS-Based Gyroid and Diamond Ti6Al4V Scaffolds for Bone Implants: An Integrated Approach for Translational Consideration," Bioengineering, 9(10), p. 504, DOI: 10.3390/bioengineering9100504.
- [31] Du, X., Ronayne, S., Lee, S. S., Hendry, J., Hoxworth, D., Bock, R., and Ferguson, S. J., 2023, "3D-Printed PEEK/Silicon Nitride Scaffolds with a Triply Periodic Minimal Surface Structure for Spinal Fusion Implants," ACS Applied Bio Materials, 6(8), pp. 3319-3329, DOI: 10.1021/acsabm.3c00383.
- [32] Khrapov, D., Kozadayeva, M., Manabaev, K., Panin, A., Sjöström, W., Koptyug, A., Mishurova, T., Evsevleev, S., Meinel, D., and Bruno, G., 2021, "Different Approaches for Manufacturing Ti-6Al-4V Alloy with Triply Periodic Minimal Surface Sheet-Based Structures by Electron Beam Melting," Materials, 14(17), p. 4912, DOI: 10.3390/ma14174912.
- [33] Mishra, A. K., Chavan, H., and Kumar, A., 2021, "Effect of Material Variation on the Uniaxial Compression Behavior of FDM Manufactured Polymeric TPMS Lattice Materials," Materials Today: Proceedings, 46, pp. 7752-7759, DOI: 10.1016/j.matpr.2021.02.276.
- [34] Tilton, M., Jacobs, E., Overdorff, R., Potes, M. A., Lu, L., and Manogharan, G., 2023, "Biomechanical Behavior of PMMA 3D Printed Biomimetic Scaffolds: Effects of Physiologically Relevant Environment," Journal of the mechanical behavior of biomedical materials, 138, p. 105612, DOI: 10.1016/j.jmbbm.2022.105612.
- [35] De Aquino, D., Maskery, I., Longhitano, G., Jardini, A., and Del Conte, E., 2020, "Investigation of Load Direction on the Compressive Strength of Additively Manufactured Triply Periodic Minimal Surface Scaffolds," The International Journal of Advanced Manufacturing Technology, 109, pp. 771-779, DOI: 10.1007/s00170-020-05706-y.
- [36] Hameed, P., Liu, C.-F., Ummethala, R., Singh, N., Huang, H.-H., Manivasagam, G., and Prashanth, K. G., 2021, "Biomorphic Porous Ti6Al4V Gyroid Scaffolds for Bone Implant

- Applications Fabricated by Selective Laser Melting," Progress in Additive Manufacturing, 6, pp. 455-469, DOI: 10.1007/s40964-021-00210-5.
- [37] Maevskaia, E., Guerrero, J., Ghayor, C., Bhattacharya, I., and Weber, F. E., 2023, "Triply Periodic Minimal Surface-Based Scaffolds for Bone Tissue Engineering: A Mechanical, In Vitro and In Vivo Study," Tissue Engineering Part A, 29(19-20), pp. 507-517, DOI: 10.1089/ten.tea.2023.0033.
- [38] Castro, A., Ruben, R., Gonçalves, S., Pinheiro, J., Guedes, J., and Fernandes, P., 2019, "Numerical and Experimental Evaluation of TPMS Gyroid Scaffolds for Bone Tissue Engineering," Computer methods in biomechanics and biomedical engineering, 22(6), pp. 567-573, DOI: 10.1080/10255842.2019.1569638.
- [39] Valainis, D., Dondl, P., Foehr, P., Burgkart, R., Kalkhof, S., Duda, G. N., Van Griensven, M., and Poh, P. S., 2019, "Integrated Additive Design and Manufacturing Approach for the Bioengineering of Bone Scaffolds for Favorable Mechanical and Biological Properties," Biomedical Materials, 14(6), p. 065002, DOI: 10.1088/1748-605X/ab38c6.
- [40] Cai, Z., Liu, Z., Hu, X., Kuang, H., and Zhai, J., 2019, "The Effect of Porosity on the Mechanical Properties of 3D-Printed Triply Periodic Minimal Surface (TPMS) Bioscaffold," Bio-Design and Manufacturing, 2, pp. 242-255, DOI: 10.1007/s42242-019-00054-7.
- [41] Yang, L., Yan, C., Cao, W., Liu, Z., Song, B., Wen, S., Zhang, C., Shi, Y., and Yang, S., 2019, "Compression–Compression Fatigue Behaviour of Gyroid-Type Triply Periodic Minimal Surface Porous Structures Fabricated by Selective Laser Melting," Acta Materialia, 181, pp. 49-66, DOI: 10.1016/j.actamat.2019.09.042.
- [42] Gabrieli, R., Wenger, R., Mazza, M., Verné, E., and Baino, F., 2024, "Design, Stereolithographic 3D Printing, and Characterization of TPMS Scaffolds," Materials, 17(3), p. 654, DOI: 10.3390/ma17030654.
- [43] Vijayavenkataraman, S., Kuan, L. Y., and Lu, W. F., 2020, "3D-Printed Ceramic Triply Periodic Minimal Surface Structures for Design of Functionally Graded Bone Implants," Materials & Design, 191, p. 108602, DOI: 10.1016/j.matdes.2020.108602.
- [44] Blatt, J., Kirkendoll, J., Mandava, P. K., Preston, Z., Joyce, R., and Salary, R. R., "An Image-Based Convolutional Neural Network Platform for the Prediction of the Porosity of Composite Bone Scaffolds, Fabricated Using Material Extrusion Additive Manufacturing," Proc. Paper No. IMECE2022-95044, ASME International Mechanical Engineering Congress & Exposition (IMECE 2022), Columbus, OH, USA, October 30 November 3, 2022, American Society of Mechanical Engineers, DOI: 10.1115/IMECE2022-95044.
- [45] Lu, Y., Gong, T., Yang, Z., Zhu, H., Liu, Y., and Wu, C., 2022, "Designing Anisotropic Porous Bone Scaffolds Using a Self-Learning Convolutional Neural Network Model," Frontiers in Bioengineering and Biotechnology, 10, p. 973275, DOI: 10.3389/fbioe.2022.973275.
- [46] Peng, B., Wei, Y., Qin, Y., Dai, J., Li, Y., Liu, A., Tian, Y., Han, L., Zheng, Y., and Wen, P., 2023, "Machine Learning-Enabled Constrained Multi-Objective Design of Architected Materials," Nature Communications, 14(1), p. 6630, DOI: 10.1038/s41467-023-42415-y.
- [47] Ibrahimi, S., D'Andrea, L., Gastaldi, D., Rivolta, M. W., and Vena, P., 2024, "Machine Learning Approaches for the Design of Biomechanically Compatible Bone Tissue Engineering Scaffolds," Computer Methods in Applied Mechanics and Engineering, 423, p. 116842, DOI: 10.1016/j.cma.2024.116842.

- [48] Wei, Y., Qin, Y., Peng, B., Dai, J., Li, Y., Han, L., and Wen, P., 2022, "Data-Efficient, Multi-Objective Machine Learning Approach for Additively Manufactured Cellular Materials," ReALML 2022.
- [49] Patel, D., Yang, R., Wang, J., Rai, R., and Dargush, G., 2023, "Deep Learning-Based Inverse Design Framework for Property Targeted Novel Architectured Interpenetrating Phase Composites," Composite Structures, 312, p. 116783, DOI: 10.1016/j.compstruct.2023.116783.
- [50] Minnema, J., van Eijnatten, M., Kouw, W., Diblen, F., Mendrik, A., and Wolff, J., 2018, "CT Image Segmentation of Bone for Medical Additive Manufacturing Using a Convolutional Neural Network," Computers in biology and medicine, 103, pp. 130-139, DOI: 10.1016/j.compbiomed.2018.10.012.
- [51] Bermejillo Barrera, M. D., Franco-Martínez, F., and Díaz Lantada, A., 2021, "Artificial Intelligence Aided Design of Tissue Engineering Scaffolds Employing Virtual Tomography and 3D Convolutional Neural Networks," Materials, 14(18), p. 5278, DOI: 10.3390/ma14185278.
- [52] Akogo, D. A., and Palmer, X.-L., "ScaffoldNet: Detecting and Classifying Biomedical Polymer-Based Scaffolds via a Convolutional Neural Network," Proc. Advances in Information and Communication: Proceedings of the 2019 Future of Information and Communication Conference (FICC), Volume 2, Springer, pp. 152-161, DOI: 10.1007/978-3-030-12385-7 13.
- [53] Deering, J., Mahmoud, D., Rier, E., Lin, Y., do Nascimento Pereira, A. C., Titotto, S., Fang, Q., Wohl, G. R., Deng, F., and Grandfield, K., 2023, "Osseointegration of Functionally Graded Ti6Al4V Porous Implants: Histology of the Pore Network," Biomaterials Advances, 155, p. 213697, DOI: 10.1016/j.bioadv.2023.213697.
- [54] Bardini, R., and Di Carlo, S., 2024, "Computational Methods for Biofabrication in Tissue Engineering and Regenerative Medicine-A Literature Review," Computational and Structural Biotechnology Journal, DOI: 10.1016/j.csbj.2023.12.035.
- [55] Bouakaz, I., Drouet, C., Grossin, D., Cobraiville, E., and Nolens, G., 2023, "Hydroxyapatite 3D-Printed Scaffolds with Gyroid-Triply Periodic Minimal Surface Porous Structure: Fabrication and an *in vivo* Pilot Study in Sheep," Acta Biomaterialia, 170, pp. 580-595, DOI: 10.1016/j.actbio.2023.08.041.
- [56] Manescu, V., Antoniac, I., Antoniac, A., Laptoiu, D., Paltanea, G., Ciocoiu, R., Nemoianu, I. V., Gruionu, L. G., and Dura, H., 2023, "Bone Regeneration Induced by Patient-Adapted Mg Alloy-Based Scaffolds for Bone Defects: Present and Future Perspectives," Biomimetics, 8(8), p. 618, DOI: 10.3390/biomimetics8080618.
- [57] Chaffins, A., Yu, M., Claudio, P. P., Day, J. B., and Salary, R. R., "Investigation of the Functional Properties of Additively-Fabricated Triply Periodic Minimal Surface-Based Bone Scaffolds for the Treatment of Osseous Fractures," Proc. Paper No. 2004, ASME 2021 International Manufacturing Science and Engineering Conference (MSEC 2021), Hosted by the University of Cincinnati, Cincinnati, OH, USA, June 21-25, 2021., American Society of Mechanical Engineers, DOI: 10.1115/MSEC2021-63413.
- [58] Zhao, D., Hart, C., Weese, N. A., Rankin, C. M., Kuzma, J., Day, J. B., and Salary, R. R., "Experimental and Computational Analysis of the Mechanical Properties of Biocompatible Bone Scaffolds, Fabricated Using Fused Deposition Modeling Additive Manufacturing Process," Proc. Paper No. 8511, ASME 2020 International Manufacturing Science and

- Engineering Conference (MSEC 2020), Cincinnati, OH, USA, June 22-26, 2020., American Society of Mechanical Engineers, DOI: 10.1115/MSEC2020-8511.
- [59] Salary, R., 2022, "Perspective Chapter: Advanced Manufacturing for Bone Tissue Engineering and Regenerative Medicine," Advanced Additive Manufacturing, I. V. Shishkovsky, ed., IntechOpen, London, UK, p. 59, DOI: 10.5772/intechopen.102563.
- [60] Mandava, P. K., Joyce, R., Day, J. B., and Salary, R. R., "Investigation of the Mechanical Properties of Additively Manufactured Bone Tissue Scaffolds, Composed of Polyamide, Polyolefin, and Cellulose Fibers," Proc. Paper No. 85435, ASME 2022 International Manufacturing Science and Engineering Conference (MSEC 2022), Purdue University, West Lafayette, IN, USA, June 27 July 01, 2022., American Society of Mechanical Engineers, DOI: 10.1115/MSEC2022-85435.
- [61] Lawrence, L. M., Salary, R., Miller, V., Valluri, A., Denning, K. L., Case-Perry, S., Abdelgaber, K., Smith, S., Claudio, P. P., and Day, J. B., 2023, "Osteoregenerative Potential of 3D-Printed Poly ε-Caprolactone Tissue Scaffolds In Vitro Using Minimally Manipulative Expansion of Primary Human Bone Marrow Stem Cells," International Journal of Molecular Sciences, 24(5), p. 4940, DOI: 10.3390/ijms24054940.
- [62] Brakke, K., 2020, "Triply Periodic Minimal Surfaces," Department of Mathematics and Computer Science, Susquehanna University, Selinsgrove, PA, USA.
- [63] Hoffman, D., Hoffman, J., Weber, M., Trazet, M., Wohlgemuth, M., Boix, E., Callahan, M., Thayer, E., and Wei, F., 2019, "The Scientific Graphics Project Triply Periodic Level Surfaces," Mathematical Sciences Research Institute, Berkeley, CA, USA.
- [64] Shin, J., Kim, S., Jeong, D., Lee, H. G., Lee, D., Lim, J. Y., and Kim, J., 2012, "Finite Element Analysis of Schwarz P Surface Pore Geometries for Tissue-Engineered Scaffolds," Mathematical Problems in Engineering, 2012(Article ID 694194), DOI: 10.1155/2012/694194.
- [65] ANSYS-Fluent, 2015, "16.2 Theory Guide," ANSYS Inc., Canonsburg, PA.
- [66] Salary, R., Lombardi, J. P., Tootooni, M. S., Donovan, R., Rao, P. K., Borgesen, P., and Poliks, M. D., 2017, "Computational Fluid Dynamics Modeling and Online Monitoring of Aerosol Jet Printing Process," Journal of Manufacturing Science and Engineering, 139(2), p. 021015, DOI: 10.1115/1.4034591.
- [67] Salary, R., Lombardi, J. P., Weerawarne, D. L., Rao, P., and Poliks, M. D., 2021, "A Computational Fluid Dynamics Investigation of Pneumatic Atomization, Aerosol Transport, and Deposition in Aerosol Jet Printing Process," Journal of Micro-and Nano-Manufacturing, 9(1), p. 010903, DOI: 10.1115/1.4049958.
- [68] Yu, M., Yeow, Y. J., Lawrence, L., Claudio, P. P., Day, J. B., and Salary, R., 2021, "Characterization of the Functional Properties of PCL Bone Scaffolds Fabricated Using Pneumatic Microextrusion" Journal of Micro-and Nano-Manufacturing, JMNM-20-1074, DOI: 10.1115/1.4051631.
- [69] Omar, A. M., Hassan, M. H., Daskalakis, E., Ates, G., Bright, C. J., Xu, Z., Powell, E. J., Mirihanage, W., and Bartolo, P. J., 2022, "Geometry-Based Computational Fluid Dynamic Model for Predicting the Biological Behavior of Bone Tissue Engineering Scaffolds," Journal of Functional Biomaterials, 13(3), p. 104, DOI: 10.3390/jfb13030104.
- [70] Salary, R., Lombardi, J., Rao, P., and Poliks, M. D., 2017, "Online Monitoring of Functional Electrical Properties in Aerosol Jet Printing Additive Manufacturing Process Using Shape-From-Shading Image Analysis," ASME Journal of Manufacturing Science and Engineering, 139(10), pp. 101010-101010-101013, DOI: 10.1115/1.4036660.

- [71] Salary, R., Lombardi, J. P., Weerawarne, D. L., Tootooni, M. S., Rao, P. K., and Poliks, M. D., 2020, "A Sparse Representation Classification Approach for Near Real-Time, Physics-Based Functional Monitoring of Aerosol Jet-Fabricated Electronics," Journal of Manufacturing Science and Engineering, Paper No: MANU-18-1807, 081007 (17 pages), 142(8), DOI: 10.1115/1.4047045.
- [72] E3D, "V6 Assembly," C. Open Source Creative Commons CC BY-SA 3.0 License, UK, <a href="https://e3d-online.dozuki.com/">https://e3d-online.dozuki.com/</a>, ed., DOI:

## Appendix A: IRB Approval Letter



Office of Research Integrity

July 1, 2024

Brandon Coburn 311 Rocky Fork Road Otway, OH 45657

Dear Brandon,

This letter is in response to the submitted thesis abstract titled "Numerical Design, Fabrication, and Characterization of Porous Tissue Scaffolds for Bone Regeneration." After assessing the abstract, it has been deemed not to be human subject research and therefore exempt from oversight by the Marshall University Institutional Review Board (IRB). The Code of Federal Regulations (45CFR46) has set forth the criteria utilized in making this determination. Since the information in this study does not involve human subject as defined in the above referenced instruction, it is not considered human subject research. If there are any changes to the abstract you provided, then you would need to resubmit that information to the Office of Research Integrity for review and a determination.

I appreciate your willingness to submit the abstract for determination. Please feel free to contact the Office of Research Integrity if you have any questions regarding future protocols that may require IRB review.

Sincerely,

Bruce F. Day, ThD, CIP

Director

WE ARE... MARSHALL.

One John Marshall Drive • Huntington, West Virginia 25755 • Tel 304/696-4303 A State University of West Virginia • An Affirmative Action/Equal Opportunity Employer